Journal of Electron Spectroscopy and Related Phenomena, 67 (1994) 529–622
0368-2048/94/$07.00

Review

X-ray absorption and dichroism of transition metals and their compounds

F.M.F. de Groot[1]

Spectroscopy of Solids and Surfaces, University of Nijmegen, Toernooiveld, 6525 ED Nijmegen, The Netherlands

(First received 28 December 1992; in final form 27 October 1993)

Abstract

This review presents an overview of the X-ray absorption spectra of 3d transition metals and their compounds. The emphasis is on the description of the X-ray absorption process and the various routes to interpret the results within the framework of their electronic structure. This also includes the use of polarization dependent measurements which are particularly used for the study of the magnetic structure. Emphasis will be given to the metal 2p spectra for which the obtainable resolution has been greatly improved over the last 10 years. The interpretation of 2p core spectra, photoemission as well as absorption, is dominated by short range models, such as the Anderson impurity model. It has been shown that 2p X-ray absorption is relatively insensitive to charge transfer effects which simplifies the analysis. The interpretation with a ligand field multiplet model accounts well for the observed spectra and due to its simplicity this model yields accurate and well defined electronic structure parameters. For the 1s X-ray absorption spectra, of the metals as well as of the ligands, it has been shown that they correspond closely to the unoccupied density of states as determined from single particle schemes using either band structure methods or real space multiple scattering. A number of potentially important effects beyond this interpretation will be discussed. Overviews will be given of the published X-ray absorption results for the metal 2p, the metal 1s and the ligand 1s spectra.

Contents

1. Introduction 530

2. Experimental 530
   2.1. Synchrotron radiation 531
   2.2. X-ray monochromators 533
   2.3. Detection techniques 535

3. Electronic structure models 537
   3.1. The Hartree–Fock (HF) approximation 537
   3.2. The local spin density (LSD) approximation 538
   3.3. The generalized gradient approximation (GGA) 539
   3.4. *GW* calculations 540
   3.5. The short range ("Anderson impurity") models 541
   3.6. The inclusion of U in LSD calculations 541
   3.7. The self-interaction correction (SIC) . . 542
   3.8. Multiplet effects (orbital polarization) . 543
   3.9. Ligand field multiplet (LFM) model . . 543
   3.10. Multi-configurational approaches . . . 544

4. Core excitations 544
   4.1. The interaction of X-rays with matter . 545
   4.2. XAS versus XPS 546
   4.3. Short range models for core spectroscopies 547
   4.4. Interplay between charge transfer and multiplet effects 550

5. Metal 2p X-ray absorption 550
   5.1. The ligand field multiplet model 550

[1] Present address: Laboratoire pour l'Utilisation du Rayonnement Electromagnetique, Université Paris-Sud, Bâtiment 209 d, F-91405 Orsay Cedex, France.

SSDI 0368-2048(93)02041-J

5.2. When are multiplets important? 564
5.3. The short range model extended for multiplets 566

6. X-ray magnetic circular dichroism (X-MCD) 578
6.1. The atomic single electron model. 578
6.2. Sum rules 582
6.3. Linear dichroism. 585

7. Overview of the published metal 2p spectra 587
7.1. Calcium 2p X-ray absorption spectra . 588
7.2. Scandium 2p X-ray absorption spectra 589
7.3. Titanium 2p X-ray absorption spectra. 589
7.4. Vanadium 2p X-ray absorption spectra 590
7.5. Chromium 2p X-ray absorption spectra 590
7.6. Manganese 2p X-ray absorption spectra 590
7.7. Iron 2p X-ray absorption spectra 592
7.8. Cobalt 2p X-ray absorption spectra. . . 592
7.9. Nickel 2p X-ray absorption spectra. . . 593
7.10. Copper 2p X-ray absorption spectra . 594

8. Metal and ligand 1s X-ray absorption 594
8.1. Band structure techniques 595
8.2. Multiple scattering formulation. 595
8.3. Ligand 1s X-ray absorption. 596
8.4. Metal 1s X-ray absorption spectra. 602
8.5. Overview of the ligand 1s spectra 607
8.6. Overview of the metal 1s spectra 608

9. Concluding remarks and outlook. 608
9.1. The metal 2p X-ray absorption spectra 608
9.2. The ligand 1s X-ray absorption spectra 608
9.3. The valency and symmetry of the metal ions 609
9.4. The electronic configuration 609
9.5. The short range model Hamiltonians. . 609
9.6. The use of X-ray absorption for the study of materials. 609

References 610

Appendix A: Final state effects on Hubbard model parameters 620

Appendix B: Abbreviations, etc. 621

1. Introduction

This review is an attempt to give an overview of the field of X-ray absorption, including their magnetic circular dichroism (MCD), of transition metals and their compounds. The main emphasis of this review is the metal 2p spectra. The review concentrates on the analysis using the ligand field multiplet model as well as short range model Hamiltonians. For clarity it is noted that this route of analysis is sometimes envisaged as a particular "school" of spectral analysis which is not universally accepted. Some important other "schools", for example the multiple scattering schemes, are mentioned only very briefly. Most controversies in the analysis are touched upon in the various sections.

The outline of the review is as follows: Section 2 introduces some of the experimental aspects of X-ray absorption experiments. Section 3 gives a short overview of the models used for the description of the electronic structure of transition metals and their compounds. Section 4 describes the interaction of X-rays with matter. It describes core excitations and focuses on the short range model descriptions of core level spectroscopies. Section 5 deals with metal 2p X-ray absorption. The ligand field multiplet model and the charge transfer multiple model are discussed in detail. Section 6 discusses the different routes to interpret MCD spectra. The different models interpreting X-ray absorption, now extended for their sensitivity to circularly polarized X-rays, are compared. Section 7 gives an overview of the existing data of metal 2p spectra, including the linear and circular dichroism studies. Section 8 describes the analysis of metal and ligand 1s X-ray absorption spectra in terms of single particle calculations, including multiple scattering approaches. It also includes a (selected) overview of published data of the 1s edges of the ligands as well as of the metals.

2. Experimental

The normal set-up to measure an X-ray absorption spectrum is in transmission mode as sketched

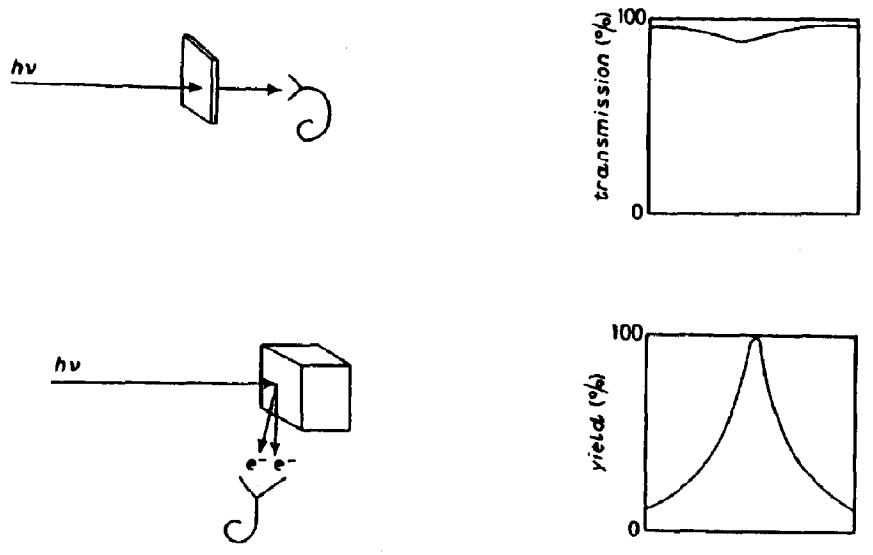

Fig. 1.Transmission mode (top) and yield mode (bottom) X-ray absorption experiments.

in Fig. 1 at the top. The intensity of the X-ray is measured before and after the substrate and the percentage of transmitted X-rays is determined. The X-ray absorption spectrum is generated by repeating the experiment for a series of X-ray energies.

Transmission mode experiments are standard for hard X-rays. For soft X-rays, in order to obtain a detectable signal the substrate has to be thin, typically 0.1 μm. This poses large technological problems for most materials. Soft X-rays also have a large absorption cross section with air; hence the experiments have to be performed in vacuum. An alternative to the transmission mode experiments has been provided by measuring the decay products of the core hole which is created in the absorption process. The decay of the core hole gives rise to an avalanche of electrons, photons and ions escaping from the surface of the substrate. The bottom of Fig. 1 shows a yield mode experiment of the X-ray absorption cross section, with which it is possible to measure samples of arbitrary thickness.

X-ray absorption experiments have been performed since the beginning of this century, but they have been severely restricted because the only available X-ray sources had a restricted set of intense discrete energies with a Bremsstrahlung continuum of relatively low intensity. The advent of synchrotron radiation sources, which provide an intense and continuum spectrum of polarized electromagnetic radiation, created the possibility of immensely improving the X-ray absorption spectra. The intrinsic polarization features of the X-ray beam can be exploited to do dichroism experiments. The following experimental aspects of the X-ray absorption and dichroism experiments will be discussed: synchrotron radiation, X-ray monochromators and detection techniques.

2.1. Synchrotron radiation

Synchrotron radiation is produced when a charged particle, with an energy $E \gg mc^2$, is deflected in a magnetic field. The development of synchrotron radiation is based on the work of Ivanenko and Pomaranchuk [Iva44] and Schwinger [Sci46] in the forties [Koc77, Fug91]. The original synchrotrons were used for high energy physics and the radiation was considered merely as a side product. The experiments which made use of the radiation were performed in a parasitic fashion. However the interesting results which emerged led to the development of

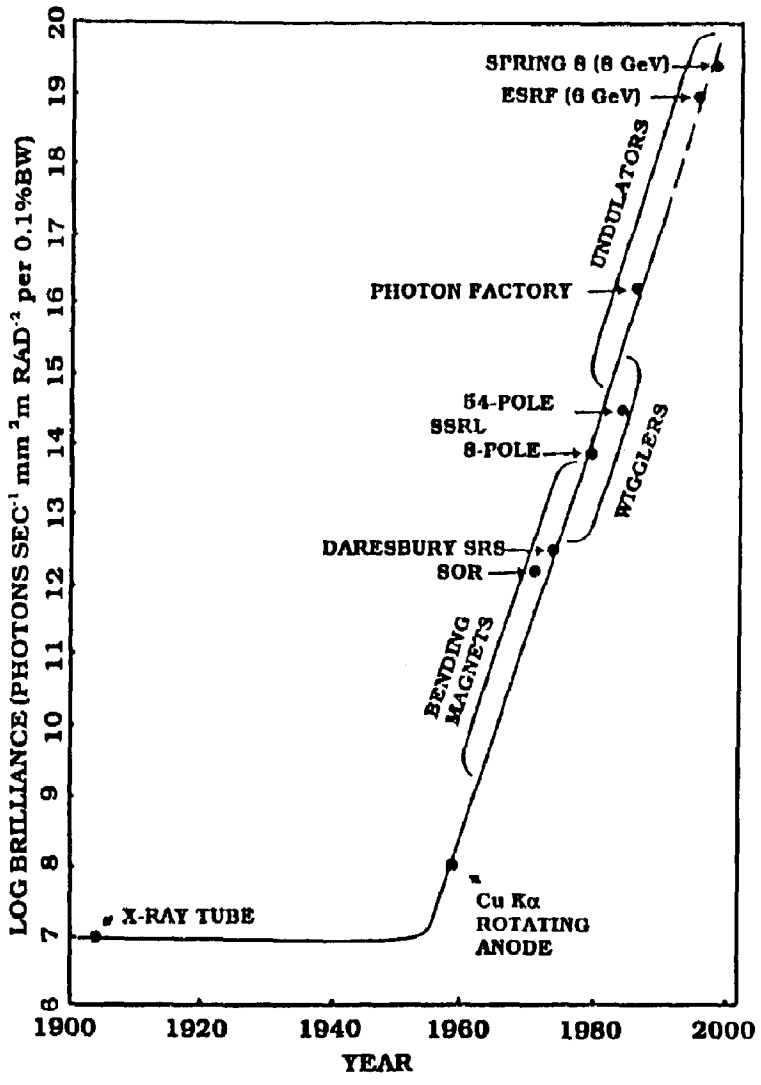

Fig. 2. The historical development of the brilliance of available X-ray sources (from [Fug91]).

dedicated synchrotron radiation sources in the early seventies and the SRS synchrotron in Daresbury can be considered as the first dedicated storage ring for synchrotron radiation. The original emphasis was on the optimization of the life-time, the current and the energy of the beam. In the early eighties the emphasis switched to an optimization of the brilliance and also to the development of insertion devices to increase the intensity of high energy photons [Fug91]. Figure 2 sketches the development of the available X-ray flux during the last century (taken from [Fug91]).

As a typical example of a dedicated VUV-ring the Berliner Elektronen-Speicherring Gesellschaft für SYnchrotronstrahlung (BESSY) [Ber87] will be discussed. BESSY is an electron storage ring with a circumference of about 62 m. From each of the twelve bending magnets synchrotron radiation is directed to a number of experimental stations. The energy of the electrons stored in the ring is 754 MeV. To keep the electrons in orbit they are accelerated at one point in the ring to compensate the energy-loss due to emission of radiation in the bending magnets. The position of the beam within

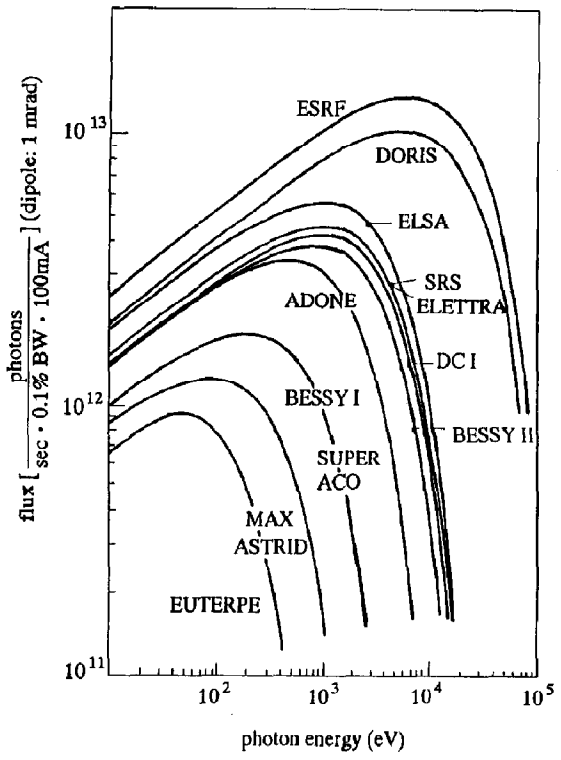

Fig. 3. Intensity distribution of the radiation in the European synchrotron radiation facilities. ESRF, ELETTRA and BESSY II are not as yet operational. DORIS and ELSA are used parasitically (from [Fug91]).

the synchrotron ring is constantly corrected with a series of quadrupolar and sextupolar magnets, but nevertheless the stored current slowly decreases because of scattering with remnant gas, imperfect orbit correction, etc. The typical life-time of an 800 MeV ring such as BESSY, superACO and NSLS-VUV is 2 to 5 h [Fug91].

The deflection of the electrons in the bending magnets creates electromagnetic radiation with an energy distribution as sketched in Fig. 3 [Iva44, Sci46, Ten85]. The critical energy e_c is determined by the energy of the electrons and by the magnetic field in the deflection magnets. For BESSY the critical energy is about 600 eV, which roughly equals the energy with the highest flux as can be checked in Fig. 3. Figure 4 shows the radial distribution of the radiation for three typical X-ray energies relative to the critical energy e_c. The radiation in the plane of the orbiting electrons is linearly

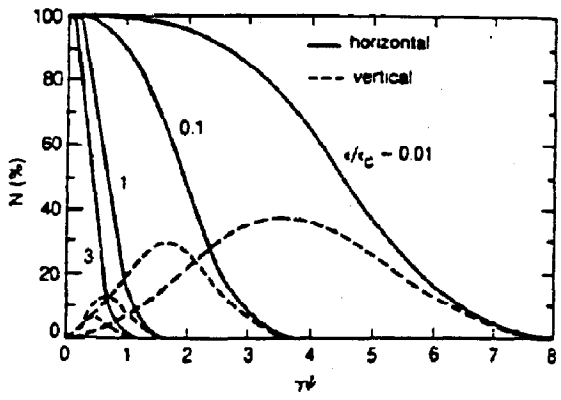

Fig. 4. Radial distribution of intensity. $\gamma\psi$ is the angle (in mrad) with the plane of the electron-orbit.

polarized. Out-of-plane radiation is partly circularly polarized. By selecting part of this out-of-plane radiation, the circularly polarized X-rays can be used for X-ray magnetic circular dichroism (X-MCD) experiments. The intensity of the out-of-plane radiation decreases quickly, especially for soft X-rays. However the intensity profile can be modified with the use of insertion devices, such as an asymmetric wiggler [Sai92].

2.2. X-ray monochromators

X-rays can be monochromatized with crystal monochromators or with gratings. The 1s edges of the 3d transition metals have an energy of 5 to 9 keV and in general Si crystals are used. The 2p edges have an energy in the energy range in between 200 and 1000 eV, that is in between the traditional regions of grating monochromators ($E < 200$ eV) and crystal monochromators ($E > 800$ eV).

2.2.1. Crystal monochromators

For energies above 800 eV the usual way to monochromatize the X-ray is by means of a double crystal monochromator. The X-ray beam impinges on the first crystal and the X-ray energy which satisfies Bragg's equation ($n\lambda = 2d \sin\theta$) is reflected. In principle one crystal is enough to monochromatize the beam; the second crystal improves the resolution slightly but it is used

primarily because it allows for a constant direction of the outgoing monochromatized X-ray. The energy range of the double crystal monochromator is defined by the lattice spacing of the crystals used, given that the angle of incidence (θ) is limited to between 10° and 80°. For energies above 2 keV artificial silicon crystals ($2d = 6.271$ Å) are used. The difficult energy range in between 800 and 1500 eV is covered by crystals of natural beryl $Be_3Al_2Si_6O_{18}$ ($2d = 15.95$ Å). For energies lower than 800 eV one has to use crystals with a lattice spacing larger than beryl. The organic crystals with this property are, however, not resistant to the full power of the synchrotron beam. A solution to this problem has been found by using an artificial multilayer as a pre-monochromator [Laa87]; however for energies below 1 keV the grating monochromators are dominant (see Section 2.2.2). The use of beryl has drawbacks because of the limited allowed heatload and particularly the content of aluminium and silicon. Recently YB_{66}, a cubic crystal with $2d = 23.44$ Å, has been tested [Scf92, Won90]. This material has a slightly improved resolution, but its greatest merit is the absence of absorbing elements in between 1 and 2 keV, which makes it a suitable monochromator for silicon and aluminium 2p edges. A complication in the use of crystal monochromators for circular dichroism experiments is the decrease of the degree of polarization in non-grazing geometries.

2.2.2. *Grating monochromators*

The monochromatizing element is an artificial grating with typically 1000 lines per mm ($2d \approx 5 \times 10^{-7}$ m). The soft X-ray range can be covered by using the grating monochromators in grazing incidence ($\theta \rightarrow 0$). The grazing incidence grating monochromators are divided according to the shape of the grating, which can be toroidal, planar or circular. The toroidal grating monochromators (TGMs) dominate in the energy range up to 200 eV. At present the energy region in between 200 eV and 800 eV is best served with either a planar grating monochromator (PGM) or with a spherical (or cylindrical) grating monochromator (SGM).

A typical SGM is the grasshopper as used at Stanford Synchrotron Radiation Laboratory (SSRL) [Bro78]. This monochromator and also the 10-metre monochromator at Photon Factory [Mae86] use the Rowland circle geometry. The Rowland circle constraints were relaxed in the later designs of Padmore [Pad87, Pad89] and Chen [Che87]. The Dragon monochromator [Che87, Che89, Che90a] at the National Synchrotron Light Source (NSLS) at Brookhaven reached an unprecedented high resolution of $1:10^4$ for the soft X-ray range. The strength of the Dragon monochromator is its relatively simple arrangement of optical components. The entrance slit improves the resolution by making the monochromator less dependent on the source size. The exit slit moves during an energy-scan and the mirrors are situated before the grating. This arrangement facilitates the change of the monochromator position to use out-of-plane (circularly polarized) radiation. A design in which the beam is split in the mirrorbox and radiation from above and below the synchrotron plane is guided to the sample simultaneously (the so-called double headed Dragon) has been proved to be very effective for MCD experiments [Che90b].

The plane grating SX700 monochromators [Pet82, Pet86, Tog86] were designed to monochromatize the synchrotron radiation onto a fixed exit slit, without the necessity of an entrance slit. This can be achieved by a combined movement of the plane grating and the mirrors. The first plane pre-mirror is used to satisfy the focusing condition of the plane grating [Pet82]. The second ellipsoidal mirror refocuses the radiation onto the curved exit slit. The resolution is mainly source limited because there is no entrance slit. The resolution of the SX700/1 is about $1:10^3$ and the SX700/2 monochromator has a resolution of about $1:10^4$ [Dom91]. The SX700/3 monochromator is adapted to the use of out-of-plane circularly polarized light [Wim92].

2.2.3. What do you need for X-ray absorption?

The present resolution of $1:10^4$, reached by both SGMs and PGMs, is satisfactory, and for solids life-time broadening is of the same order of magnitude (depending on the particular edge and material). For the MCD measurements both the Dragon-like and SX700 monochromators reach similar degrees of polarization. Throughput is in general not a large constraint for X-ray absorption; it is for photoemission.

A large number of SGMs and PGMs usable for (soft) X-ray absorption are available at close to all the synchrotron sources in the world. The new generation of synchrotrons, ESRF, APS, SPRING8 and particularly for the soft X-ray range ALS, ELETTRA, BESSY2 and MAX2, will provide improved brilliance. This can and will further improve the various parameters of the monochromators, particularly the flux, but constraints such as heatload will necessitate further improvements in the design and optical elements.

2.3. Detection techniques

As sketched in Fig. 1, the absorption cross section can be measured by means of electrons which escape from the surface as a result of the decay of the core hole. Instead of electrons, photons or ions can be detected, and the electron, fluorescence and ion-yield methods present an alternative to the transmission mode experiments. In this section the different methods are discussed, specifically with regard to the conditions under which a specific yield measurement represents the X-ray absorption cross section and the related question of the probing depth of the specific yield method.

2.3.1. Auger electron yield

One can measure the intensity of a specific Auger decay channel of the core hole. The energy of the Auger electron is not dependent on the energy of the incoming X-ray and from the universal curve [Sea79] it is found that the mean free path of a 500 eV Auger electron is of the order of 20 Å. Hence the number of Auger electrons emitted is equal to the number of core holes which are created in the first 20 Å from the surface. Because the mean free path of the incoming X-ray is of the order of 1000 Å, the number of core holes created in the first 20 Å is equal to the absorption cross section. Effectively the Auger electron yield method is a measurement of only 20 Å of material; hence the Auger electron yield is rather surface sensitive.

2.3.2. Fluorescence yield

Instead of the Auger decay, the fluorescent decay of the core hole can be used as the basis for the absorption measurement. The amount of fluorescent decay is increased with energy [Cit76], and a comparison of the amount of Auger decay with fluorescent decay shows that for the atomic number $Z \leqslant 20$ Auger decay dominates for all core levels and for $Z \leqslant 50$ Auger decay dominates all edges apart from the K edges for which fluorescent decay starts to dominate [Fug90]. Thus for the 3d metals, the K edges show strong fluorescence and all other edges mainly Auger decay. The photon created in the fluorescent decay has a mean free path of the same order of magnitude as the incoming X-ray, which excludes any surface effect. However, it means that there will be saturation effects if the sample is not dilute. That is, in the limit that there is only one absorption process, all X-ray photons which enter the material contribute to the fluorescence yield signal; hence its intensity will not be equal to the absorption cross section. The relation between the intensity of the fluorescence yield (I_f) and the absorption cross section (σ) is [Jak77]

$$I_f \approx \frac{\sigma_x(E)}{\sigma_x(E) + \sigma_b(E) + \sigma_x(E_f) + \sigma_b(E_f)} \quad (1)$$

For dilute materials, that is if the background absorption (σ_b) dominates the absorption of the specific edge (σ_x), the measured intensity is approximately equivalent to the absorption coefficient ($I_f \approx \sigma_x$). For less dilute materials the spectral shape is modified and the highest peaks will

appear compressed with respect to the lower peaks, known as saturation effects. For a given material the background absorption is known and in principle can be corrected for afterwards. However this correction procedure affects the statistics considerably. For concentrated systems, ($\sigma_x > \sigma_b$), the spectral modifications are too large for a sensible analysis. The $M_{4,5}$ edges of rare earths and to a lesser extent also the $L_{2,3}$ edges of transition metals are relatively strong; hence the fluorescence yield signal will be saturated for the pure metals. Compounds with low-Z elements will also show distorted X-ray absorption spectra. The oxygen K edge of metal oxides will show relatively small saturation effects, especially if some high-Z elements are present as is the case for $YBa_2Cu_3O_{7-\delta}$ and related compounds [Tro90]. Equation (1) shows that apart from saturation effects, there can be effects due to so-called self-absorption. If the fluorescent decay of a core hole takes place at an energy (E_f) which is strongly reabsorbed, the spectral shape is modified in a rather complicated manner and the spectrum is difficult to interpret. The large escape depth makes fluorescence yield suited for the measurement of impurities, which are difficult to measure with a surface sensitive technique such as Auger yield. The suitability of fluorescence yield for impurities, for example metal ions in bioinorganic cluster compounds or even complete enzymes, has led to large efforts in the development of fluorescence yield detectors [Cra88, Cra91a].

2.3.3. Ion yield

Another decay product of the core holes is ions. If the absorption process takes place in the bulk and the core hole decays via an Auger process a positively charged ion is formed, but due to further decay and screening processes the original situation will be restored after some time. However, if the absorption process takes place at the surface, the possibility exists that the atom which absorbs the X-ray will be ionized by Auger decay and escape from the surface before relaxation processes can bring it back to the ground state. If the escaping ions are analysed as a function of X-ray energy the signal will again be related to the absorption cross section. Because only atoms from the top layer are measured, ion yield is extremely surface sensitive. The mere possibility of obtaining a measurable signal from ion yield means that the surface is irreversibly distorted, but as there are of the order of 10^{13} surface atoms per mm^2, this does not necessarily mean that a statistically relevant proportion of the surface is modified. The possibility of using ion yield is highly material dependent and it is expected that the highest cross sections will be obtained for ionic solids. The method has been demonstrated for calcium atoms in the surface layer of CaF_2 [Him91].

2.3.4. Total electron yield

The most abundant yield detection technique, which is also the most unclear in its nature, is total electron yield. The difference with Auger electron yield is that the energy of the outgoing electrons is not selected and all escaping electrons are counted. It is clear that the signal is dominated by secondary electrons which are created in the cascade process of the Auger decay electrons [Erb88, Hen79]. The ease of detection and the large signal make total electron yield a much used technique, but questions which remain are the specific processes which take place and specifically the probing depth and the related surface

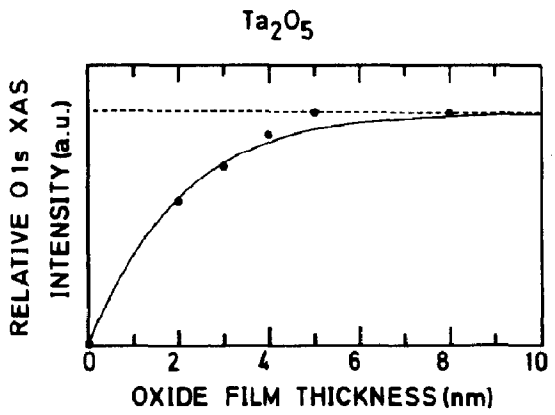

Fig. 5. Relative oxygen K edge X-ray absorption intensity as a function of the thickness of the Ta_2O_5 layer (from [Abb92b]).

Table 1
Probing depths of yield detection of soft X-ray absorption experiments of 3d metal oxides

Detection technique	Probing depth/Å
Ion yield	≈ 2
Auger electron yield	≈ 20
Total electron yield	≈ 40
Fluorescence yield	> 1000

sensitivity are only roughly known. An estimate for the probing depth is to use the Auger probing depth as the lower boundary and something of the order of 200 Å as the upper boundary. As the creation, migration and escape of secondary electrons will be material dependent, the probing depth of total electron yield will be material dependent.

A quantitative study of the mean probing depth of total electron yield for the oxygen K edge of thin layers of Ta_2O_5 on tantalum metal has been studied by Abbate et al. [Abb92b]. The tantalum oxide overlayers can be prepared with great accuracy and they are stable with respect to further oxidation if the layers have a thickness of 20 Å or more [San83]. Figure 5 shows the results for a layer thickness between 20 and 80 Å. The figure shows that total electron yield signal is already saturated for layers of the order of 40 Å. More details concerning the processes which determine the probing depth are given in [Abb92a, Erb88, Hen79, Kro90]. In Table 1 the estimates of the probing depths of the different yield methods are collected.

3. Electronic structure models

This section sketches the models which are used to describe the electronic structure of transition metals and their compounds. The two basic electronic structure models are (1) the Hartree–Fock (HF) approximation and (2) the local spin density (LSD) approximation to density functional theory (DFT). While LSD and its extensions/modifications dominate solid state physics, the quantum chemistry domain is dominated by models which use HF as their starting point. In this section HF (3.1) and LSD (3.2) are introduced. The subsequent sections discuss some of the extensions of HF and LSD, such as the generalized gradient approximation (GGA) (3.3), the GW approach (3.4), short range model Hamiltonians (3.5), the inclusion of the Coulomb interaction (U) in LSD (3.6), the self-interaction correction (SIC) (3.7), orbital polarization (OP) (3.8), the ligand field multiplet (LFM) model (3.9) and recent extensions based on multiconfigurational HF descriptions (3.10).

For solids in general LSD overbinds and the band gap is too small, while for HF the band gap is too large. In a sense most of the recent extensions can be viewed as an effort to combine the good points of HF and LSD to arrive at a more accurate description of the ground state.

3.1. The Hartree–Fock (HF) approximation

A well established approximation to determine the electronic structure is the Hartree–Fock (HF) approximation (presented text is based on [Ing91]). It is built on two basic notions. (1) The interaction of the electrons is described by the electrostatic potential, the Hartree potential (V_H)

$$V_H(r) = \sum_j \int dx' \phi_j(x') \phi_j^*(x') \frac{1}{r - r'} \qquad (2)$$

(2) The second ingredient of HF is the antisymmetric structure of the wavefunction which gives rise to the exchange interaction (V_x). V_x acts non-locally on the wavefunction. Apart from the Hartree and exchange potentials HF contains the kinetic term (V_k) and interaction with the nuclei (V_N). In bracket notation the eigenvalue problem is given as

$$E = \sum_i \langle i|V_k + V_N|i\rangle + \langle ij|V_H|ij\rangle + \langle ij|V_x|ji\rangle \qquad (3)$$

A self-consistent HF calculation gives the ground state energy E; the ground state wavefunction is given as a Slater determinant: an antisymmetrized determinant of the one-electron orbitals. An important omission in HF is the neglect of

correlation. With correlation is meant the notion that as two electrons repel each other, their position and momentum are not independent. In HF correlations are not included, apart from a partial effect for parallel spin from exchange. In general Hartree–Fock overestimates the band gap. For example in the case of $CaCuO_2$ a HF gap of 13.5 eV is to be compared with an experimental band gap of 1.5 eV [Mas92b].

3.2. *The local spin density (LSD) approximation*

Since the establishment of the density functional theorem (DFT), stating that the ground state energy can be expressed as a function of the electron density [Hoh64], and the practical implementation of this theorem in the local (spin) density approximation (LSD) [Koh65], solid state calculations based on this formalism have become important. This is not only to determine the total energy but also to obtain a picture of the electronic structure in terms of the density of states, which in turn is used to analyse spectra.

As in HF the kinetic, nuclear and Hartree potentials are used. The difference is that exchange and correlation effects are described by a combined potential V_{xc}. All potentials are local functions of the electron density n. All complications are collected in the exchange-correlation potential, for which it is assumed that in a solid its value is equal to that of a homogeneous electron gas for a particular n. Thus for the spin-polarized version the potential is given as

$$V_{LSD}[n^+, n^-] = V_k + V_N + V_H + V_{xc} \qquad (4)$$

For $V_{xc}[n^+, n^-]$ several alternative formulations are used and for details the reader is referred to review papers on LSD, for example [Jo89b]. The electronic structure and properties of solids are described with a number of alternative realizations of LSD. These methods vary in the use of plane waves (pseudo-potentials and augmented plane waves (APW)) or spherical waves (augmented spherical waves (ASW)); the use of fixed basis sets such as the linear combination of atomic orbitals (LCAO); the use of the electron scattering formulation, such as real space multiple scattering (MS) and Koster–Koringa Rostoker (KKR); linearized versions, such as linearized muffin tin orbitals (LMTO) and linearized APW (LAPW). For each of these methods in general several computer codes exist. Some methods exist in versions for spin-polarized calculations, the inclusion of spin–orbit coupling, fully relativistic codes, full potentials, spin-moment or direction restricted calculations, etc. Some recent reviews include [Jo89b, And87, Zel92].

A usual picture to visualize the electronic structure of a transition metal compound, such as oxides and halides, is to describe the chemical bonding mainly as a bonding between the metal 4sp states and the ligand p states, forming a bonding combination, the valence band and empty antibonding combinations. The 3d states also contribute to the chemical bonding with the valence band which causes them to be antibonding in nature. This bonding, taking place in a (distorted) cubic crystalline surrounding, causes the 3d states to be split into the so-called t_{2g} and e_g manifolds. This situation is visualized for a TiO_6^{8-} cluster in Fig. 6(a). For comparison the oxygen 1s X-ray absorption spectrum is given. In Fig. 6(b) this picture is modified for a partly filled 3d band. The example given is for a FeO_6^{9-} cluster. The 3d band is split by the crystal field splitting and a large exchange splitting.

This qualitative description of the electronic structure of transition metal compounds can be worked out quantitatively within L(S)D: in [Mat72a, Mat72b] a systematic study was made of the band structures of the 3d monoxides. The qualitative picture given above was verified, but in the calculations it was found that the dispersion of the 3d bands is larger than the crystal field splittings, with the result that all monoxides were calculated to be metallic, in conflict with the experimental findings. An important improvement of the L(S)D calculations, already suggested in [Mat72a], came with the inclusion of spin and the correct description of the magnetic structure of the monoxides [And79, Ogu83, Ogu84, Ter84,

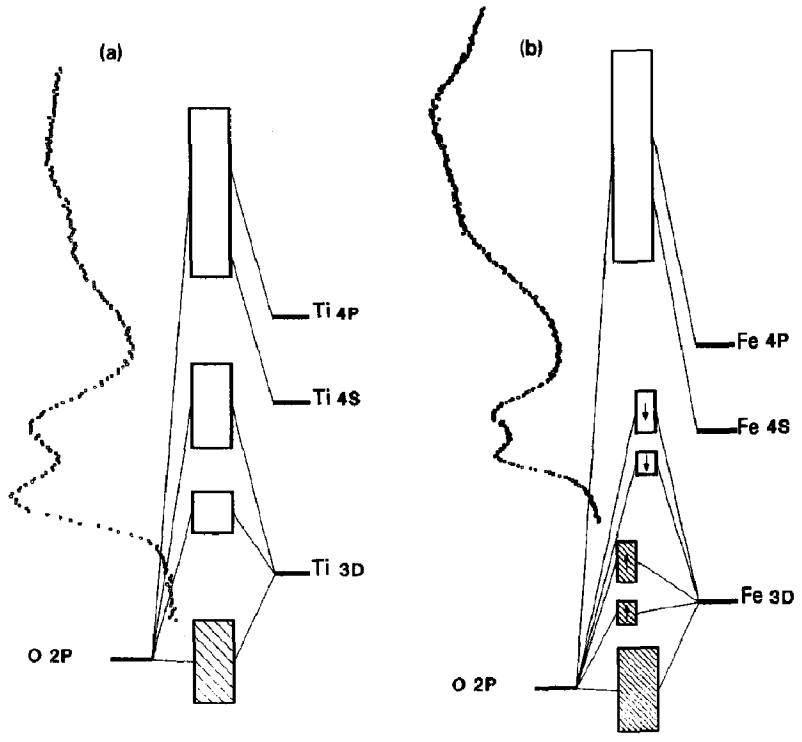

Fig. 6. Schematic band picture of (a) a TiO_6^{8-} cluster and (b) a FeO_6^{9-} cluster. Ti^{4+} has an empty 3d band and Fe^{3+} contains a half filled 3d band.

Yas83]. With the experimentally found antiferromagnetic coupling in the (111) direction it was found from LSD calculations that both MnO and NiO are insulators. In MnO all spin-up states are filled and all spin-down states empty, similar to the situation in Fig. 6(b). Figure 7, reproduced from [Ogu84], shows the result of the LSD calculation for NiO. A band gap of 0.3 eV is found and the occupied states can be roughly divided into an oxygen 2p band at about 6 eV below the Fermi level and a nickel 3d band just below E_F. From the spin-projected nickel 3d states it can be seen that, in first approximation, the spin-down states are rigidly shifted over about 1.2 eV. The $t_{2g}^{\downarrow}$ states are positioned at the same energy as the $e_g^{\uparrow}$ states, or in other words the ligand-field splitting roughly equals the exchange splitting.

3.2.1. The real space multiple scattering formalism

Particularly for hard X-rays, the absorption spectra are calculated with a real space multiple scattering formalism [Vvd92]. It has been shown that if worked out rigorously within its mathematical framework, the real space multiple scattering result is identical to the result obtained from band structure [Jon68, Nat86a, Reh93]. See Section 8 for further discussion.

3.3. The generalized gradient approximation

The generalized gradient approximation (GGA) has been developed to overcome the limitations met in the use of LSD. The goal of GGA is to come closer to the limit of the exact exchange-correlation potential within DFT. In comparison with experiment LSD gives a too strong bonding and hence too small optimized lattice parameters. This result has been linked to the use of a localized potential. In GGA this is replaced with a potential which is not only dependent on the electron density n, but also on its gradient (∇n). The exchange-correlation potential is $V_{xc}[n^+, n^-, \nabla n^+, \nabla n^-]$ [Lan80].

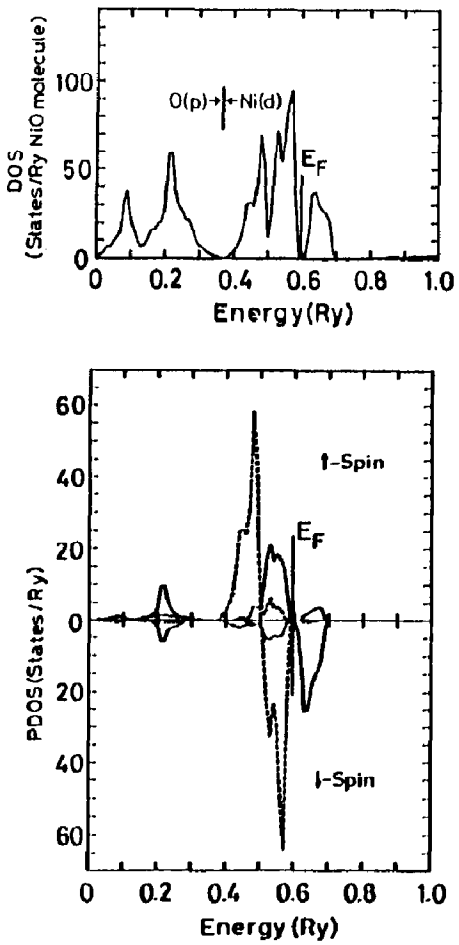

Fig. 7. Total density of states (top) and projected Nid projected density of states (bottom) of an LSDA calculation of NiO (from [Ogu84]).

For transition metals an important result of a GGA calculation is that the ground state of iron is predicted in agreement with experiment. While LSD finds a paramagnetic face-centred cubic (P-FCC) ground state, GGA finds a ferromagnetic body-centred cubic (F-BCC) phase [Bag89]. There are two energy effects of GGA compared to LSD which can be approximated as follows: (1) there is an energy lowering effect linear in the Wigner–Seitz radius which favours the BCC phase; (2) for a fixed radius GGA favours a magnetic moment, which lowers the energy of the ferromagnetic phase. The combination of these effects gives the F-BCC phase at lowest energy [Bag89].

For the precise formulation of the exchange-correlation potential in GGA a number of alternatives exist, normally indicated by the first letters of the authors. Influential formulations are those of Langreth–Mehl–Hu (LMH) [Hu85, Lan83], Perdew–Wang (PW) [Per86a, Per92a, Per92b] and Becke [Bec88]. These GGA potentials are "semi-empirical" in the sense that they make a particular choice for, for example, the real-space-cutoff, which is partly guided by the correspondence to experiment. For details of the potentials the reader is referred to the original literature which is collected in [Per92b].

3.4. GW *calculations*

A well defined model to describe electronic excitations is the so-called *GW* approach [God88, God92, Hed65, Hed69] in which the Green function G calculated with a screened Coulomb interaction W is used to calculate the excitation energies. In [Ary92] it is noted that one can divide W into an exchange part W_x and a correlation part W_c. Then a "GW_x" calculation can be identified with HF. The calculation requires a non-local, energy-dependent so-called self-energy operator. A *GW* calculation gives the density of (quasi-particle) states for the occupied states of the $N-1$ system and the empty states of the $N+1$ system. Hence it gives a direct description of (inverse) photoemission spectra. This is in contrast to LSD calculations, which can be considered as *GW* calculations with a local, energy-independent self-energy operator, thereby yielding an "N-particle density of states". The actual calculation of excitation energies with *GW* is a large task, especially for transition metals, because of the narrow 3d bands, and to my knowledge only for nickel has a *GW* calculation been performed [Ary92]. As far as the valence band is concerned the main effect of *GW* is a compression of the 3d band. The ordering of the bands is not altered from LSD. A *GW* calculation is in progress for NiO [Ary93].

3.5. The short range ("Anderson impurity") models

A clear case of disagreement between LSD calculations and experimental results can be found in the XPS/BIS data of NiO. Sawatzky and Allen [Saw84] showed that in NiO XPS/BIS gives a band gap of about 4.3 eV, compared with 0.3 eV from LSD. For clarity I note that formally LSD should not yield the correct band gap, but the large discrepancy with experiment shows that "something is missing" in LSD. The missing factor is the incomplete treatment of the Coulomb interaction U, as indicated in [Fuj84a, Saw84]. The main result of the inclusion of U is that the states closest to E_F are dominated by oxygen 2p character, in contrast to the LSD result which puts the 3d states closest to E_F. This discrepancy will be discussed in more detail below.

A crucial phenomenon for transition metal oxides is the fact that it costs energy to transfer an electron from one metal-ion to another, because of strong two-electron Coulomb integrals $\langle 3d, 3d|1/r|3d, 3d\rangle$, comprising U_{dd}. In LSD calculations this effect is not incorporated correctly and each transition metal contains the same number of (completely delocalized) electrons. In practice to put a number to the occupation one usually assigns all electrons within a particular radius to that atomic site. The fact that U_{dd} is not small means that it costs energy to vary the occupation number of the metal sites and in the extreme limit of infinite U_{dd} each metal site contains an integer number of localized 3d electrons. Models have been built focusing on a correct description of the Coulomb interaction, at the expense of less-complete descriptions of other ingredients [Hub63, Hub64, Hub67]. The model Hamiltonians built from this approach usually consist only of the 3d states and the oxygen 2p states. The Anderson impurity model [Ano61] comprises the energy positions of a localized state ε_d and delocalized states ε_p, the Coulomb interaction U_{dd} and the hopping terms t_{pd} and t_{pp} [Fuj84a, Fuj84b]. The model is often extended by including the Coulomb interaction of the 2p states U_{pp}, U_{pd}, sometimes denoted as the Falicov–Kimball model [Gie91] or in the context of copper oxides as the three-band Hubbard model [Eme87]. The Anderson impurity model and similar short range models are crucial for a sensible description of photoemission, inverse photoemission and core level XPS of transition metal compounds [Saw88].

3.5.1. Calculation of parameters in model Hamiltonians

In general the parameters in the Anderson impurity model are optimized to describe the experimental data. An important goal would be to derive the parameters from an ab initio method. The idea is to start with the full Hamiltonian and to project out degrees of freedom which are not included in the model Hamiltonian [Gun90]. The delocalized electrons are projected out and the Coulomb interaction is renormalized to account effectively for this. The Coulomb interaction U and the energy of the localized state $\varepsilon_d - \varepsilon_p$ can be determined from a constrained LSD calculation [Ani91b, Ded84, Hyb89, Mcm88a, Mcm88b, Zaa88]. In a model study Gunnarsson [Gun90] pointed out that the consequences of projecting out delocalized states causes a renormalization of U, first order in V^{-1} (V is the hopping integral of the delocalized states). An additional result is that the hopping of the localized state (t_{pd}) is also affected (in second order). If the localized state is expanded as a function of its occupation, the hopping is affected, in this case strongly [Gun88b]. Also the Coulomb interaction of the localized state with delocalized state renormalized t_{pd} [Gun89b].

3.6. The inclusion of U in LSD calculations

There have been recent efforts to include U_{dd} in the LSD Hamiltonian [Ani91a, Ani92a]. In these so-called LSD + U calculations the total energy functional is expressed as the L(S)D energy corrected for U and the exchange parameter J. That is, with an LSD calculation the exchange splitting J is determined. It can approximately be assumed to

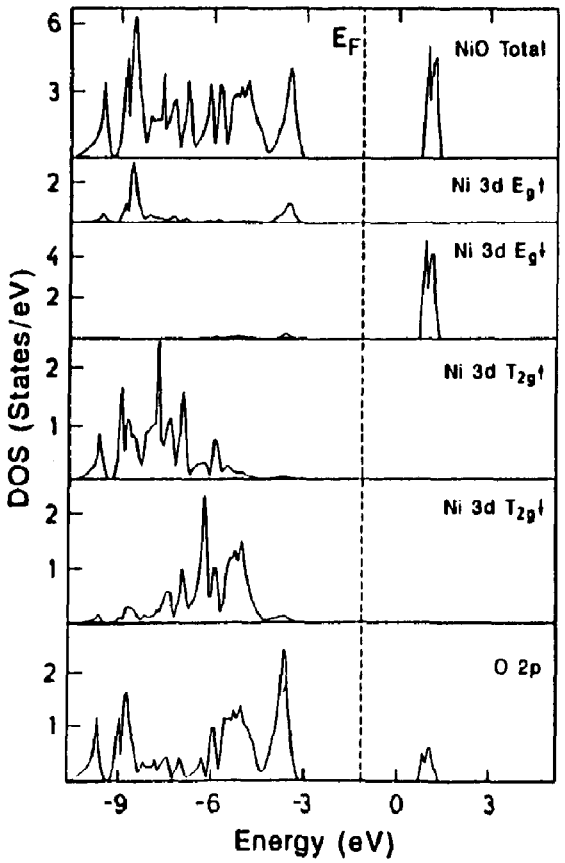

Fig. 8. Total and projected density of states of an LSD + U calculation of NiO (from [Ani91a]).

be k-independent. Also with the constrained LSD method U is determined as discussed above. Then the single particle potential is re-expressed as

$$V_{m\sigma} = V_{\mathrm{LD}} + U\sum_{m'}(n_{m'-\sigma} - n^0) + (U - J)\sum_{m'}(n_{m'\sigma} - n^0) \qquad (5)$$

where m and σ refer to orbital and spin momenta respectively. The spin-independent LD potential is corrected for the deviations from the average occupation (n^0). Figure 8, reproduced from [Ani91a], shows the result of an LSD + U calculation using this expression for the potential. The result is a valence band of a width of about 7 eV in which the oxygen and nickel character are strongly mixed. The top of the valence band is indeed dominated by oxygen character in agreement with the earlier Anderson impurity-model predictions [Saw84, Zaa86t].

As yet a number of problems have still to be solved: the choice of the potential to be used is not obvious and one can imagine a number of alternatives. For example one can make U (and n^0) symmetry dependent, etc. [Czy93]. A second uncertainty is the value of U. The method to calculate U first with LSD and then in the second step to include it in an LSD + U calculation offers an ab initio method, although it is not certain whether it presents the "correct value" of U within an LSD + U calculation.

3.7. *The self-interaction correction (SIC)*

An alternative approach to introduce the localization effect due to the two-electron integrals is to introduce a so-called self-interaction correction (SIC). In LSD calculations non-existing self-interactions are included in the electrostatic term and also in the exchange-correlation term. The effects are opposite and tend to cancel, and in fact for the case of an infinitely extended solution they do cancel. For clarity it is noted that the self-interactions are a consequence of LSD and do not occur in the "exact" solution of DFT. In a strongly correlated material the wavefunctions are not infinitely extended and a correction must be added to the Hamiltonian removing the effects of self-interaction, the SIC [Gun74, Ish90, Miy91, Per79, Per80, Sva88a, Sva88b, Sva90a]. In order to have the possibility of finding a localized solution of the LSD + SIC calculations, a symmetry breaking term is introduced. It is tested self-consistently if a localized solution is favoured over delocalization. For example for the 3d monoxides localized solutions are found for MnO to CuO in agreement with experiment [Sva90b, Szo93] and La_2CuO_4 is found to be an antiferromagnetic insulator with a LSD-SIC gap of about 2 eV, close to the experimental value [Sva92, Tem93]. In principle the result of a LSD + SIC calculation is "single particle"-like and one finds the eigen-

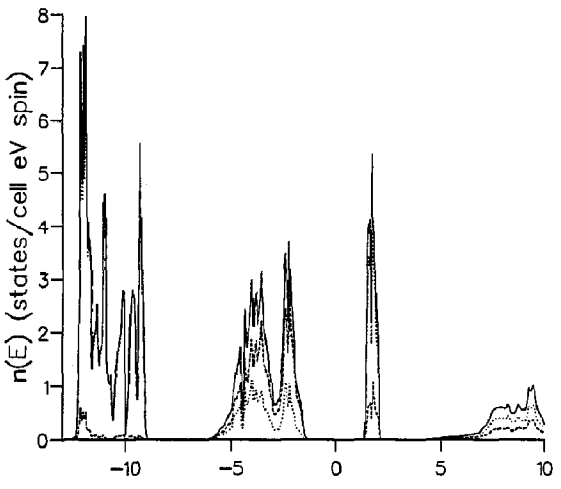

Fig. 9. Projected density of states of an LSD + SIC calculation of NiO. —, Total DOS; ···, Ni-projected DOS; – – –, oxygen projected DOS (from [Szo93]).

values of the ground state. As for normal LSD, one can relate the eigenvalues to excitation energies, though again there is no formal justification.

Figure 9, reproduced from [Szo93], shows the result of an LSD + SIC calculation. The band gap is close to the experimental value. The valence band is separated into two bands, an oxygen 2p-dominated band close to E_F and the nickel 3d band at about 6 eV lower energy. This result is (as far as energy positions are concerned) similar to the experimental XPS spectrum and the model calculations of Fujimori et al. [Fuj84a] and Zaanen et al. [Zaa85a].

3.8. *Multiplet effects (orbital polarization)*

In LSD one assumes the orbital contribution to the magnetic moment to be negligible and hence the different magnetic m_{lm} states are assumed to have equal average population ($\bar{m}_l$) [Sev93]. To enforce a non-statistical orbital occupation an additional term has been introduced in the LSD Hamiltonian [Eri90a, Eri90b, Nor90].

Recently Severin et al. [Sev93] separated the exchange integral into a spin part and an orbital part. The spin part can be identified with the Stoner-like exchange interaction J, included in LSD. The angular-part of the exchange integral is

Table 2
The Racah parameters and the Kanamori parameters given as a function of the Slater integrals

Racah	Slater	"Kanamori"	Slater
A	$F^0 - \frac{F^4}{9}$	U	$F^0 - \frac{2}{9}J$
C	$\frac{5F^4}{63}$	J	$\frac{1}{14}(F^2 + F^4)$
B	$\frac{9F^2 - 5F^4}{441}$	C	$\frac{1}{14}(\frac{9}{7}F^2 - \frac{5}{7}F^4)$
A	$F^0 - 0.070F^2$	U	$F^0 - 0.025F^2$
C	$0.050F^2$	J	$0.116F^2$
B	$0.013F^2$	C	$0.060F^2$

however (assumed to be) zero in LSD. This angular-part can be identified with the Kanamori C parameter, or the Racah B parameter, both as given in Table 2. For the Slater integrals experimental atomic values, or atomic HF values, are known accurately. For solids it is known that J is screened [Mar88]. Because for C no ab initio solid state information is known, it was assumed that the screening of C is equal to the screening in J [Sev93]. In Slater integral terms this identifies with an equivalent reduction of F^2 and F^4. Then with the inclusion of C, the orbital polarization (OP), the orbital and spin moments are calculated with LSD + OP. The results are in close agreement with experiment [Sev93].

It is noted that in this method of Severin et al. the full HF Coulomb and exchange integrals are calculated, but in the LSD + OP calculation the U part of the integrals is omitted. In other words, U is assumed to be zero, as in normal LSD calculations. Svane and Gunnarsson included in their LSD + SIC calculation the effects related to both U and C [Sva90a]. It can be said that, starting from local density, the effects of the Slater integrals formulated as U, J and C (see Table 2) are included as follows: LSD includes J, LSD + OP includes J and C and LDA + U includes J and U. In principle there are no objections to including C in an LSD + U description [Ani91a].

3.9. *Ligand field multiplet (LFM) model*

The ligand field multiplet (LFM) model describes the ground only in terms of the partly

filled 3d band. It is the simplest possible theory to describe the effects of the Coulomb and exchange integrals on the 3d band and hence to describe the symmetry of the ground state in the local symmetry for a transition metal ion in the solid [Grf64]. LFM theory is important for those experiments which are mainly sensitive to symmetry and hence those experiments which involve only the 3d band. This includes dd optical transitions, resonance experiments such as electron paramagnetic resonance (EPR) and as will be discussed in the next sections metal 2p X-ray absorption. Obviously LFM theory does not provide an ab initio calculation of the ground state in solids; it can be viewed as the simplest model Hamiltonian and the way to proceed to an ab initio determination would be to use the mapping of more complete Hamiltonians onto the LFM model. That is, if the Anderson impurity model Hamiltonian is determined ab initio one can go one step further and also delete the delocalized states to arrive at a single 3d band.

3.10. Multi-configurational approaches

Most of the preceding sections concentrated on the extension and improvement of LSD. This section discusses briefly some recent approaches which use HF as their basis. The extensions of HF basically deal with two types of shortcomings: (1) the inclusion of weak correlations, and (2) the inclusion of strong correlations where single Slater determinations no longer present good starting points. HF and extensions dominate the electronic structure determinations of molecules, which are discussed first.

Weak correlations can be included by parametrized, statistical, correlation corrections to HF [Cow81]; in other words one includes the electron density correlation functionals [Per86b]. A treatment based on perturbation theory was given by Møller and Plesset in 1934 [Mol34]. An influential method to include weak correlations is the coupled-electron-pair approximation (CEPA) [Ahl84, Mey71].

If strong correlations are important one has to leave the single Slater integral concept by including a specific set of configurations. These calculations can in general be called multi-configurational (MC) HF. Instead of Hartree–Fock one more generally uses the expression self-consistent-field (SCF) which denotes that the HF (like) equations are solved self-consistently using the variational principle [Dol91]. In 1973 Bagus and co-workers performed a MC calculation for the final state in 3s XPS which is dominated by the two configurations $3s^1 3p^6 3d^5$ and $3s^2 3p^4 3d^6$ [Bag73]. These two configurations are very strongly coupled by a 3s3d to 3p3p electron rearrangement process, the same process which causes the super Koster–Kronig Auger decay. There exist a number of generalized criteria to choose the configurations to be included. For example one can do a "first-order" CI (FOCI) [Jan88] by including all single excited states. Dolg et al. performed a MC-SCF calculation for cerocene (cerium sandwiched by two C_8H_8 rings), which constitutes a system with both strong (f states in cerium) and weak (other electrons) correlations [Dol91]. Recently Fulde and Stoll extended the CEPA calculations to a situation with more than one configuration. This then offers a way to include the strong correlations by MC-SCF and to include the weak correlations by CEPA [Ful91].

In going from molecules to solids a problem arises with respect to the embedding of the cluster for which an (MC) HF calculation is performed into "the solids". To account for the long-range Coulomb interactions the solid is often described as point charges around the cluster [Jan88].

4. Core excitations

This section describes the properties of core excitations, that is X-ray photoemission (XPS) and X-ray absorption (XAS). For the analysis of core spectroscopies it is necessary to describe the ground state, the final state and the transition cross section. The ground state electronic structure models have been discussed in the preceding section. In principle

the final state can be calculated with these models; however the core hole gives some additional complications. The core hole has three major effects. (1) There is a core electron less, hence the core potential is stronger as if the atomic number is increased by one. (2) Core states with an angular momentum give rise to a core state spin–orbit splitting. (3) Core states with an angular momentum also give rise to strong core valence Coulomb interactions. At present no ab initio method is able to account for these three effects.

For 1s edges effects (2) and (3) do not exist and the core hole potential is the only extra effect to be accounted for in the final state. It is possible to include a core hole potential in real space multiple scattering. Also in a LSD calculation this is possible, at the expense of a larger calculation, by using supercells. It is noted that LSD calculations give a reasonably correct picture of the empty density of states as the Coulomb interactions U do not affect the distribution of empty states in a first order approximation. This is relatively clear to see in the self-interaction framework: as only occupied states have (self) interactions in LSD, only occupied states are directly affected by SIC (see Section 3.7).

For 2p edges the strong core valence Coulomb interactions make impossible any analysis using only the distribution of empty states (as obtained from LSD, MS, etc.). This forces one to use model Hamiltonian descriptions, such as the Anderson impurity model (using atomic Slater integrals for the core valence Coulomb interactions) or even the ligand field multiplet model (using renormalized core valence Coulomb interactions).

4.1. The interaction of X-rays with matter

The interaction of X-rays with matter is described in many textbooks [Bas83]. The Hamiltonian describing this interaction is written as a function of the vector potential of the electromagnetic radiation A and the momentum of the electrons p. It contains terms in A^2 and $A \times p$. For the analysis of X-ray absorption it is sufficient to consider only $A \times p$. In general the dipole approximation can be used [Car90] and the probability for absorption of an X-ray is equal to a squared transition matrix element times a delta function describing the conservation of energy; Fermi's golden rule

$$\sigma = \frac{8\pi e^2 \omega^3 n}{hc^3} |\langle \Phi_f | \mathbf{p}_q | \Phi_i \rangle|^2 \delta_{E_f - E_i + E_{h\nu}} \tag{6}$$

The momentum operator $\mathbf{p}_q$ (q accounts for the polarization degrees of freedom) can be replaced by the position operator $\mathbf{r}$ as $[\mathbf{r}, \mathscr{H}] = (ih/m)\mathbf{p}$; however this replacement is exact only if the same Hamiltonian is used in the initial and final state. Equation (6) in principle refers to a final state with infinite lifetime. If the finite lifetime is accounted for the δ function is replaced by a Lorentzian.

In theoretical treatments of the X-ray absorption cross section it is customary to reformulate Eq. (6) in terms of a correlation function [Gun83, Zaa86a]. The squared matrix element $|\langle \Phi_f | \mathbf{r} | \Phi_i \rangle|^2$ is rewritten as $\langle \Phi_i | \mathbf{r} | \Phi_f \rangle \times \langle \Phi_f | \mathbf{r} | \Phi_i \rangle$. The radial operator $\mathbf{r}$ is rewritten in second quantization as $T = \sum_v W_v \phi_v^\dagger \phi_c$; ϕ_c annihilates a core electron and $\phi_v^\dagger$ creates a valence electron. The finite lifetime of the excited state Γ is included and the delta function $\delta_{E_f - E_i + E_{h\nu}}$ is reformulated as (one over π times) the imaginary part of the Green function $\mathscr{G}$

$$\mathscr{G} = \frac{1}{\mathscr{H} - E_i + E_{h\nu} - \frac{1}{2} i\Gamma} \tag{7}$$

After these modifications the total equation takes the shape of a correlation function

$$\sigma \approx -\frac{1}{\pi} \mathscr{S} \langle \phi_i | T^\dagger \mathscr{G} T | \phi_i \rangle \tag{8}$$

T and $T^\dagger$ project the initial state wavefunction on a series of final states for which the Green function is evaluated. This correlation function formulation is also used in the real space multiple scattering formulation of X-ray absorption (Section 8). The use of correlation functions like this has led one to remark that "everything is a ground state property", because if ϕ_i is known

the spectrum can in principle be calculated. This Platonian interpretation can be countered by the Aristotelian remark that one only knows nature, if one knows its movement, in the sense of change. This puts the transition operator T at the centre of attention. ϕ_i is pure "matter" and hence only potential; it is actualized by T (following Aristotle).

4.1.1. Selection rules for X-ray absorption

In the case of an atom the wavefunctions in Eq. (6) can be given J and M (or M_J) quantum numbers. The matrix element $\langle\phi(JM)|\mathbf{r}_q|\phi(J'M')\rangle$ can be separated into a radial and an angular part according to the Wigner–Eckart theorem [Cow81]

$$\langle\phi(JM)|\mathbf{r}_q|\phi(J'M')\rangle = (-1)^{J-M}\begin{pmatrix} J & 1 & J' \\ -M & q & M' \end{pmatrix}\langle\phi(J)\|\mathbf{r}_q\|\phi(J')\rangle \quad (9)$$

The triangular relations of the 3J-symbol determine the selection rules for X-ray absorption. They read as follows: because the X-ray has an angular momentum of $l_{h\nu} = +1$, conservation of angular momentum gives $\Delta l_i = +1$ or -1; the angular momentum of the excited electron differs by 1 from the original core state. As X-rays do not carry spin, conservation of spin gives $\Delta s_i = 0$. Given these restrictions the overall momentum quantum number cannot be changed by more than 1; thus $\Delta J = +1$, 0 or -1, with $J + J' \geqslant 1$. The magnetic quantum number M is changed according to the polarization of the X-ray, i.e. $\Delta M = q$.

For linearly polarized X-rays impinging on a sample under normal incidence $q = \pm 1$ and for grazing incidence $q = 0$. This gives a difference in the value of the 3J-symbol, and hence (in potential) a polarization dependence. For circularly polarized X-rays a polarization dependence is found for a magnetic ground state. For an atomic non-magnetic ground state $M = \pm J$ and the 3J-symbol is identical for $q = \pm 1$. The rules for dichroism are discussed in more detail in Section 6.

4.1.2. Extended final states

For extended final states (the Bloch-like wavefunctions in density functional methods) J is not a good quantum number and the only selection rules are $\Delta l_i = +1$ or -1 and $\Delta s_i = 0$. In case of an excitation from a 1s core state only p final states can be reached and from a p core state s and d final states can be reached. The absorption cross section (σ) is reformulated as the matrix element squared times the local projected density of states (n_l) [Mul84]

$$\sigma \approx |\langle\Phi^v_{l-1}|\mathbf{r}_q|\Phi^c_l\rangle|^2 n^*_{l-1} + |\langle\Phi^v_{l+1}|\mathbf{r}_q|\Phi^c_l\rangle|^2 n^*_{l+1} \quad (10)$$

where n^* denotes the final state density of states, which should be used according to the final state rule [Von79, Von82]. Φ^v and Φ^c denote respectively the valence wavefunction and the core wavefunction (see Section 8 for more details).

4.2. XAS versus XPS

In core X-ray photoemission spectroscopy (XPS) the electron is excited to an energy high above the Fermi level and it can be considered as a free electron. The shape of the XPS spectrum is determined by the reaction of the system on the core hole. For example for 2p XPS an important effect is the two-electron integral $\langle 2p, 3d|1/r|2p, 3d\rangle$, giving rise to a core hole potential U_{cd}. The core hole spin–orbit coupling is also important and gives rise to the $2p_{3/2}$ and $2p_{1/2}$ edges.

In X-ray absorption spectroscopy (XAS) the energy of the X-ray is varied through a core level and an electron is excited to a state just above the Fermi level. If no reaction with the core hole takes place, the shape of the XAS spectrum will reflect the density of empty states (times transition strengths). Because in X-ray absorption the excited electron is not free, the dipole transition poses strong selection rules to the final state. This gives X-ray absorption its site and symmetry selective properties and for example oxygen 1s X-ray absorption will reflect the oxygen p-projected density of states.

However as for XPS the effect of the core hole is important and in fact it localizes the problem and necessitates the use of a short range model. The higher-order terms of the core hole interaction with the 3d band are also important. The two electron integrals $\langle 2p, 3d|1/r|2p, 3d\rangle$ and $\langle 2p, 3d|1/r|3d, 2p\rangle$ contain the higher-order terms F^2, G^1 and G^3. They have large values and give rise to a series of final states with different symmetries and energies: the final state multiplet. In general these effects are denoted as multiplet effects. For photoemission the dipole selection rule is relaxed and all final state symmetries are allowed. There is an important difference between 2p XPS and 2p XAS with regard to the relative importance of charge transfer versus multiplet effects. This can be shown nicely with the use of the short range model.

4.3. Short range models for core spectroscopies

Model Hamiltonians which explicitly include the Coulomb interaction U in the Hamiltonian include, (1) the single band or Hubbard model, (2) the Anderson impurity model comprising both a localized and an itinerant band, (3) the Kimball–Falicov model including also U_{pd}, etc. In Fig. 10 a schematic density of states is given for a 3d transition metal compound. In the short range (Anderson impurity) model as used for core spectroscopies, only the 3d states and the ligand p band are retained. The 3d band is considered localized, with an energy ε_d and a Coulomb repulsion energy U_{dd}. The 3d states interact with ligand p states at energy position ε_p. The hopping matrices are denoted as t_{pd}. Also the ligand p states interact with each other via t_{pp}. This short range model can be used for a cluster describing the transition metal ion and its nearest neighbour ligand ions. This approach has been applied to core spectroscopy by Fujimori et al. [Fuj84a, Fuj84b]. The ligand states can also be described as bands by including the k-dependence of the p band. Each transition metal atom contains localized 3d states but all other states are in principle described as bands. This approach has been introduced for

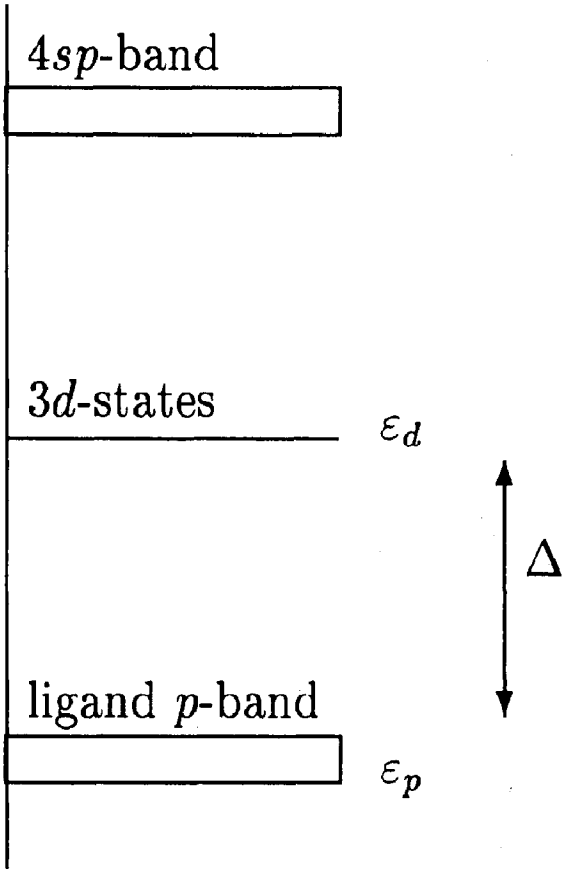

Fig. 10. Schematic density of states of a 3d transition metal compound.

spectroscopy of cerium compounds by Gunnarsson and Schönhammer [Gun83, Gun85] and has been adapted to transition metal compounds by Zaanen et al. [Zaa86a, Zaa86t].

The Hamiltonian which is used in the short range (Anderson impurity) model is

$$\mathcal{H} = \varepsilon_d n_d + \sum_k \varepsilon_{pk} n_{pk} + t_{pd} \sum_k (a_d^\dagger a_{pk} + a_{pk}^\dagger) + U_{dd} n_d n_d \qquad (11)$$

In this equation second quantization is used and $a_d^\dagger$ denotes the creation of the localized d state; n_d ($\equiv a_d^\dagger a_d$) is the occupation-number operator of the localized state. To describe the ground state the ionic ansatz (starting point) is a specific 3d

configuration $3d^N$, as given by the formal valency of the ion. If the hopping of this localized state with the ligand p band is considered, this gives rise to $3d^{N+1}\underline{L}$ configurations with an energy $\varepsilon_d - \varepsilon_p$, which is also denoted as Δ, the charge transfer energy.

The electronic configuration of the ground state of the compound is given by a linear combination of $3d^N + 3d^{N+1}\underline{L}$ plus, if necessary, the other more excited states. It is determined by three parameters, U_{dd}, Δ and t_{pd}, plus the shape of the band. The symmetry is in general determined by the formal valency and is not altered by charge transfer effects, provided the ground state is not dominated by a $3d^{N+1}\underline{L}$ configuration. For example Ti^{4+} in TiO_2 has a ground state $3d^0 + 3d^1\underline{L} + 3d^2\underline{LL}'$; its symmetry is $^1A_1$ and is not modified by charge transfer.

In the final state of both 2p XPS and 2p XAS a core hole is present which couples strongly to the 3d states via $U_{\underline{c}d}$, which pulls down states with extra 3d electrons. The core hole in principle also couples to other valence states (see Appendix A), but in most cases these couplings are assumed to be effectively included in $U_{\underline{c}d}$ [Saw88]. The final state Hamiltonian becomes

$$\mathcal{H} = \varepsilon_d n_d + \sum_k \varepsilon_{pk} n_{pk} + t_{pd} \sum_k (a_d^\dagger a_{pk} + a_{pk}^\dagger a_d) + U_{dd} n_d n_d + \varepsilon_c n_c \qquad (12)$$

The four parameters, Δ, t_{pd}, U_{dd} and $U_{\underline{c}d}$ determine the shape of the 2p XPS and 2p XAS spectra (neglecting multiplet effects). The energy of the core state (ε_c) determines the energy position of the 2p edge. (Also the core hole spin–orbit coupling is included: see next section.) The situation for a typical charge transfer insulator ($\Delta = 3$, $U_{dd} = 7$ eV) is visualized in Fig. 11 [Deg93c]. The ionic configurations are given and the effects of hybridization are not included. The arrows indicate the transitions in both XPS and XAS. In XPS the ordering of the final states is changed because of the effect of $U_{\underline{c}d}$. The energy difference between the localized state and the band, Δ_f(XPS) is given by $\Delta - U_{\underline{c}d}$, which for charge transfer insulators is negative. In XAS the ordering of states in the final state does not change because the 2p electron is excited directly into a 3d state, which causes the counteracting effects of U_{dd} and $U_{\underline{c}d}$. In general $U_{\underline{c}d}$ is slightly larger than U_{dd}, but

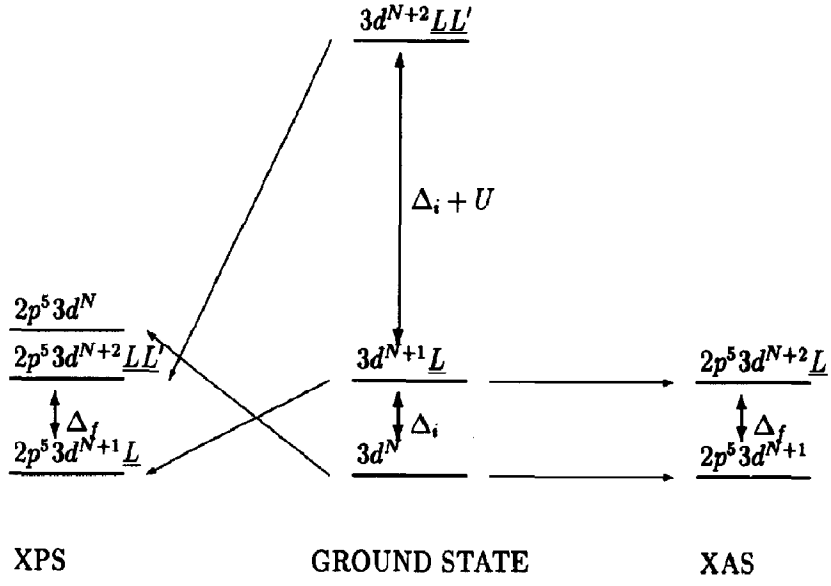

Fig. 11. 2p XPS and 2p XAS in the charge transfer model, neglecting the effects of hybridization. The configurations with lowest energy in the initial and the two final states are set to zero. $\Delta_f = \Delta_i + U_{dd} - U_{\underline{c}d}$. The arrows indicate the transitions in both 2p XPS and 2p XAS.

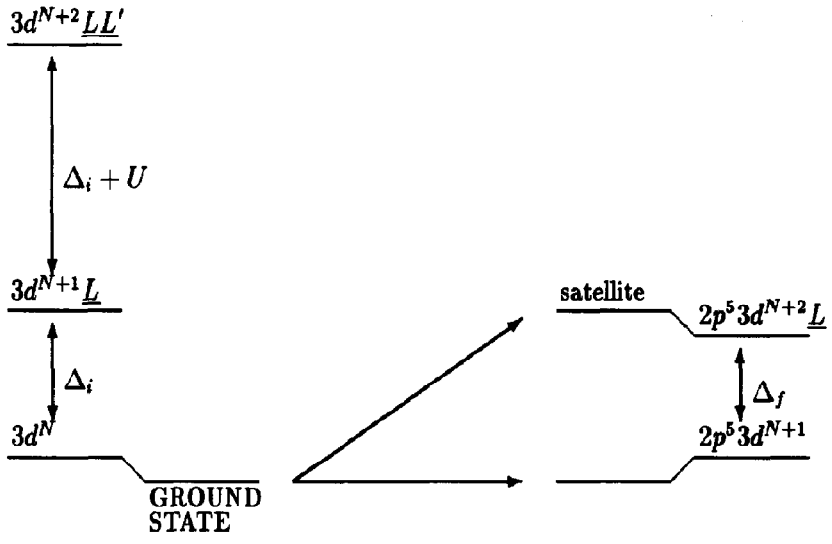

Fig. 12. The effects of hybridization on 2p XAS. If $\Delta_f = \Delta_i$ (and $t_f = t_i$) only the transitions to the lowest mixed configuration in the final state occur (see text).

here they are for simplicity taken as equal. This has the consequence that $\Delta_f(\mathrm{XAS}) = \Delta + U_{dd} - U_{\underline{c}d} \approx \Delta$.

In Fig. 12 the effects of hybridization are included for 2p XAS. The ground state is formed from a combination of $3d^N$ and $3d^{N+1}\underline{L}$. The two configurations in the final state form a bonding and antibonding combination. With the restriction that $U_{\underline{c}d} \approx U_{dd}$ all intensity goes to the bonding combination of the two final state configurations and no satellite is present. The ground state is written as $\Phi_i = \sin\alpha[3d^N] + \cos\alpha[3d^{N+1}\underline{L}]$ and the final states as $\Phi_{f1} = \sin\beta[2p^5 3d^{N+1}] + \cos\beta[2p^5 3d^{N+2}\underline{L}]$ and $\Phi_{f2} = -\cos\beta[2p^5 3d^{N+1}] + \sin\beta[2p^5 3d^{N+2}\underline{L}]$. Then the intensity of the main peak is given as $\cos^2(\beta - \alpha)$ and the satellite equals $\sin^2(\beta - \alpha)$ [Oka92b]. If $U_{\underline{c}d} \approx U$ and $t_f \approx t_i$, then $\alpha \approx \beta$ and the satellite has zero intensity. One set of exceptions to this "rule of no-satellite" can be found at the end of the transition metal series. Systems which are dominated by $3d^9$ will have an altered final state because some of the configurations in the final state are not possible because they would have to contain more than ten 3d electrons. Hence their final state electronic configuration will have to adapt to this situation which can give rise to an increased intensity for the satellites. This will also influence systems with a $3d^9\underline{L}$ ground state such as $NaCuO_2$.

In the case of 2p XPS the situation is rather different. In general there are three low-lying states in the final state and their ordering has been changed with respect to the ground state. Under complete neglect of hybridization only the $2p^5 3d^N$ final state can be reached. If hybridization is turned on the two lower states gain in intensity, partly due to ground state hybridization but mainly due to final state hybridization and additionally due to the interference terms. This has been shown nicely for the nickel halides where all model parameters can be chosen equal with only the charge transfer (Δ) decreasing from fluoride to iodide, giving rise to a large variety in spectral shapes [Zaa86a]. Recently it has been shown that in the case of the 2p XPS spectrum of NiO it is necessary to extend the impurity model to a larger cluster and to allow for non-local screening effects, that is the formation of completely screened core hole ($\underline{c}d^9$ instead of normal $\underline{c}d^9\underline{L}$) while the valence hole moves to a neighbouring nickel to form a $d^8\underline{L}$ state [Vee93a, Vee93b].

From this discussion it can be concluded that the 2p XPS spectrum will contain large charge transfer

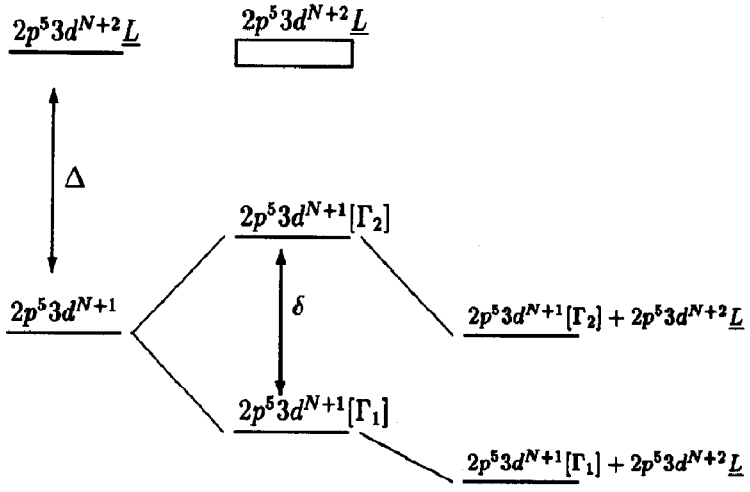

Fig. 13. The interplay of multiplet and charge transfer effects. If, as indicated, $\Delta > \delta/2$, the net result is a compression of the multiplet structure. If $\Delta < \delta/2$ the effects of charge transfer will be more complicated.

satellites, while the 2p XAS spectrum in principle only shows a single peak (with its multiplet splittings). This difference between 2p XPS and 2p XAS can be summarized as follows:

> XPS is sensitive to the charge transfer effects or in other words the *electronic configuration* of the ground state, while XAS is sensitive to the *symmetry* of the ground state with its characteristic multiplet.

4.4. Interplay between charge transfer and multiplet effects

We assume that in a final state of 2p XAS the multiplet lines are spread out over an energy range of several electronvolts (for details of multiplet calculations see Section 5.1). This spread implies that the energy difference of these different states with the $2p^53d^{N+2}\underline{L}$ band varies considerably. In Fig. 13 a situation is sketched in which the multiplet splittings ($\delta/2$) are less than the charge transfer energy (Δ). If hybridization is turned on, the energy-gain of the lowest multiplet state (Γ_1) will be less than the energy-gain of the highest multiplet state, because the effective energy difference with the band is much smaller in the latter case. In the case of a multiplet with 100 lines instead of 2 this principle remains valid. The consequence is that the multiplet structure is "compressed" with respect to the atomic multiplet. If the spread of multiplet states is larger than the charge transfer energy, some of the multiplet states will be located within and above the band and the effects of charge transfer will be more complex. To account for these situations the short range model has been extended to include multiplet effects by Jo and Kotani [Jo88a]. This will be discussed in Section 5.3.

5. Metal 2p X-ray absorption

Charge transfer effects are less effective in 2p X-ray absorption and in the first part of this section they will be neglected altogether. What remains is a description of localized 3d states, which can be treated in detail using a multiplet approach. In Section 5.3 the short range model will be extended to include these multiplet effects.

5.1. The ligand field multiplet model

The ligand field multiplet (LFM) model has been proven to be successful in the description of metal 2p X-ray absorption spectra. It was first applied to core spectra by the groups in Tokyo [Asa75, Asa76, Yam77, Sug82, Shi82, Yam82a, Yam82b] and

Winnipeg [Gup74, Gup75]. For an account of the historical development of the model the reader is referred to [Deg91t] and a general history of X-ray absorption can be found in [Stu89].

5.1.1. Atomic multiplet theory

Atomic multiplet theory describes the correlated electronic states in partly filled atomic shells. It is the general theory in use for the calculation of core excitation spectra of atoms and as such is described in many textbooks such as those of Condon and Shortley [Con35] and Cowan [Cow81].

The Hamiltonian for atomic multiplets is

$$\mathscr{H} = \mathscr{H}_{3d} + \mathscr{H}_{mu} + \mathscr{H}_{ls} \tag{13}$$

The notation is as used for the short range model (Sections 4 and 5.3). $\mathscr{H}_{3d}$ gives just the average energy of the 3d states, $\mathscr{H}_{mu}$ includes all two-electron integrals which will be described below, and $\mathscr{H}_{ls}$ denotes the 3d spin–orbit coupling. In the final state the core state energy $\mathscr{H}_{c}$, its two-electron integrals with the 3d states $\mathscr{H}_{c.mu}$, and its spin–orbit splitting $\mathscr{H}_{c.ls}$ must be added. This will be discussed below.

As an introduction some of the simplest atomic multiplets will be discussed. A transition metal atom or ion with a partly filled 3d orbital contains electrons which have ten possible combinations of angular and spin momenta m_l and m_s. Because the spin–orbit coupling is small for 3d electrons, *LS*-coupling gives a good description [Kar70]. For a $3d^1$ configuration the overall quantum numbers L and S are respectively 2 and $\frac{1}{2}$, hence J is either $\frac{3}{2}$ or $\frac{5}{2}$. In general the atomic symmetries are notated with term symbols $^{2S+1}L_J$, which for a single 3d electron are $^2D_{5/2}$ and $^2D_{3/2}$. A $3d^2$ configuration has 45 combinations of L and S. They are grouped in the irreducible representations $^1G_4$, $^3F_4$, $^3F_3$, $^3F_2$, $^1D_2$, $^3P_2$, $^3P_1$, $^3P_0$ and $^1S_0$. Similarly a $3d^3$ configuration has 120 configurations divided over ^4F, ^4P, ^2H, ^2G, ^2F, ^2D (2 times) and ^2P. To determine the wavefunctions of these three-electron states, a general method has been developed in which first two electrons are coupled to $|d^2\mathbf{LS}\rangle$ and subsequently this two-electron function is coupled with the third electron. From symmetry arguments and recoupling formulae it can be shown that the overall wavefunction $|d^3\mathbf{L'S'}\rangle$ can be formed by a summation over all *LS* combinations of the two-electron wavefunctions multiplied by a specific coefficient [Cow81]

$$|d^3\mathbf{L'S'}\rangle = \sum_{\mathbf{L,S}} |d^2\mathbf{LS}\rangle c_{\mathbf{LS}} \tag{14}$$

For example the ^4F state of $3d^3$ is built from its parent triplet states as

$$|d^3[^4F]\rangle = \tfrac{4}{5}|d^2[^3F]\rangle - \tfrac{1}{5}|d^2[^3P]\rangle \tag{15}$$

Similarly all other $3d^3$ states can be generated. The values with which to multiply the parent states are called coefficients of fractional parentage. The coefficients of fractional parentage are tabulated for all partly filled d and f states by Nielsen and Koster [Nie63].

5.1.1.1. Slater integrals, Racah parameters and Hund's rules. The origin of the energy differences for the different symmetries (term symbols) can be found in the two-electron integrals and the spin–orbit coupling. The usual method of determining the two-electron integrals is by expanding them as a series of Legendre polynomials [Con35, Cow81]. The radial part reduces to the integral

$$R^k(d_1d_2, d_3d_4) = \int_{r_1}\int_{r_2} \frac{r_<^k}{r_>^{k+1}} \times P_1(d_1)P_2(d_2)P_1(d_3)P_2(d_4)dr_1dr_2 \tag{16}$$

It is common practice to divide the radial integrals into Coulomb terms and exchange terms. The Coulomb terms are denoted as $R^k(d_1d_2, d_1d_2) \Rightarrow F^k(d_1, d_2)$ and the exchange terms as $R^k(d_1d_2, d_2d_1) \Rightarrow G^k(d_1, d_2)$, the so-called Slater integrals. The angular part puts strong selection rules on the k values in the series expansion, i.e. for two 3d-electrons only F^0, F^2 and F^4 are possible and for a pd interaction F^0, F^2, G^1 and G^3. There is a close relationship between F^2 and F^4 and to about 1% accuracy F^4 equals $0.63F^2$.

Table 3
Relative energy positions of a $3d^2$ configuration; for the values in the third column the representative values $B = 0.1$ eV and $C = 0.4$ eV are used

Symmetry	Relative energy/eV	
$E(^1S)$	$+14B+7C$	+4.2
$E(^1D)$	$-3B+2C$	+0.5
$E(^1G)$	$+4B+2C$	+1.2
$E(^3P)$	$+7B$	+0.7
$E(^3F)$	$-7B$	−0.8

A number of alternative closely connected notations are in use. In the subscript F_k notation the F^k Slater integrals are renormalized with a common k-dependent denominator D_k [Con35]. Often the Racah parameters A, B and C are used and Table 2 gives their relation to the Slater integrals. The table also contains the relationship of the Slater integrals to the notation which uses the "Hubbard" U and the "Stoner" exchange J values [Mar88a]. In the bottom half of the table the constant relation between F^2 and F^4 is used.

The effects of the two-electron integrals on the different symmetries of a $3d^2$ configuration are shown in Table 3. The ground state is the ^3F state, which is an example of the rule that for a general $3d^N$ configuration the ground state is that state with highest S, and for these states the state with the highest L, Hund's rule [Hun27] applies. Hund's rule is a direct consequence of the two-electron integrals: S (and L) are maximized because the electron–electron repulsion is minimized if the electrons belong to different m_l-orbitals and also because electrons with parallel spin have an additional exchange interaction which lowers their total energy. Hund's third rule states that if the ^3F state is split because of inclusion of the 3d spin–orbit coupling the ground state is the state with the lowest J, the $^3F_2$ state. In case more than five 3d electrons are present, the highest J value has lowest energy. Notice that the Hund's rules do not explain the ordering of the states (for example ^1D has lower energy than ^1G), but only the symmetry of the ground state.

5.1.1.2. The atomic multiplets of the final state. In the final state of the metal 2p X-ray absorption process a $2p^53d^{N+1}$ configuration is formed. The dominating interaction is the core hole spin–orbit coupling, which modifies the couping scheme to jj-coupling for the 2p core state and LS-coupling for the 3d valence state. The overall coupling scheme is a mixture of jj- and LS-coupling. As an example the transition from an empty 3d system ($3d^0$) will be discussed. Its final state has a $2p^53d^1$ configuration. Its symmetries are determined by multiplication of a d state with a p state

$$^2P \otimes {}^2D = {}^1P_1 + {}^1D_2 + {}^1F_3 + {}^3P_{0,1,2} + {}^3D_{1,2,3} + {}^3F_{2,3,4} \quad (17)$$

Because of the dominant 2p spin–orbit coupling (ζ_{2p}) the final state is described in an intermediate coupling scheme, which implies that the different symmetries $^3P_{0,1,2}$, etc., will be at quite different energies. If only the 2p spin–orbit coupling, ranging from about 3 eV for scandium to about 10 eV for nickel, is considered the 2p spectra are split into two structures, the L_3 and the L_2 edge, separated by $\frac{3}{2}\zeta_{2p}$. The pd Coulomb and exchange terms F^2_{pd}, G^1_{pd} and G^3_{pd} are of the order of 5 to 10 eV and from Table 3 it can be seen that the dd interactions cause splittings of the order of 5 eV. The combination of the 2p spin–orbit interaction and the dd and pd two-electron integrals results in a complex distribution of states for a general $2p^53d^N$ configuration.

5.1.1.3. The calculation of the atomic states. In the calculations presented in this review the atomic Hamiltonian is solved by a Hartree–Fock (HF) method, which is corrected for correlation effects [Cow81]. This method has been developed for atomic spectroscopy and detailed comparison with experiments has revealed that the quantitative agreement is not good. The calculations assume the ground state to be represented by a single $3d^N$ configuration. This introduces errors because the ground state is not single configurational but contains an admixture of a series of

configurations. The obvious extension of the calculational scheme is to include excited configurations in a configuration interaction calculation. The situation is, however, not favourable for calculations because there exist an infinite number of small effects.

Theoretical studies indicate that it is possible to approximate the infinite series of excited configurations with a single configuration which has an equivalent dependence on spin- and angular-momenta as the ground state but with an opposite sign [Raj63, Raj64, Wyb65]. This gives a partial justification of the reduction of the HF-values of the Slater integrals to 80% of their original values [Cow81]. It has been found that the disagreement with experiment is largely solved by this semi-empirical correction to the Slater integrals. A recent effort to overcome these problems and to actually perform a multi-configurational calculation has been made by Sarpal and co-workers [Sar91]. Using a multi-configurational Dirac–Fock calculation scheme, the $M_{4,5}$ edges of divalent samarium and thulium atoms were calculated. From comparison with experiment it appears that for the multi-configurational spectrum the agreement is not good, and the renormalized HF results from Thole and coworkers [Tho85c] compare far better with the experimental spectrum.

5.1.1.4. The transition probability. The calculation of the transition probability is the last step to the atomic multiplet spectrum of a 2p X-ray absorption process. As discussed in Section 4.1.1 the transition strength is given as the 3J-symbol times a reduced matrix element

$$\langle 3d^0(JM)|\mathbf{r}_q|2p^5 3d^1(J'M')\rangle =$$

$$\begin{pmatrix} J & 1 & J' \\ -M & q & M' \end{pmatrix} \langle 3d^0(J)\|\mathbf{r}_q\|2p^5 3d^1(J')\rangle$$

For the initial state $J = 0$, hence with the dipole selection rules ($\Delta J = \pm 1$, 0 and $J + J' \geqslant 1$) the J-value of the final state must be unity. As shown above, the $2p^5 3d^1$ final state contains three states

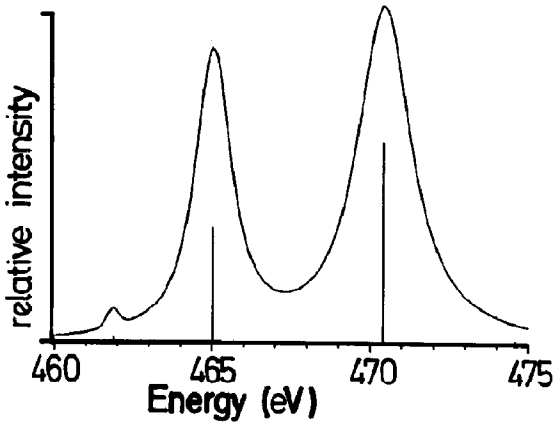

Fig. 14. Atomic multiplet calculation for the $3d^0 \rightarrow 2p^5 3d^1$ transition in tetravalent titanium.

with $J = 1$, $^1P_1$ (L_2 edge) and $^3P_1$ and $^3D_1$ (L_3 edge). Figure 14 shows the $3d^0 \rightarrow 2p^5 3d^1$ transition as calculated for a Ti^{4+} ion. Apart from the L_3 and L_2 peaks split by the 2p spin–orbit coupling, a third low-intensity peak is predicted at lower energy. This three-peaked spectrum is indeed observed, for example for calcium physisorbed on a silicon (111) surface [Him91].

5.1.2. From atoms to solids

If one transfers this atomic method to the solid state, the first question to ask is, is it possible at all to describe a 3d state in a solid quasi-atomic state? The discussion of the short range model in Section 4 has revealed that because of the counteracting effects of U_{dd} and $U_{\underline{c}d}$ this is indeed the case for X-ray absorption. However there remains the problem of how to accommodate the atomic states in the solid state environment. Particular questions are, (1) how to deal with the different local symmetry, and (2) how to incorporate the different more itinerant electronic features of the solid state, such as the electron density of the s and p states. The inclusion of the local symmetry has been the subject of many studies under the heading of ligand field theory [Grf64]. This has been used particularly to describe the optical absorption spectra of transition metal ions. For core spectroscopies, ligand field theory was developed in the seventies [Asa75, Gup74, Gup75, Yam77]. In this

Table 4
Effect of a cubic ligand field on a 3d electron

Representation	Orbital name	Atomic states	Cartesian notation
E_g	d_{z^2}	$\|20\rangle$	$\frac{1}{2}(3z^2 - r^2)$
	$d_{x^2-y^2}$	$\frac{1}{\sqrt{2}}\|2\bar{2}\rangle + \frac{1}{\sqrt{2}}\|22\rangle$	$\frac{\sqrt{3}}{2}(x^2 - y^2)$
T_{2g}	d_{xy}	$\frac{1}{\sqrt{2}}\|2\bar{2}\rangle - \frac{1}{\sqrt{2}}\|22\rangle$	$\sqrt{3}(xy)$
	d_{yz}	$\frac{1}{\sqrt{2}}\|2\bar{1}\rangle + \frac{1}{\sqrt{2}}\|21\rangle$	$\sqrt{3}(yz)$
	d_{zx}	$\frac{1}{\sqrt{2}}\|2\bar{1}\rangle - \frac{1}{\sqrt{2}}\|21\rangle$	$\sqrt{3}(zx)$

review the more general approach as developed by Thole and co-workers will be discussed in detail [Tho88a].

The itinerant effects of the solid have been described under the heading nephelauxatic effect [Jor62, Jor71] with the analogy to expanding clouds, and hence smaller on-site overlap. In Section 5.3 the effects of itinerant states on multiplets will be described using the short range model approaches. In the next section the emphasis will be on the symmetry effects.

5.1.3. Symmetry effects in solids

The dominant symmetry effect in solids is the cubic ligand field. The strength of this operator is usually denoted as the ligand field splitting (10Dq). Atomic multiplet theory can be extended to describe the 3d metal ions by incorporating the ligand field splitting.

In an octahedral environment the field of the neighbouring atoms of the central atom has cubic (O_h) symmetry which divides the fivefold degenerate 3d orbitals into two distinct representations of T_{2g} and E_g symmetry. The twofold degenerate E_g state contains orbitals which point towards the centre of the cube faces, that is directly towards the position of the ligands. Consequently E_g states interact more strongly, electrostatically as well as covalently, with the ligands. The three t_{2g} orbitals point towards the corners of the cube and therefore their interaction with the octahedral ligands is smaller. Table 4 describes the five ligand field states in terms of their atomic constituting functions.

In the ligand field multiplet model the atomic symmetries are projected to cubic symmetry. Table 5 reproduces the branching rules for projection from atomic to cubic symmetry [But81].

Table 5
The $SO_3 \rightarrow O_h$ branching rules in the Schönflies notation

Spherical	Cubic
S	A_1
P	T_1
D	$E + T_2$
F	$A_2 + T_1 + T_2$
G	$A_1 + T_1 + T_2 + E$
H	$T_1 + T_1 + T_2 + E$
I	$A_1 + A_2 + T_1 + T_1 + T_2 + E$

5.1.3.1. Effects on the energy positions. The effects of the cubic ligand field on the energies of the atomic states have been described in the textbooks of Ballhausen [Bal62], Griffith [Grf64] and Sugano et al. [Sug70]. From Table 5 it can be checked that the degeneracy of the atomic states is partially lifted and the D, F, and higher states are split into a series of representations in cubic symmetry. The diagrams representing the effect of a cubic ligand field are denoted as Tanabe–Sugano diagrams. Figure 15, reproduced from [Sug70], sketches the energy positions as functions of the magnitude of the cubic ligand field (10Dq), relative to the Racah parameter B.

In the $2p^5 3d^N$ final state the effects of the cubic ligand field are equivalent to that in the initial state.

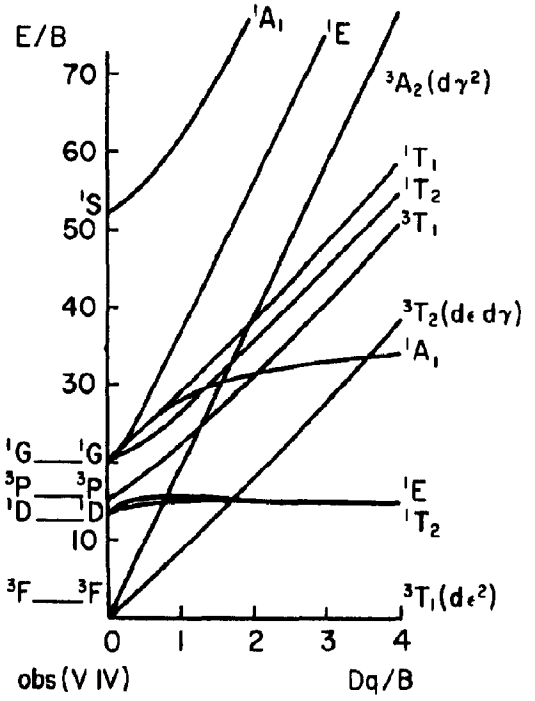

Fig. 15. Tanabe–Sugano diagram for a $3d^2$ ground state in cubic symmetry (from [Sug70]).

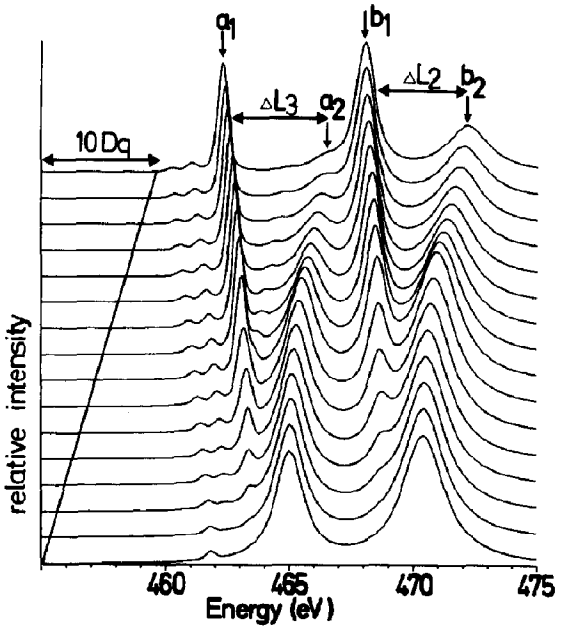

Fig. 16. Ti^{4+} X-ray absorption spectrum, calculated for an increasing cubic crystal field. The value of 10Dq is increased from 0.0 to 4.5 eV.

A difference is that the number of multiplet states is considerably larger: for a $3d^N$ initial state the maximum number of states is 256, while it is 6 times larger (=1536) for a $2p^53d^5$ final state. The number of irreducible representations is smaller because of degeneracies.

5.1.3.2. Effects on the transition probabilities. The transition probability for the $3d^0$ systems in cubic symmetry is

$$\langle 3d^0[^1A_1]||\mathbf{r}_q[T_1]||2p^53d^1[A_1 \otimes T_1 = T_1]\rangle \qquad (18)$$

All final states of T_1 symmetry are allowed and have a finite transition probability from the $^1A_1$ initial state. From Table 5 it can be seen that this includes the states of $J = 1$ atomic symmetry, but additionally the states with $J = 3$ and $J = 4$. The degeneracy of these states is respectively 3 and 1, as can be deduced from the $2p^53d^1$ states in *jj* coupling [Deg90a]. The total number of allowed final states in cubic symmetry is $3 + 3 + 1 = 7$. Figure 16 shows the effects of an increasing cubic ligand field on the multiplet spectrum of the $3d^0 \rightarrow 2p^53d^1$ transition. In this figure it can be seen that for small values of the ligand field (the step size is 0.3 eV) the spectrum is hardly modified. For small values of 10Dq the four states which were forbidden in atomic symmetry have not gained enough intensity to be detectable in the spectrum.

Figure 17 shows the energy splittings between the peaks a_1 and a_2. This splitting is compared with the size of the cubic ligand field splitting and it can be seen that the peak splitting in the spectrum is not directly related to the value of 10Dq. From this figure it becomes clear why, for small values of 10Dq, no detectable amount of intensity is transferred. The energy difference between the two states a_1 and a_2 is about 2 eV in the atomic case when a_2 is allowed and a_1 forbidden. A ligand field splitting of 0.3 or 0.6 eV will hardly affect states which are separated by 2 eV, as is evidenced by the slow increase of the splittings around $10Dq = 0$.

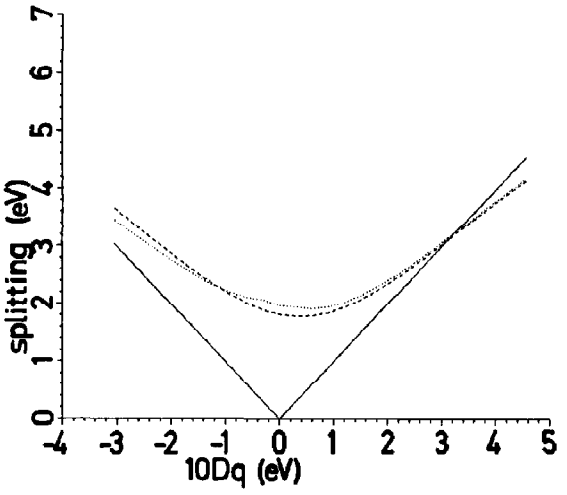

Fig. 17. The dashed line indicates the splitting between the peaks a_1 and a_2 of Fig. 16. The dotted line is for peaks b_1 and b_2.

5.1.3.3. Comparison with experiment. The ligand field multiplet results as calculated with the procedure outlined above can be compared directly with experiment. Figures 18–20 compare the ligand field multiplet calculation of Ca^{2+}, Sc^{3+} and Ti^{4+} ions with the respective 2p X-ray absorption spectra. Atomic Slater integrals were used. For

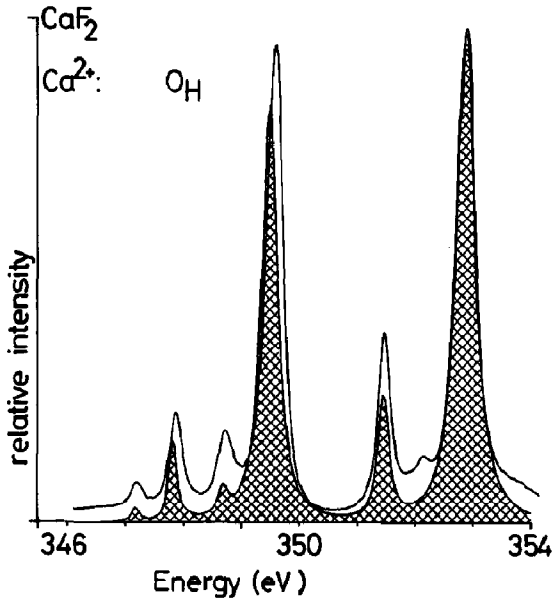

Fig. 18. Calcium 2p X-ray absorption spectrum of CaF_2 (solid line) compared with a ligand field multiplet calculation (hatched area). The value of 10Dq is −0.9 eV.

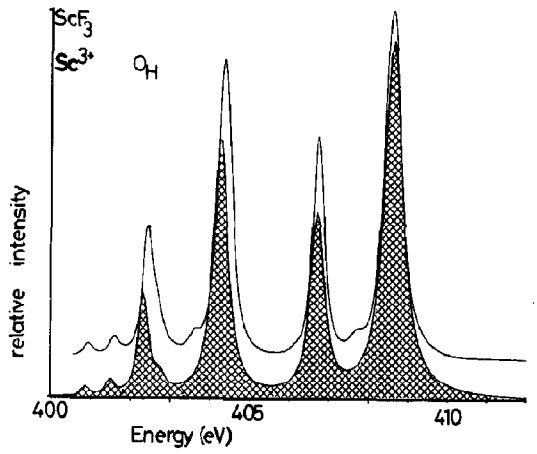

Fig. 19. Scandium 2p X-ray absorption spectrum of ScF_3 (solid line) compared with a ligand field multiplet calculation (hatched area). The value of 10Dq is 1.7 eV.

details concerning the broadenings the reader is referred to [Deg90a]. All peaks in the experimental spectrum are reproduced, which is a confirmation that the ligand field multiplets indeed dominate the spectral shape. Note that even the $SrTiO_3$ spectrum is reproduced rather well with atomic values of the Slater integrals. This raises the question how it is possible that titanium can be described as tetravalent, while for example band structure results show that the charge transfer from titanium to oxygen is small and certainly not four electrons [Deg93a]. Part of the answer is that what matters is the symmetry of the ground state and because the 3d band is empty this is $^1A_1$ for titanium in $SrTiO_3$.

5.1.3.4. Multiplets of partly filled states. Table 6 gives the (Hund's rule) ground state symmetries of the atomic multiplets and their projection to cubic symmetry. If four electrons have to be accommodated in the 3d orbitals in an octahedral surrounding, two effects are important, the exchange coupling of an e_g electron with a t_{2g} electron (J_{te}) and the cubic ligand field splitting D. (The exchange coupling is connected to the Slater integrals as given in Table 2.) If $3J_{te} > D$, a high-spin $(t_{2g}^+)^3(e_g^+)^1$ configuration with ^5E symmetry is formed from the Hund's rule ^{5}D ground state. However if $3J_{te} < D$, a low-spin $(t_{2g}^+)^3(t_{2g}^-)^1$ configuration with $^3T_1$ symmetry is formed.

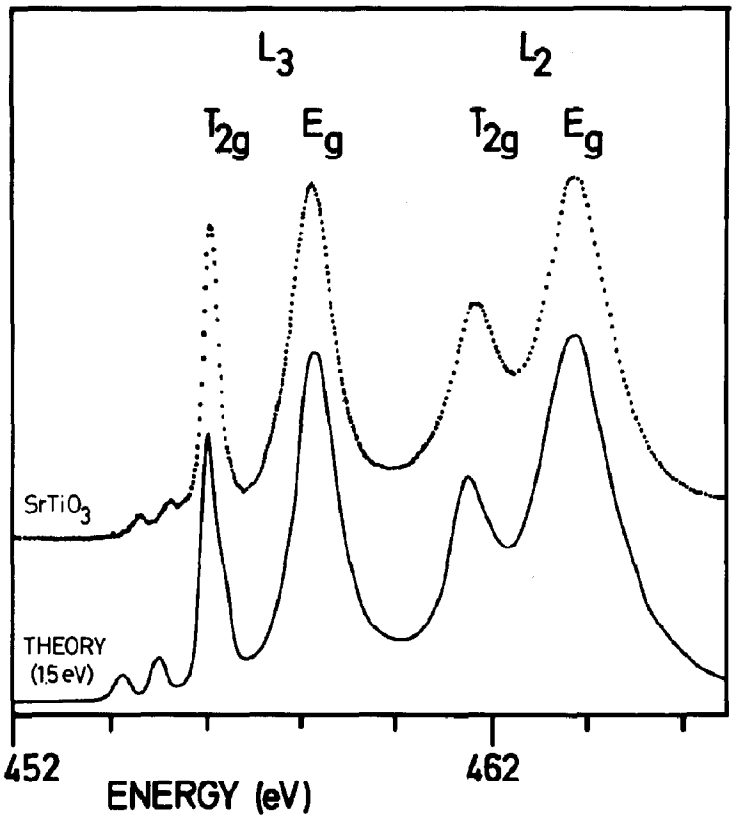

Fig. 20. Titanium 2p X-ray absorption spectrum of $SrTiO_3$ compared with a ligand field multiplet calculation. The value of 10Dq is 1.5 eV.

The criteria for high-spin or low-spin ground state are collected in Table 7. The exchange splittings J are different for different combinations of e_g or t_{2g} electrons, though these differences are small. Approximately $J_{ee} - 0.1 = J_{te} = J_{tt} + 0.1$ eV [Bal62]. The exchange splitting J_{te} is about 0.8 eV for 3d electrons. From this value one can estimate the point where the ligand field is large enough to change from high-spin to low-spin. The estimates are given in the last column of Table 2.

5.1.3.5. Ligand field multiplet calculations for $3d^N$. The calculation of the ligand field multiplet is in principle equivalent to that of the $3d^0$ configuration, with the additional possibility of low-spin ground states. As an example the $3d^5[A_1] \rightarrow 2p^5 3d^6[T_1]$ ligand field multiplet is given in Fig. 21.

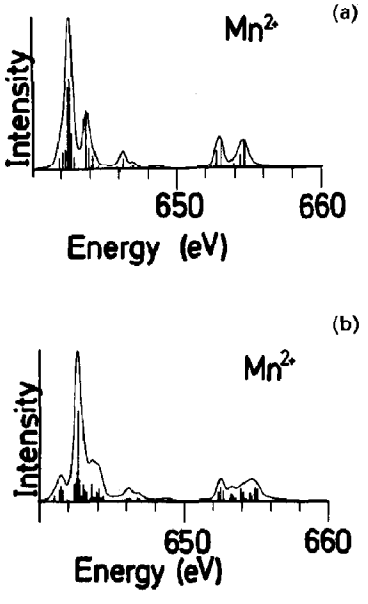

Fig. 21. Mn^{2+} $3d^5$ to $2p^5 3d^6$ transition for (a) 10Dq = 0.0 and (b) 0.9 eV. The line spectrum and the broadened spectrum are given.

Table 6
Symmetries and configurations of all possible $3d^N$ states[a]

State	Atomic symmetry	Cubic symmetry	Configuration	Susceptible for
$3d^1$	^2D	$^2T_2$	$(t_{2g}^+)^1$	3d spin–orbit
$3d^2$	^3F	$^3T_1$	$(t_{2g}^+)^2$	3d spin–orbit
$3d^3$	^4F	$^4A_2$	$(t_{2g}^+)^3$	–
$3d^4_{HS}$	^5D	^5E	$(t_{2g}^+)^3(e_g^+)^1$	Jahn–Teller
$3d^4_{LS}$		$^3T_1$	$(t_{2g}^+)^3(t_{2g}^-)^1$	3d spin–orbit
$3d^5_{HS}$	^6S	$^6A_1$	$(t_{2g}^+)^3(e_g^+)^2$	–
$3d^5_{LS}$		$^2T_2$	$(t_{2g}^+)^3(t_{2g}^-)^2$	3d spin–orbit
$3d^6_{HS}$	^5D	$^5T_2$	$(t_{2g}^+)^3(e_g^+)^2(t_{2g}^-)^1$	3d spin–orbit
$3d^6_{LS}$		$^1A_1$	$(t_{2g}^+)^3(t_{2g}^-)^3$	–
$3d^7_{HS}$	^4F	$^4T_1$	$(t_{2g}^+)^3(e_g^+)^2(t_{2g}^-)^2$	3d spin–orbit
$3d^7_{LS}$		^2E	$(t_{2g}^+)^3(t_{2g}^-)^3(e_g^+)^1$	Jahn–Teller
$3d^8$	^3F	$^3A_2$	$(t_{2g}^+)^3(e_g^+)^2(t_{2g}^-)^3$	–
$3d^9$	^2D	^2E	$(t_{2g}^+)^3(e_g^+)^2(t_{2g}^-)^3(e_g^-)^1$	Jahn–Teller

[a] If the ligand field exceeds the exchange splitting a low-spin state is formed. A T-symmetry ground state is susceptible to 3d spin–orbit coupling and an E-symmetry state is affected by a Jahn–Teller splitting (see next section).

To obtain the 2p X-ray absorption spectra the calculated line spectrum is broadened with a Lorentzian broadening to simulate life-time effects and a Gaussian broadening to simulate the resolution function of the experiment. Figure 22, reproduced from [Deg91t], shows the comparison for MnO. Good agreement is obtained with the atomic values of the Slater integrals and a ligand field splitting of 0.8 eV.

The transition from a high-spin to a low-spin ground state is directly visible in the spectral shape, because a different final state multiplet is reached. This is illustrated for Co^{3+} in Fig. 23. A series of calculations for all common ions has been published in [Deg90b]. In these calculations the 3d spin–orbit coupling has been set to zero. A series of calculations in which the 3d spin–orbit coupling has been included has been published in [Laa92c]. The criterion whether or not 3d spin–orbit coupling is important will be discussed in the next section.

Table 7
Interactions determining the high-spin or low-spin ground state of $3d^4$ to $3d^7$ configurations in octahedral symmetry

State	Criterion	Simplified criterion	Transition point/eV
$3d^4$	$3J_{te}$	$3J$	2.4
$3d^5$	$3J_{te}+\frac{1}{2}J_{ee}-\frac{1}{2}J_{tt}$	$3J$	2.5
$3d^6$	$3J_{te}+\frac{1}{2}J_{ee}-\frac{3}{2}J_{tt}$	$2J$	1.8
$3d^7$	$3J_{te}+J_{ee}-2J_{tt}$	$2J$	1.9

5.1.4. 3d Spin–orbit coupling

In this section the treatment of the 3d spin–orbit coupling in the ligand field multiplet program is

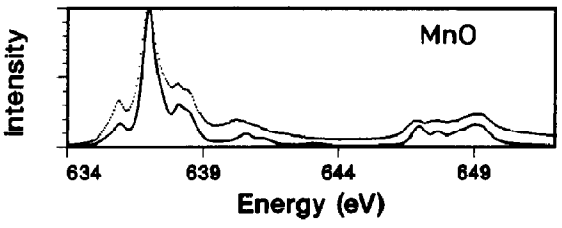

Fig. 22. Manganese 2p X-ray absorption spectrum of MnO (dotted) compared with a ligand field multiplet calculation (solid line). The value of 10Dq is 0.8 eV.

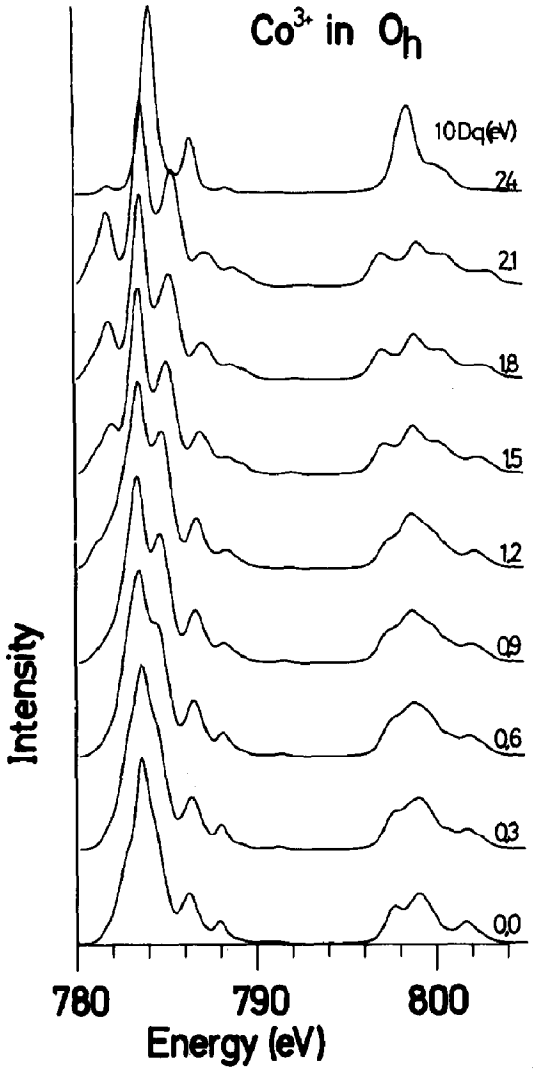

Fig. 23. Co^{3+} $3d^7$ to $2p^5 3d^8$ transition. 10Dq is increased from 0.0 to 2.4 eV. A high-spin to low-spin transition occurs between 2.1 and 2.4 eV.

discussed and arguments are given concerning the effects of the spin–orbit coupling.

For the projection of the spin symmetries from spherical to cubic symmetry the same branching rules as for the angular momentum apply. Compounds with an even number of 3d electrons have an integer spin and the branching rules as given in Table 5 can be used. For compounds with an odd number of 3d electrons the spin will be 1/2, 3/2 or 5/2. The atomic S = 1/2 state projects to E_1 symmetry in a cubic ligand field. The notation as used by Sugano, Tanabe and Kitamura is followed [Sug70]. Similarly S = 3/2 projects to G symmetry and S = 5/2 is split into states of E_2 symmetry and of G symmetry

If the 3d spin–orbit coupling is taken into consideration, the overall symmetry of the spin plus the angular momentum must be determined. In spherical symmetry this is accomplished by multiplying L with S to all possible J values. Similarly in cubic symmetry the irreducible representations of the spin must be multiplied with those of the angular momentum. Table 8 gives the results for the low-spin and high-spin configurations of all $3d^N$ states. It can be seen that in cubic symmetry the multiplicity of the spin $(2S+1)$ does not directly relate to the total number of states. For example the $^5T_2$ state is split into six (and not in five) different states. The ligand field multiplet program uses in all cases the branchings for both spin and angular momentum and thus the overall symmetries of the states. If the 3d spin–orbit coupling is neglected all states with the same angular symmetry are degenerate because the spin in itself does not influence the energy of the state.

3d Spin–orbit coupling does not affect states of A_1 or A_2 symmetry, but it has a large effect on partly filled t_{2g} states, that is the ground states of the $3d^1$, $3d^2$, $3d^4_{LS}$, $3d^5_{LS}$, $3d^6_{HS}$ and $3d^7_{HS}$ symmetries, as indicated in Table 6. The effects on states of E symmetry are small. The difference in effect on T_2 states and E states respectively is related to the way in which a t_{2g} and an e_g wavefunction respectively are built from the atomic wavefunctions. As has been shown in Table 4 an e_g wavefunction is generated from $m_l = 0$ and 2 (or −2) functions. A spin–orbit coupling effect can only affect states which differ by unity in their m_l value. This means that the 3d spin–orbit coupling (ζ_{3d}) is quenched in the case of e_g states. In the case of t_{2g} states this quenching does not occur and if only the t_{2g} states are taken into account they can be approximated with an effective $L = 1$, hence a $^2T_2$ state is split in two, with the eigenvalues $-\frac{1}{2}\zeta$ and ζ and intensity ratio 1:2, analogous to the

Table 8
Effects of spin–orbit coupling on $3d^N$ ground state

State	Symmetry	Spin projection	Overall symmetry	Degeneracy
$3d^1$	$^2T_2$	E_1	E_2+G	2
$3d^2$	$^3T_1$	T_1	$E+T_1+T_2+A_1$	4
$3d^3$	$^4A_2$	G	G	1
$3d^4_{HS}$	^5E	$E+T_2$	$A_1+A_2+E+T_1+T_2$	5
$3d^4_{LS}$	$^3T_1$	T_1	$E+T_1+T_2+A_1$	4
$3d^5_{HS}$	$^6A_1$	$G+E_2$	$G+E_2$	(2)
$3d^5_{LS}$	$^2T_2$	E_1	E_2+G	2
$3d^6_{HS}$	$^5T_2$	$E+T_2$	$A_1+E+2T_1+2T_2$	6
$3d^6_{LS}$	$^1A_1$	A_1	A_1	1
$3d^7_{HS}$	$^4T_1$	G	E_1+E_2+2G	4
$3d^7_{LS}$	^2E	E_1	G	1
$3d^8$	$^3A_2$	T_1	T_2	1
$3d^9$	^2E	E_1	G	1

$2p_{3/2}$ and $2p_{1/2}$ splitting for 2p spin–orbit coupling [Sug70].

To describe the full action of 3d spin–orbit coupling the non-diagonal matrix elements, coupling t_{2g} and e_g states have to be included. It can be shown that this affects the e_g states by $(3/2)(\zeta^2/\mathscr{D})$, as compared to the t_{2g} states which were affected by $(3/2)\zeta$. For a typical 3d transition metal compound $\zeta_{3d} \approx 70$ meV and the cubic ligand field splitting $\mathscr{D} \approx 1.0$ eV. This gives splittings of about 100 meV (≈ 1200 K) for T symmetry ground states and of about 8 meV (≈ 100 K) for E symmetry ground states. This implies that for room temperature experiments 3d spin–orbit coupling should be included for T symmetry ground states, but can be neglected for E symmetry ground states. Hence as a first approximation to the experimental spectra one can use the results of [Laa92c] for T symmetry ground states and the results of [Deg90b] for E symmetry ground states. For A symmetry ground states the results are identical. In practice it will in most cases be necessary to make more precise comparisons as for example for T symmetry ground states there will be configurations at energies of about 300 K, which implies that a Boltzmann distribution over the states must be included. (E-symmetry ground states are susceptible to Jahn–Teller distortions, see next section.)

Because the spin–orbit coupling strength increases with the atomic number, the best case to investigate the effect of 3d spin–orbit coupling is the $3d^7_{HS}$ configuration, as is for example found in CoF_2 and CoO. From Table 8 it is found that if 3d spin–orbit coupling is included, the $^4T_1$ ground state of the $3d^7_{HS}$ configuration splits in four states of E_1, E_2 and two times G symmetry. The multiplet calculation with the atomic value of the 3d spin–orbit coupling (83 meV) and a cubic ligand field strength of 0.9 eV gives the four states at energies of respectively 0 (E_2), 44 meV (G), 115 meV (G^*) and 128 meV (E_1). Figure 24 gives the ligand field multiplets of the $3d^7_{HS}[\Gamma_i] \rightarrow 2p^5 3d^8$ transition for the four different symmetries. Given this spread in the initial states, the room temperature (25 meV) spectrum is dominated by the lowest state of E_2 symmetry, with a 17% contribution of the first excited state of G symmetry.

Figure 25 gives the theoretical spectra of the ground state E_2 spectrum (b), the 300 K spectrum (c) and the spectrum under neglect of 3d spin–orbit coupling (a). It is clear that the inclusion of the 3d spin–orbit coupling enhances the agreement

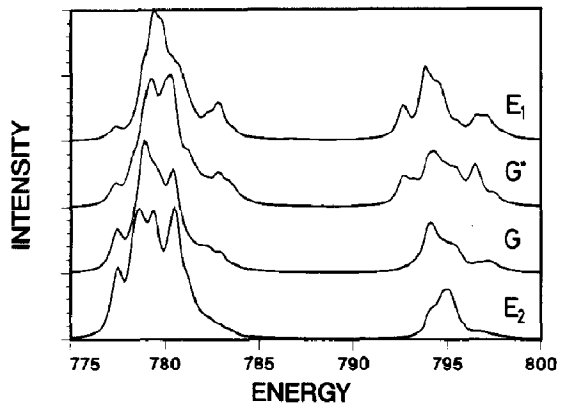

Fig. 24. Theoretical X-ray absorption spectra for the $3d^7_{HS}[\Gamma_i] \rightarrow 2p^5 3d^8$ transition for the four different 3d spin–orbit split symmetries of the $^4T_1$ ground state. The respective symmetries are from bottom to top: E_2, G, G^* and E_1.

considerably. The good agreement between theory and experiment makes it possible to determine the energies of the low-lying excited states from an analysis of the experimental spectrum, preferably measured for a series of temperatures. Hence it can be concluded that temperature dependent X-ray absorption experiments can reveal the magnitude of the 3d spin–orbit coupling, which might be different from the atomic value [Deg91t, Tan92a].

5.1.4.1. The effects of 3d spin–orbit coupling on the high-spin–low-spin transition. In the discussion of the high-spin versus low-spin states it has been assumed that the spin state of a system is that state with the lowest energy, implying that at the crossing point (in the Tanabe–Sugano diagram) the ground state is changed suddenly from high-spin to low-spin. However it turns out that if 3d spin–orbit coupling is included, this will couple high-spin states with low-spin states. This implies that the transition between high-spin and low-spin can be gradual with close to the transition point an admixture of both high-spin and low-spin symmetries. This situation will be discussed for $3d^4$. From Table 6 it can be seen that the high-spin state has ^5E symmetry and is susceptible to Jahn–Teller distortions, while the low-spin state has $^3T_1$ symmetry and is susceptible to 3d spin–orbit coupling. To simplify the problem the ligand field multiplet calculations are performed in octahedral symmetry

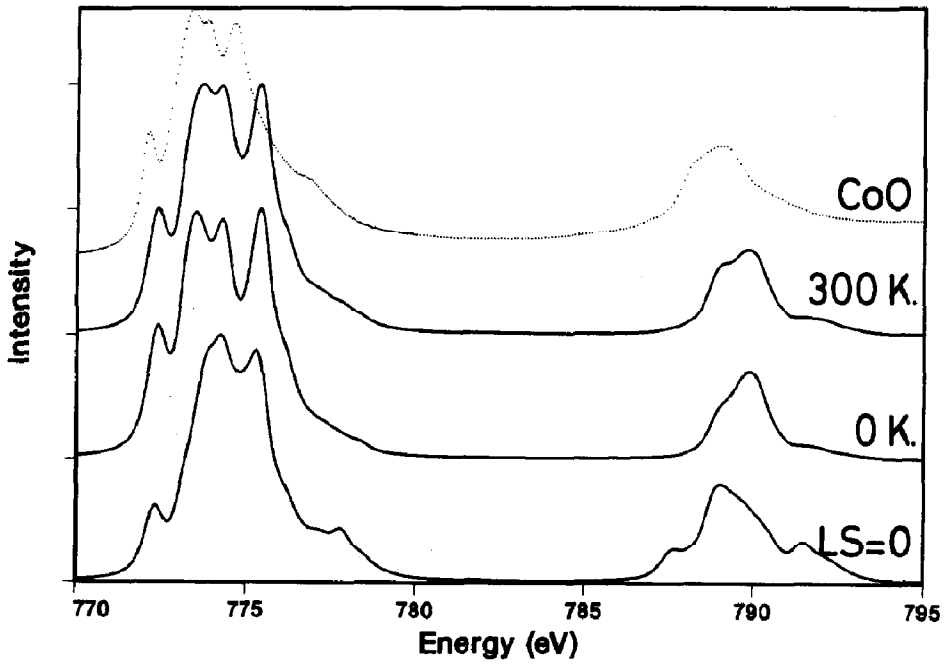

Fig. 25. Comparison of the theoretical spectra of (from bottom to top) (curve a) the spectrum under neglect of 3d spin–orbit coupling, (curve b) the ground state, and (curve c) the spectrum at 300 K, with the experimental spectrum of CoO.

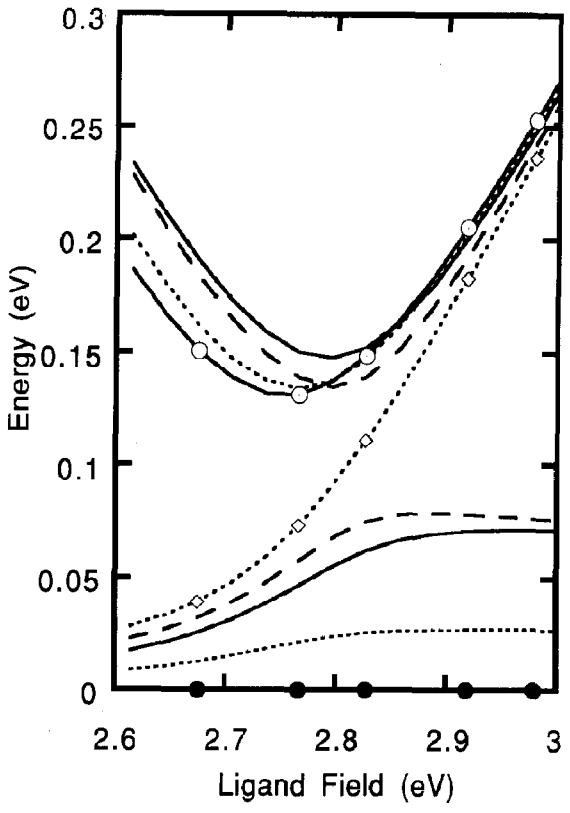

Fig. 26. Distribution of states in the $3d^4$ initial state showing the effects of 3d spin–orbit coupling at the high-spin to low-spin transition. On the left hand side the symmetries are from bottom to top: (high spin) A_1, T_1, E, T_2, A_2; (low spin) A_1, T_1, T_2, E.

and effects of the Jahn–Teller distortion have been neglected. The Slater integrals have been reduced to 75% for dd interactions and to 88% for pd interactions and the atomic 3d spin–orbit coupling has been used.

Figure 26 shows the energy levels for ligand field strength between 2.6 and 3.0 eV. The high-spin ^5E configuration splits after inclusion of the 3d spin–orbit coupling into five states of respectively A_1, A_2, T_1, T_2 and E symmetry. Likewise the $^3T_1$ configuration splits into four states of A_1, T_1, T_2 and E symmetry. For a ligand field of 2.6 eV ^5E symmetry is at lowest energy, while for 3.0 eV the system has a low-spin $^3T_1$ ground state. It can be observed directly that a T symmetry state is affected more by the 3d spin–orbit coupling as discussed above. At room temperature (0.025 eV) the high-spin ground state ($10Dq < 2.6$ eV) will be approximately given as a statistical distribution of the five states. If the cubic ligand field is increased to about 2.8 eV the lowest five states do still relate to the high-spin configuration, but the splittings between the states are enlarged due to considerable admixture of $^3T_1$ character. Note that the state of A_2 symmetry is only contained in the high-spin symmetry state and is not subject to admixture. Hence it can be used as an indication of the position of the high-spin configuration without interaction with the low-spin configuration.

Some $3d^4$ systems include $LaMnO_3$, and $LiMnO_2$, which are considered to be high-spin (^5E) insulators, [Bog57, Bog75, Goo63, Goo71], $SrFeO_3$, a low-spin or intermediate spin conductor [Gle85, Mcc65], and $CaFeO_3$, a high-spin compound probably subject to partial charge disproportionation below $T = 290$ K [Gle85]. Though $LiMnO_2$ probably has a high-spin ground state, it can be expected to be not too far from the transition point, in which case it can be affected by 3d spin–orbit coupling. Figure 27 gives the spectral shapes found from the ligand field multiplet calculations for, from bottom to top, the low-spin $^3T_1$ configuration, the high-spin ^5E configuration and the mixed spin state. The experimental spectrum of $LiMnO_2$ is shown with dots.

With regard to a further optimization of the spectral shape there are several factors to be considered. The Slater integrals have been set roughly to reduced values and the symmetry distortion related to the Jahn–Teller effect has been neglected. The Jahn–Teller distortion can have effects on the spectral shape in the range of about 1 eV and might account for the spectral mismatch. Also if the Jahn–Teller distortion is accounted for, the 3d spin–orbit coupling effects still have to be taken into account close to the high-spin to low-spin transition point (in reduced symmetry) [Deg91t].

5.1.5. Effects of non-cubic symmetries

Another type of low-energy splitting of the ligand field multiplet is caused by distortions from cubic symmetry. Large initial state effects of

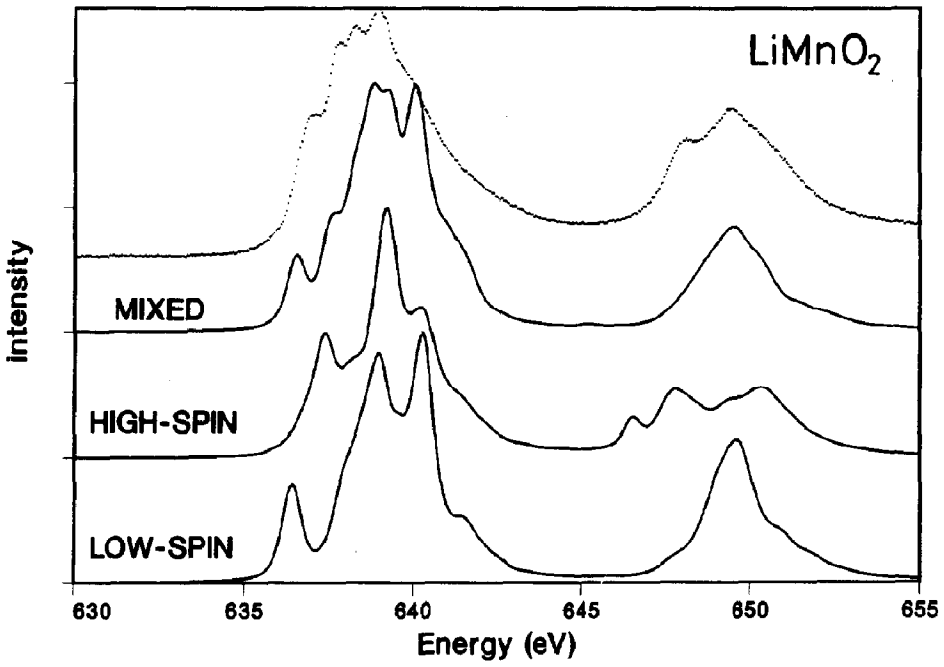

Fig. 27. Crystal field multiplet calculation for the 2d X-ray absorption spectrum of the low-spin, high-spin and mixed (or intermediate) spin ground state for trivalent ($3d^4$) manganese atoms. The top spectrum is the 2p X-ray absorption spectrum of $LiMnO_2$.

lower symmetries are found if the cubic $3d^N$ ground state contains a partly filled e_g band. Elongation of the z axis lifts the degeneracy of the e_g orbitals; the Jahn–Teller effect. Degenerate e_g states are found in systems with $3d^4_{HS}$, $3d^7_{LS}$ and $3d^9$. The effects on the $3d^4_{HS}$ state occur for divalent chromium and trivalent manganese. The tetragonal distortion of the $3d^9$ configuration is well known, for example in the CuO-based high T_c superconductors.

Final state effects of lower symmetries can be important for all $3d^N$ configurations if the site geometry is strongly distorted from cubic. Final state effects of lower symmetries are best observable for $3d^0$ compounds due to their simple spectral shape in which all multiplet transitions are resolved as individual peaks. In rutile (TiO_2) the site symmetry of titanium is D_{2h} and the effective configuration is $3d^0$. Effects of the symmetry reduction can be expected for the $2p^5e_g^1$-like states and indeed the rutile spectrum clearly shows a splitting of the e_g peak which is reproduced in a calculation for D_{4h} symmetry [Deg90a].

Similar final state effects of lower symmetries are expected for systems with a partly filled 3d band. However it can be expected that ligand field effects, including distortions from cubic symmetry, are more important for early 3d compounds. The important parameters are the radial extent of the wavefunctions of the 3d electrons r_ϕ and the inter-atomic distances R. It is known that the ratio r_ϕ/R decreases in the 3d metal series [Fug88, Mar85t], and especially in systems with one or more occupied e_g orbital, relatively large inter-atomic distances are found [Wis72]. Crystal field effects scale with r_ϕ/R; hence effects of lower symmetries (and also the cubic ligand field strengths) are largest for the early 3d metals.

5.1.5.1. Projection rules for lower symmetries. The ligand field multiplet program can handle any point group symmetry. As an example, the branching rules of a D_{2h} point group are given in Fig. 28. The projection from spherical symmetry to D_{2h} symmetry is accomplished in three steps. First the symmetry is reduced to cubic, in the second step

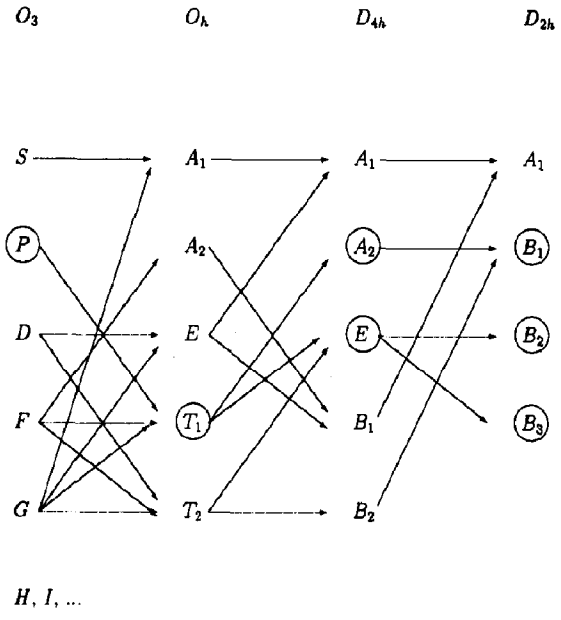

Fig. 28. Schematic branchings from O_3 symmetry (atomic) to D_{2h} symmetry, via O_h and D_{4h}. Encircled are all representations which can be reached from atomic P symmetry.

the cubic (O_h) to tetragonal (D_{4h}) symmetry reduction is included and the third step goes to D_{2h} symmetry. The necessary extra ligand field terms in the Hamiltonian can be deduced directly from this figure: the Hamiltonian has A_1 symmetry, thus all branchings to A_1 symmetry take part in the Hamiltonian. For cubic symmetry, apart from the S state, the G state projects to the A_1 state. This $G \rightarrow A_1$ branching describes the inclusion of a cubic ligand field term in the Hamiltonian. Similarly for tetragonal symmetry the cubic E state projects to the A_1 state. In turn the cubic E state has two parent states in spherical symmetry, hence there are two additional paths $D \rightarrow E \rightarrow A_1$ and $G \rightarrow E \rightarrow A_1$. In other words there are two additional ligand field parameters in the Hamiltonian of D_{4h} symmetry. The total number of ligand field parameters of a specific point group can be found directly from the total number of different paths leading to the A_1 symmetry state. It should be noticed that the "route" to reach the D_{2h} point group is not uniquely defined, and instead of the route via O_h (as given in Fig. 28) an alternative route via $D_{\infty h}$ can be chosen. The choice of the route determines the meaning of the ligand field parameters and because of the central place of the cubic ligand field strength, in general the route via O_h symmetry is used. The different branchings for all point groups and also all possible choices for the routes to reach a specific point group are given in [But81].

Systems with lower symmetries are expected to show large linear dichroism effects as will be discussed in Section 6.3. This can be deduced directly from Fig. 28 as the dipole operator is split in D_{4h} and lower symmetries.

5.2. *When are multiplets important?*

If multiplets are important an absorption edge is preferably described with an atomic approach as described above. In that case the short range models will be the most appropriate starting point because also the Hubbard U, directly related to the F^0_{dd} Slater integral, will be important. In contrast if multiplet effects are small, the band structure (or multiple scattering) approach is most appropriate because of its ab initio description of hybridization.

There is a simple rule for the importance of multiplets:

> Multiplets are important in the case of a direct transition to a partly filled d or f band.

Thus the p edges of transition metals and their compounds are affected by multiplet effects, whereas the s edges are not affected. For rare earths and actinides it means that their d edges are affected, in contrast to their s and, in first approximation, p edges. This rule can be deduced from the values of the atomic Slater integrals. Table 9 gives the values for the edges of iron, ruthenium and osmium. For comparison the values for the 3d edge of terbium are given. These values are expected to be only marginally screened in solid transition metals and their compounds. Depending on the obtainable resolution, mainly determined by the core hole life-time, the multiplet effects are observable. From Table 9 it is clear that

Table 9
Slater integrals as calculated with the HF for the d^5 transition metal ions Fe^{3+}, Ru^{3+} and Os^{3+}

Ion	Edge	Excitation energy/eV	Core hole spin–orbit/eV	F^2_{pd}/eV	G^1_{pd}/eV	G^3_{pd}/eV
Fe^{3+}(3d)	3p	[60]	(<1)	13.1	16.2	9.9
	2p	[700]	(13)	7.5	5.5	3.2
	1s	[7150]	–	–	0.3	–
Ru^{3+}(4d)	4p	[50]	(3)	9.6	12.1	7.4
	3p	[470]	(22)	4.6	1.0	1.0
	2p	[2900]	(130)	2.1	1.8	1.0
Os^{3+}(5d)	5p	[52]		11.4	18.1	11.6
	4p	[510]		9.8	2.4	2.4
	3p	[2860]	(345)	5.4	1.1	1.2
	2p	[11630]	(1514)	3.1	2.7	1.6
Tb^{3+}(4f)[a]	3d	[1258]	(13)	8.04 3.77 (F^4)	5.79	3.40 3.35 (G^5)

[a] For comparison the 3d4f values of Tb^{3+} are given.

the iron 2p and 3p edges in particular will be dominated by multiplet effects.

5.2.1. Core hole spin–orbit coupling and branching ratios

As discussed in detail by Thole and van der Laan [Laa88a, Laa88b, Laa90a, Laa90d, Tho88b, Tho88c], the interplay between core hole spin–orbit coupling and core hole Slater integrals can give rise to non-statistical branching ratios.

In a single electron picture the overall intensity of the L_3 and the L_2 edges has a ratio of 2 : 1, as their J values are respectively 3/2 and 1/2 and the overall intensity is given by $(2J + 1)$ [Cow81]. This statistical value is found if the magnitude of pd Slater integrals is much smaller than the 2p spin–orbit coupling. From Table 9 it is evident that this is the case for all deep core levels. However for the 2p edge of iron the 2p spin–orbit coupling and the pd Slater integrals are of the same order of magnitude. This implies that the statistical branching ratio will be affected. In Fig. 29 the branching ratios are given for the divalent 3d transition metal ions in a cubic ligand field ($\mathscr{D}$) of 1 eV (the values are taken from [Laa88a]). Although the value of the branching ratio is mainly determined by the 2p spin–orbit coupling and the pd Slater integrals, the cause for a particular value is the symmetry of the ground state.

The ground state symmetry is determined by the dd Slater integrals (Hund's rules), the ligand field strength ($\mathscr{D}$) and the 3d spin–orbit coupling (ζ_d), as discussed above. An important factor for the branching ratio is the spin state, caused by the

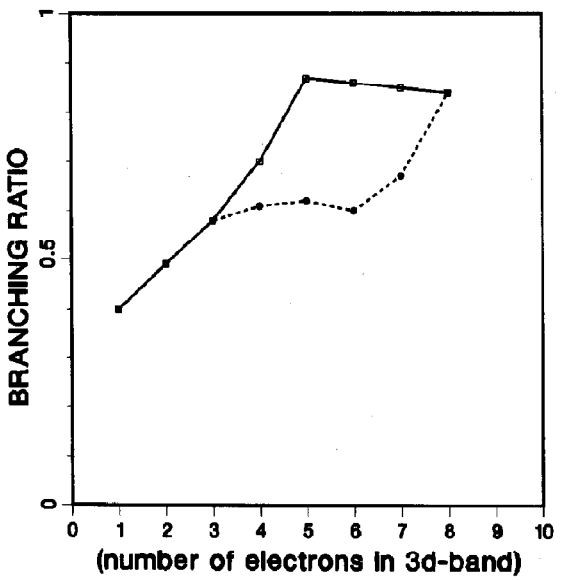

Fig. 29. Branching ratio of the divalent 3d transition metal ions as predicted from a ligand field multiplet model. High spin, squares and solid line; low spin, circles and dashed line.

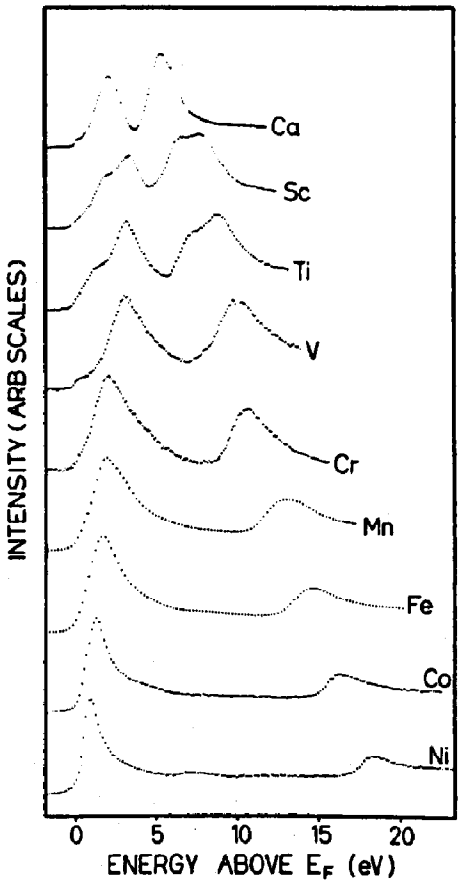

Fig. 30. The 2p X-ray absorption spectra of the 3d transition metals (from [Fin85]).

interplay of dd Slater integrals ("exchange") and ligand field strength. Within a particular high-spin or low-spin state the precise values of the ligand field strength and the 3d spin–orbit coupling have only a small effect on the branching ratio. This influence can be approximated as $\zeta_d/\mathscr{D} \approx 0.05/1.0$ [Laa90d, Tho88b]. This implies that for solids the potential influence of 3d spin–orbit coupling on the branching ratio is limited due to a finite ligand field strength. In the case of atoms (ions) 3d spin–orbit coupling can have large effects, such as for divalent nickel ions where 3d spin–orbit coupling causes a transition to be forbidden for right circularly polarized light [Laa91].

Also the branching ratios of the 2p spectra of the 3d transition metals are non-statistical as can be checked in Fig. 30. In the case of metals the ground state symmetry is basically described by band structure methods, where the Slater integrals (Hund's rules) enter under the heading of "orbital polarization". All metals can be assumed to contain a ground state symmetry analogous to a high-spin symmetry in 3d metal complexes and it is expected that in first approximation the branching ratios follow the trend given in Fig. 29.

These interplay effects between core hole spin–orbit coupling and core-valence Slater integrals are different for shallow core levels such as the iron 3p edge, which has a very small core hole spin–orbit coupling and is completely dominated by the Slater integrals. Deep core levels, such as ruthenium $L_{2,3}$ edges, will have a statistical branching ratio as they are separated by a large energy and no intensity can be transferred by the core hole Slater integral. However they still do affect the spectral shape of the individual edges (by interplay with the ligand field splitting), which causes small differences between the L_3 and L_2 edges [Deg••].

5.3. The short range model extended for multiplets

The short range (Anderson impurity) model has been extended to include multiplets by the groups of Kotani and Jo [Ima89a, Ima89b, Ima90, Jo88a, Jo88b, Jo88c, Jo89a, Kot89]. Its first application was to cerium compounds, but attention has since partly been shifted to transition metal compounds. The extra ingredient of its application to transition metal compounds is the inclusion of the cubic ligand field as has been discussed above. The inclusion of multiplets implies that for the localized configuration not a single state is included, but a series of states with different energy (ε_d) and symmetry (Γ) belonging to the ligand field multiplet. For the Hamiltonian of the short range model used this implies

$$\varepsilon_d n_d \Rightarrow \sum_\Gamma \varepsilon_{d\Gamma} n_{d\Gamma}$$

In general a single metal with 4 or 6 ligand atoms is described and the band-like states are also written out in the symmetries of the localized 3d

states. In practice this is accomplished within the ligand field multiplet model, by exciting a 2p electron to a "delocalized" *n*d state, representing the ligand band. In this manner the symmetries of the band-like states are more or less automatically formulated in the symmetry of the localized 3d states. The energy of these delocalized states ($\varepsilon_{pk\Gamma}$), relative to the localized states, is then set according to the charge transfer parameter

$$\sum_k \varepsilon_{pk} n_{pk} \Rightarrow \sum_{k,\Gamma} \varepsilon_{pk\Gamma} n_{pk\Gamma}$$

The interaction-terms t_{pd} have to be given for all symmetries (Γ)

$$t_{pd} \sum_k (a_d^\dagger a_{pk} + a_{pk}^\dagger a_d) \Rightarrow \sum_\Gamma t_{pd\Gamma} \times \sum_k (a_{d\Gamma}^\dagger a_{pk\Gamma} + a_{pk\Gamma}^\dagger a_{d\Gamma})$$

The U-term is modified to include all higher-order effects and the 3d spin–orbit coupling. Here I will follow the notation used by the groups of Kotani and Jo [Oka92a]

$$U_{dd} n_d n_d \sum_{(4)} g_{dd} a_{d\Gamma_1}^\dagger a_{d\Gamma_2} a_{d\Gamma_3}^\dagger a_{d\Gamma_4} + \zeta_d \sum_{(2)} \mathbf{ls} a_{d\Gamma_1}^\dagger a_{d\Gamma_2}$$

The summation of g_{dd} is over four different symmetries (Γ_i) and the summation of the spin–orbit coupling is over two symmetries. In the final state the multiplet effects caused by the core states are also included

$$\varepsilon_c n_c \Rightarrow \sum_\Gamma \varepsilon_{c\Gamma} n_{c\Gamma} + \sum_{(4)} g_{cd} a_{d\Gamma_1}^\dagger a_{d\Gamma_2} a_{c\Gamma_3}^\dagger a_{c\Gamma_4} + \zeta_c \sum_{(2)} \mathbf{ls} a_{c\Gamma_1}^\dagger a_{c\Gamma_2}$$

The term g_{dd} includes the dd Slater integrals F_{dd}^0, F_{dd}^2 and F_{dd}^4 and g_{cd} includes F_{cd}^2, G_{cd}^1 and G_{cd}^3. The total Hamiltonian in the final state then consists of

$$\mathcal{H} = \mathcal{H}_{band} + \mathcal{H}_{3d} + \mathcal{H}_{mu} + \mathcal{H}_{ls} + \mathcal{H}_{mix}(+\mathcal{H}_c + \mathcal{H}_{c.mu} + \mathcal{H}_{c.ls}) \quad (19)$$

Table 10
The parameters of the short range model as used for the analysis of 2p XPS of the nickel halides, with ^{M} and without inclusion of multiplets

Compound	Charge transfer		Core potential		Coulomb repulsion		Hopping	
	Δ	Δ^M	$U_{\underline{c}d}$	$U_{\underline{c}d}^M$	U_{dd}	U_{dd}^M	t_{pd}	t_{pd}^M
NiF_2	6.5	4.3	7.0	7.5	5.0	7.3	2.0	2.0
$NiCl_2$	3.6	1.3	7.0	7.5	5.0	7.3	2.0	1.3
$NiBr_2$	2.6	0.3	7.0	7.5	5.0	7.3	2.0	1.4
NiO	7.0	2.0	7.0	7.5	5.0	7.3	2.3	2.0

For the ground state this is a two-state model: a ligand band ($\mathcal{H}_{band}$) and a localized 3d state including its spin–orbit coupling ($\mathcal{H}_{3d} + \mathcal{H}_{mu} + \mathcal{H}_{ls}$). In the final state a core state is added ($\mathcal{H}_c + \mathcal{H}_{c.ls}$) and also its interaction with the 3d state is included ($\mathcal{H}_{c.mu}$). This Hamiltonian has to be solved for the initial state and final state and all transition matrix elements must be calculated, similarly as discussed before.

5.3.1. 2p XPS of the nickel halides

An important confirmation of the usefulness of the short range (Anderson impurity) model for the description of core spectroscopies is the description of the 2p XPS spectra of the nickel halides [Zaa86a]. No multiplet effects have been included and the description of the short range model as outlined in Section 4.3 is followed. The parameters as used are collected in Table 10. An equivalent analysis has been given in [Par88]. The ground state of all nickel halides is formed by a linear combination of $3d^8$ and $3d^9\underline{L}$ character. The $3d^{10}\underline{L}\underline{L}'$-states are positioned at high energy ($U_{dd} + 2\Delta$). U_{dd} is basically determined by the cation which is Ni^{2+} in all cases. The same holds for $U_{\underline{c}d}$. The hopping is determined from comparison to experiment. The t_{pd} given is the value for the e_g orbitals: $t_{pd} = \langle e_g|\mathcal{H}|\underline{L}(e_g)\rangle$. The value for the t_{2g} orbitals is smaller by a factor of two [Mat72a]. The effective hopping, denoted as V_{eff} in [Kot92], is $\sqrt{n_h} t_{pd}$ (with the number of holes (n_h) equal to 2). The value of Δ decreases from NiF_2 to NiI_2 and basically determines the

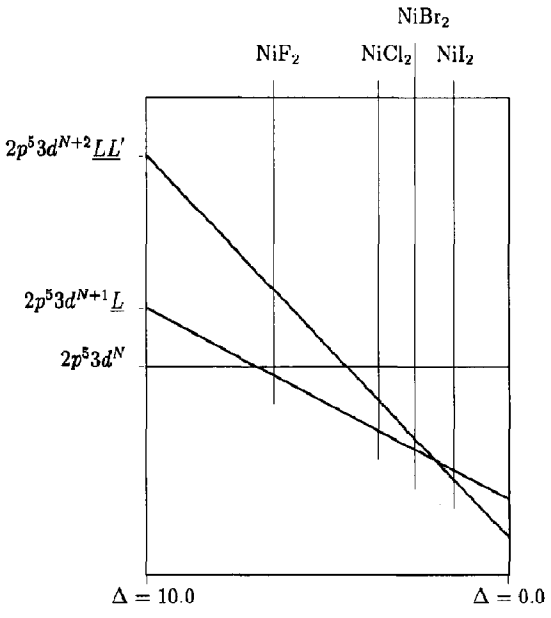

Fig. 31. The final state electronic configurations in 2p XPS of the nickel halides

ionicity of the system: NiF_2 is most ionic and contains only 14% of $3d^9\underline{L}$ character. In the final state of 2p XPS the configurations with extra 3d electrons are pulled down and Fig. 31 shows the final state configurations using the short range model without multiplets. The final state of NiF_2 contains close to degenerate d^8 and d^9 configurations, and the other three halides have close to degenerate d^9 and d^{10} configurations. This will give two peaks in NiF_2 in first approximation related to transitions from the $3d^8$ ground state to the bonding and antibonding combinations in the final state. The other halides will have three peaks because the $3d^{10}$ configurations enter the description.

Okada and Kotani [Kot92, Oka89, Oka90, Oka91a, Oka92a, Oka92b] performed calculations for the nickel halides in which they included the multiplet effects explicitly, as described above. The results of their method, denoted by them as the charge transfer-multiplet (CT-M) method, are given in Fig. 32. Though all features were already described without multiplets, the agreement with experiment has clearly been improved.

The values of U_{dd} and to a lesser extent also U_{cd} increased if multiplets were included. In [Oka92b] calculations have been done with and without multiplets and the values found for NiF_2 are larger if the multiplets are included; however the values without multiplets are also larger than the values used in [Zaa86a]. Important values for the final state are the ionic energy positions of the three configurations as sketched in Fig. 31. The positions of d^9 and d^{10} are respectively −0.5 and 2 in [Zaa86a], −2 and 3 in [Oka92b] (without multiplets) and −3.2 and 1 in [Oka92b] (with multiplets). Thus the ordering of the states is not modified, but there is some uncertainty in the relative energy

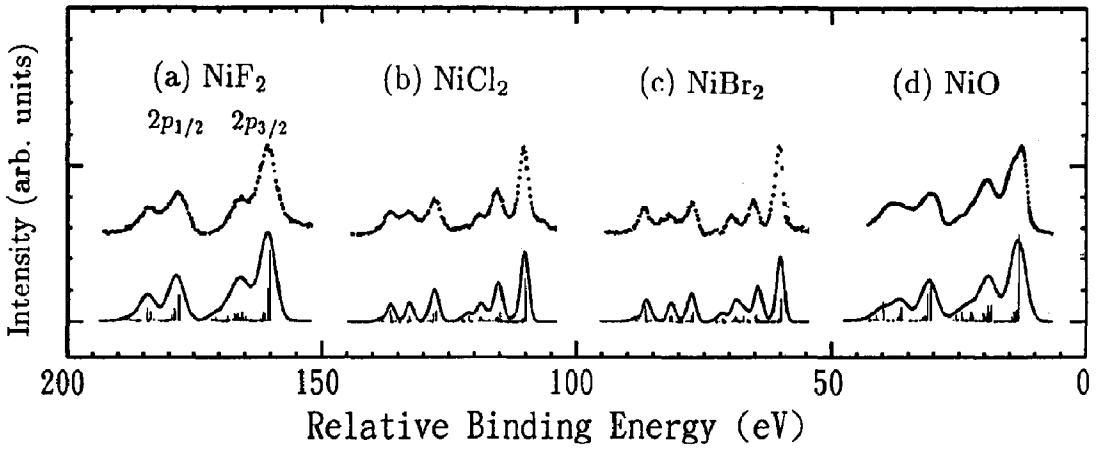

Fig. 32. The 2p XPS spectra of nickel compounds (a, NiF_2; b, $NiCl_2$; c, $NiBr_2$; d, NiO) (dots) compared with short range model calculations, including multiplets (bottom, solid line) (from [Oka92b]).

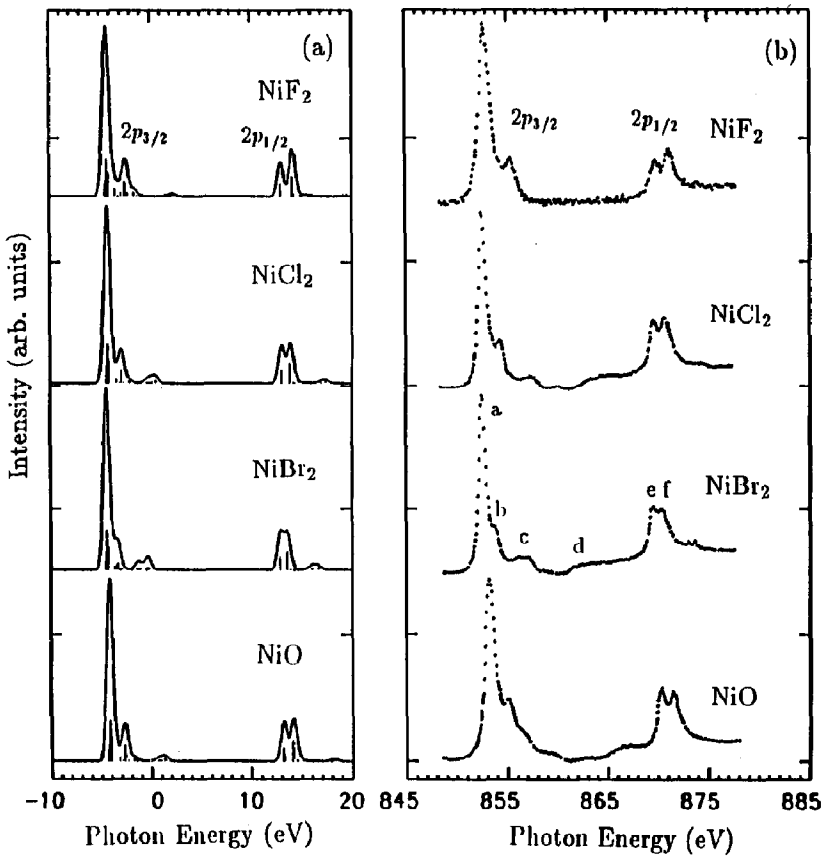

Fig. 33. The 2p XAS spectra of nickel compounds (left) (from [Laa86a]), compared with short range model calculations including multiplets (right) (from [Kot92]).

positions. Okada and Kotani argue that they need larger U values to account also for the spectral shape of the $2p_{1/2}$ spectrum, while in [Par88, Zaa86a] only the $2p_{3/2}$ has been analysed. Also it can be concluded that a smaller value of Δ must be chosen if multiplets are included.

A problem which is not touched in most papers is the additional interactions in the final state. It is assumed that the core hole only will give rise to local interactions, which can be gathered in one parameter U_{cd} [Saw88]. Also the values of the hopping and to a lesser extent U_{dd} need not be identical in the final state [Gun88a, Zaa86a]. This problem is discussed in Appendix A.

Recently the occurrence of non-local contributions to the screening has been shown to be important for 2p XPS of NiO (and in general charge transfer insulators) [Vee93a].

5.3.2. 2p XAS of the nickel halides

The important advantage of the short range model including multiplets, the CT-M model, is that it can also be applied to 2p XAS, which is dominated by multiplets and where in most cases charge transfer effects give rise to relatively small modifications. The 2p XAS spectra of the nickel halides have been measured by van der Laan et al. [Laa86a]. In their analysis they used both the ligand field multiplet model (for NiF_2) and the short range (Anderson impurity) model. Figure 33 shows the CT-M results of [Kot92], with the parameters as given in Table 10. In [Laa86a] a ligand field strength of 1.5 eV was used, while in [Kot92] a ligand field strength of 0.5 eV was used. Additionally the hopping was reduced from 2.0 eV to 1.5 eV in [Laa86a], to account for the difference in the final state. The analysis of [Kot92] gives the

best agreement with all spectral shapes. This confirms the fact that although 2p XAS is dominated by ligand field multiplets, the effects of charge transfer remain visible.

If one uses the ligand field multiplets without charge transfer the value of the cubic ligand field is considerably larger because one has effectively to include the difference in hopping between the t_{2g} and e_g states. The fact that $t_{pd\sigma} \approx 2t_{pd\pi}$ causes the largest contribution to the ligand field splitting in the short range model. This effect is not accounted for in the ligand field multiplet analysis and it must be incorporated in the value of 10Dq.

5.3.2.1. Reducing the Slater integrals. As was demonstrated in Section 4.3 in 2p XAS the final state value of Δ is equivalent to the ground state value, which largely excludes charge transfer effects. The main effect of charge transfer is a reduction of the multiplet splitting. This reduction can be applied directly to a ligand field multiplet by reducing the values of the Slater integrals.

Lynch and Cowan used this approach to simulate the $M_{4,5}$ edges of Ce^{3+} and Pr^{3+} [Lyn87]. The hybridization of ligand character $|L\rangle$ into the original atomic $|4f\rangle$ wavefunction was accounted for by reducing the ff Slater integrals by 20% and the df Slater integrals by 10%. Because the core states are not modified in a solid the reduction is about twice as large for valence–valence interaction than for core–valence interactions. The results of Lynch and Cowan [Lyn87] showed a complex reordering of states as a result of the Slater integral reduction.

To test the validity of Slater integral reduction and to compare it with the impurity model, the nickel dihalide spectra have been simulated [Deg91t]. The divalent nickel compounds are simulated as $3d^8 \rightarrow 2p^5 3d^9$ transitions. This presents a special case as the $2p^5 3d^9$ final state contains only a single 3d hole and does not contain any dd correlations. This simplifies the multiplet calculation and, apart from the spin–orbit coupling which is not essential for this problem, only two sets of Slater integrals remain: F^2_{dd} and F^4_{dd} for the initial state and F^2_{pd}, G^1_{pd} and G^3_{pd} for the final state. Furthermore the X-ray absorption spectral shape is not sensitive to the values of the ground state dd integrals as the $^3A_2$ ground state is the sole state of this symmetry and consequently does not mix with any excited state. The only set of parameters which determines the spectral shape is the final state pd Slater integrals. To test the Slater integral reduction they have been reduced stepwise from their atomic values and Fig. 34 shows the corresponding spectral changes. For a cubic ligand field a value of 0.9 eV is used, in agreement with the values determined from optical spectroscopy. (For NiO it is necessary to increase 10Dq to 1.5 eV.)

Reduction of the pd Slater integrals reduces the splitting between the main peak and its high-energy shoulder, a similar effect to that observed in going from NiF_2 to NiI_2. Also the modifications in the L_2 edge are reproduced nicely. From this agreement it can be considered that in the case of the nickel dihalides the Slater integral reduction gives a good account of the main spectral modifications upon increasing hybridization. A difference with the CT-M calculations is that the satellite structure is not reproduced by reducing the Slater integrals. It is important to note that the amount of Slater integral reduction gives an alternative measure of the amount of hybridization. For the halides it is found that whereas the fluoride corresponds to the atomic values, for chloride, bromide and iodide the Slater integrals have to be approximately reduced to respectively 75%, 65% and 25% of their atomic value. This trend is a nice example of the so-called nephelauxatic series obtained from the analysis of optical spectra [Jor62, Jor71].

5.3.3. General results of the short range model for 2p XAS

From the discussion of the nickel halides it is clear that the short range model including multiplets describes all observed features in the 2p X-ray absorption spectra. The trends in the spectral shape in going from fluoride to iodide are reproduced and the satellites are found at about the correct places

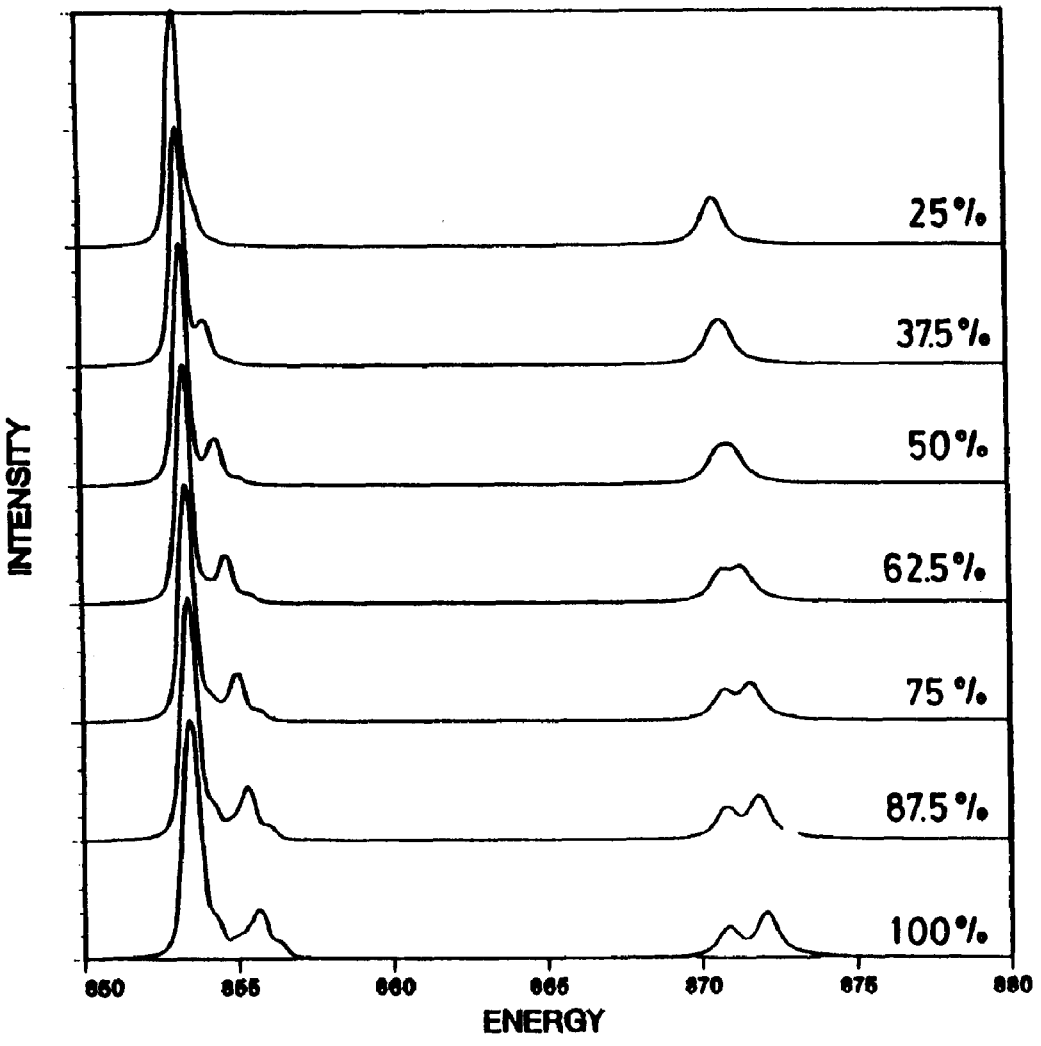

Fig. 34. $3d^8 \rightarrow 2p^5 3d^9$ ligand field multiplet calculations for divalent nickel. The Slater integrals have been reduced as indicated on the right (100% relates to the atomic values).

with correct intensities. As discussed the satellite structures are small because U_{dd} is about equal to U_{cd}.

A study of the 2p X-ray absorption spectrum (and 2p XAS) of CoO also shows good agreement [Oka92b]. Again there is some spread of the parameters used by different groups [Deg93a]. In particular the values for U_{dd} and U_{cd} as used in [Oka92b] are larger than the other studies. The effect of the short range model is a reduction of the multiplet peaks, which as discussed can also be simulated by Slater integral reduction [Deg93a].

Recently the short range model, including multiplets, has also been applied to early transition metal compounds, and in particular to tetravalent titanium oxides [Oka93]. The early transition metal oxides belong to a different class of materials (see next section) and the parameters of the short range model are different compared to the late transition metal compounds.

From Table 11 it can be seen that for TiO_2, U_{cd} and particularly U_{dd} are smaller, while Δ and t_{pd} are larger. Because the 3d band is empty the effective interaction V_{eff} is $\sqrt{(11/2)}t_{pd}$ compared with

Table 11
The parameters of the short range model as used by Okada and Kotani for the analysis of 2p XAS of various oxides

Compound	Charge transfer, Δ	Core potential, $U_{\underline{c}d}$	Coulomb repulsion, U_{dd}	Hopping	
				$t_{pd\sigma}$	V_{eff}
NiO	2.0	7.5	7.3	2.0	2.7
CoO	2.5	7.0	7.0	2.0	3.0
TiO_2	3.0	6.0	4.0	3.0	7.0

$\sqrt{2}t_{pd}$ for NiO. In general $V_{eff} = \sqrt{n_h}t_{pd\sigma}$, but because six of the ten holes for TiO_2 are of π origin, they must be accounted for with $t_{pd\pi}$, taken as half of $t_{pd\sigma}$. This modifies the calculation of V_{eff} to $\sqrt{(n_\sigma + (1/4)n_\pi)}$. Because of the large hybridization it is better to speak about a bonding and an antibonding combination of $3d^0 + 3d^1\underline{L}$, and similarly for the final state of $2p^5 3d^1 + 2p^5 3d^2\underline{L}$. As discussed, because of the cancellation effect of $U_{\underline{c}d}$ and U_{dd}, the satellites are weak as most intensity goes to the bonding combination.

In Fig. 35 the result of the short range model calculation is compared with a 2p X-ray absorption spectrum of $SrTiO_3$. The short range model reproduces the spectrum including the satellites correctly. For the main structures there are some changes: the first peak is sharpened compared to the ligand field multiplet model, while the other three main peaks are broadened because of the interaction with the band. In [Oka93] this finding is used to explain the experimentally found broadening. Other sources of broadening are symmetry reduction, which is important in for example $FeTiO_3$ and particularly TiO_2 [Deg90a] and the core hole life-time effects which are different for the different states and to first approximation are expected to increase for states at higher energy, and to be particularly large for the L_2 edge. Also some spectra, such as that for ScF_3 given in Fig. 19, do show an asymmetric first peak in experiment. Additionally it is noted that the ligand field multiplet spectrum of $SrTiO_3$ has a sharp leading peak (as can be checked in Fig. 20). The result given in Fig. 35 is not the optimized result as far as the ligand field multiplet model is concerned.

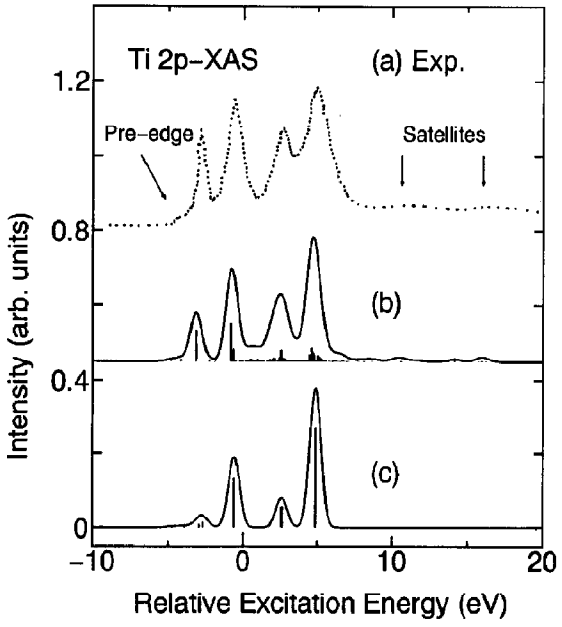

Fig. 35. Titanium 2p X-ray absorption spectrum of $SrTiO_3$ (top, a) compared with a CT-M calculation (middle, b) and a ligand field multiplet calculation (bottom, c) (from [Oka93]).

Thus although the CT-M model is necessary to explain the satellites, for the main peaks the ligand field multiplet calculations can compete with the CT-M results as far as accuracy is concerned, particularly if the Slater integrals are allowed to be reduced (though this is not necessary for systems with empty 3d bands). The main structures, including an accurate account of the intensity ratios, are obtained directly from the ligand field multiplet calculations, as has been discussed in Section 5.1. The CT-M results, though in principle better justified, give only a small improvement and have

an important drawback in the basic uncertainties in the parameters used. Particularly if one focuses on the symmetry properties of a system, such as Jahn–Teller distortions, high-spin to low-spin transitions, etc. it will be easier to study them with ligand field multiplets alone, because of computational limitations and also because of the relatively transparent meaning of all parameters used.

The use of the CT-M model implies for the satellites that they are of charge transfer nature, in contrast to the former assignment in terms of polaronic satellites [Boe84, Laa90b, Laa90c]. In fact the use of the charge transfer mechanism is questioned in these studies and the inclusion of an additional excitation mechanism is introduced to explain the relatively large satellites which were hard to explain. A definitive answer to the question of the relative importance of the different possible excitation processes is as yet not found.

5.3.4. Trends in the short range (Anderson impurity) model parameters

In this section some of the trends of the parameters in the short range model are discussed. As this is a whole subject of its own only some basic remarks will be made. A first estimate to the configuration averaged (see below) values of $\bar{U}_{dd}$ and $\bar{\Delta}$ can be made from the atomic estimates of the Slater integrals [Zaa86t]: $\bar{U}_{dd} \equiv E(3d^{N+1}) + E(3d^{N-1}) - 2E(3d^N) \approx P_{N+1}F^0(3d^{N+1}) + P_{N-1}F^0(3d^{N-1}) - 2P_NF^0(3d^N) \approx F^0(3d^N)$. In this formulation ligand field effects and the Slater integrals F^2 and F^4 have been omitted for the moment. The calculation is basically a counting of electron-pairs (P_N). The number of electron-pairs of the $N+1$ plus $N-1$ states exceeds the two pairs of the N states by 1 (for all possible N). Hence its value is basically determined by F^0 and the values of $\bar{U}_{dd}$ determined in such a manner gradually increase from about 15 eV for titanium to 18 eV for nickel, because the value of F^0 is gradually increasing with atomic number (Z) throughout the 3d series, mainly as a result of contraction of the 3d states.

For the charge transfer $\bar{\Delta}$ a decreasing trend is found and its value is a gradually decreasing function of Z ($\Delta = E(3d^{N+1}\underline{L}) - E(3d^N) \approx$ constant $- F^0(3d^N)$). Its value is about 31 eV for titanium and 28 eV for nickel. The parameters determined as such must be corrected for polarization effects in the solid. This effect is accounted for by a constant correction factor for both $\bar{U}_{dd}$ and $\bar{\Delta}$. This brings the values of $\bar{U}_{dd}$ to range from 3 eV for titanium increasing to 6 eV for copper and $\bar{\Delta}$ to range from 7 eV decreasing to 4 eV. For clarity it is noted that this general subtraction procedure is not exactly correct and the values found are not to be taken as quantitatively accurate.

5.3.4.1. Charge transfer versus Mott–Hubbard insulators. It has been shown by Zaanen et al. [Zaa85a] that the two parameters U_{dd} and Δ basically determine the nature of the band gap in transition metal compounds. The lowest states to be filled are always the empty 3d states. If $U_{dd} > \Delta$ the highest states to be excited are ligand p states, and if $U_{dd} < \Delta$ the highest states are the 3d states. This divides the transition metal compounds into two basic categories: charge transer systems versus Mott–Hubbard systems. See for example [Abb93b, Fuj93] for recent discussions on this matter. From the basic trends in $\bar{U}_{dd}$ and $\bar{\Delta}$ it can immediately be concluded that the early transition metal compounds will have a large tendency to be Mott–Hubbard systems and the late transition metal compounds are likely to behave as charge transfer systems.

5.3.4.2. Corrections due to multiplet and ligand field effects. The values for $\bar{U}_{dd}$ and $\bar{\Delta}$ have been determined with the average energies of the respective $3d^N$ configurations. However the determining energies are not these average values, but instead the lowest states in the respective multiplets. As has been discussed at length in Section 5.1 the energies in the ligand field multiplets of transition metal compounds are basically determined by the dd Slater integrals and the cubic ligand field splitting. These corrections can be worked out for the

Table 12
Corrections on $\bar{U}_{dd}$ and $\bar{\Delta}$ from the multiplet (B and C) and crystal field ($\mathscr{D}$) effects[a]

Configuration	Corrections on $\bar{U}_{dd}$		Corrections on $\bar{\Delta}$
$3d^1[^2T_2]$ and $3d^6[^5T_2]$	$-5B$	$(+2/5)\mathscr{D}$	$-5B\,(-2/5)\mathscr{D}$
$3d^2[^3T_1]$ and $3d^7[^4T_1]$	$-5B$	0	$-10B\,(-2/5)\mathscr{D}$
$3d^3[^4A_2]$ and $3d^8[^3A_2]$	$+4B$	$(+5/5)\mathscr{D}$	$-6B\,(+3/5)\mathscr{D}$
$3d^4[^5E]$ and $3d^9[^2E]$	$-8B$	0	$-14B\,(+3/5)\mathscr{D}$
$3d^5[^6A_1]$	$+14B+7C$	$(-5/5)\mathscr{D}$	$+7C\,(-2/5)\mathscr{D}$

[a] For the configurations $3d^6$ and $3d^9$ an extra correction of $+7C$ should be included for Δ. (The corrections for $3d^2$ and $3d^7$ states due to configuration interaction have been neglected.)

respective $3d^N$ configurations [Deg91t, Grf64, Zaa86t] and from this the corrections on $\bar{U}_{dd}$ and $\bar{\Delta}$ can be determined as indicated in Table 12.

Figure 36 gives the rough estimate for U_{dd} and Δ of divalent transition metal compounds based on the linear trend in their mean values and the corrections from ligand field and multiplet effects as indicated in Table 12. The parameters used were $B = 0.1$, $C = 0.4$ and $\mathscr{D} = 1.0\,\text{eV}$. It should be noted that these determinations of U_{dd} and Δ are only rough indications, merely to account for the trends, and do not have to be taken as absolute. More accurate empirical as well as theoretically determined values are given by, for example, the groups of Sawatzky [Vel90t, Vel91a, Zaa86t], Fujimori [Boc92a, Fuj93], Kotani [Kot92, Oka92b] and Oh [Par88]. As discussed there is a considerable variation in the parameters determined by different groups (with different models).

From Fig. 36 it can be seen that the main effect of the multiplet and ligand field effects is the increase in the values of U_{dd}, and to a minor extent also of Δ, for the $3d^3$, $3d^5$ and $3d^8$ configurations. This effect is superimposed on the respective increasing or decreasing trends. For all late transition metal oxides $U_{dd} > \Delta$, that is they all belong to the class of charge transfer systems. Also they are all insulating as Δ is still relatively large compared with $t_{pd} \approx 2.0\,\text{eV}$. Mn^{2+} has both very large U_{dd} and Δ

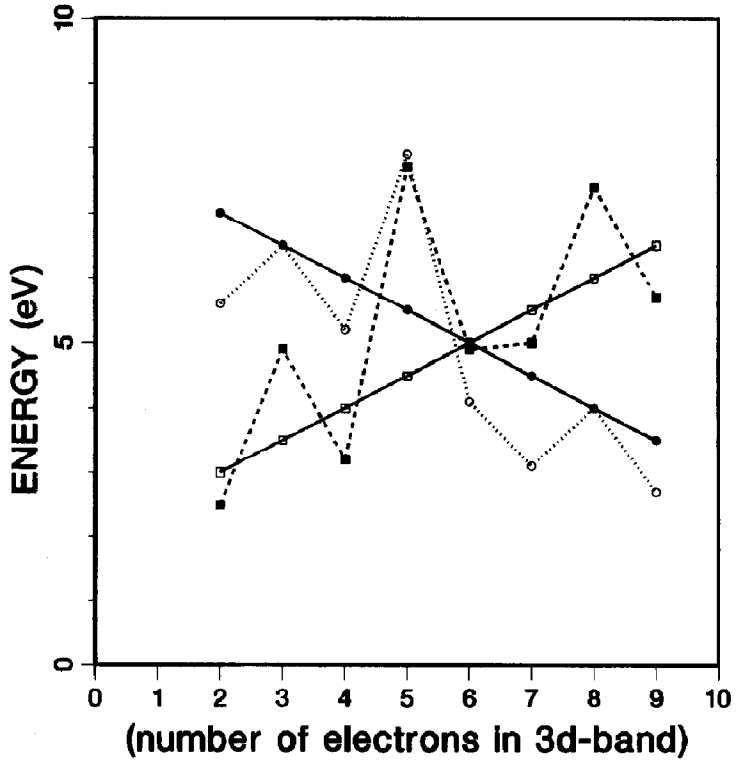

Fig. 36. Estimates for $\bar{U}_{dd}$ (□, solid line), U_{dd} (■, dashed line), $\bar{\Delta}$(●, solid line) and Δ (○, dotted line).

because of the exchange splitting of the five unpaired spins. Because both $3d^3$ and $3d^5$ are stable configurations, Cr^{2+} is liable to be unstable with respect to charge disproportionation. The band gaps of the early transition metal systems are determined by U_{dd} and they are also predicted to be closer to the metal–insulator transition point. In fact TiO and VO are both metallic.

5.3.4.3. Effects of different ligands. The effect of the ligands has been discussed for the case of the nickel halides and it has been found that the ligand largely determines the value of Δ and in first approximation does not affect U_{dd}. For empirical studies of these trends the reader is referred to the recent papers of Bocquet and co-workers [Boc92a, Boc92b] and Fujimori and co-workers [Fuj93]. $\bar{\Delta}$ is found to increase as, $F > O \approx Cl > Br \approx S > I \approx Se > Te$. Assuming a rigid shift of $\bar{\Delta}$ this effect will bring the late divalent transition metal sulphides and iodides closer to the metallic region and, for example, CoS and NiS are indeed metallic [Wis72]. Because of the large value of Δ of the $3d^5$ configurations, the divalent manganese compounds are insulating.

5.3.4.4. Effects of different valencies. For the general case of a formally trivalent transition metal ion we shall for simplicity assume that the change in Δ is a constant and as an example a value of 2.5 eV is subtracted. Also U_{dd} will be slightly affected and it is increased by 0.5 eV. An increasing valency will also increase the hopping (t_{pd}) and affect the ligand field splitting, which is approximately doubled from 1.0 eV to 2.0 eV [Sug70]. This relatively large increase of the ligand field splitting is mainly caused by the covalent contribution which is related to t_{pd}^2/Δ.

Figure 37 gives the rough estimates for U_{dd} and Δ of trivalent transition metal compounds based on the linear trend and the corrections from ligand field and multiplet effects as indicated in Table 12.

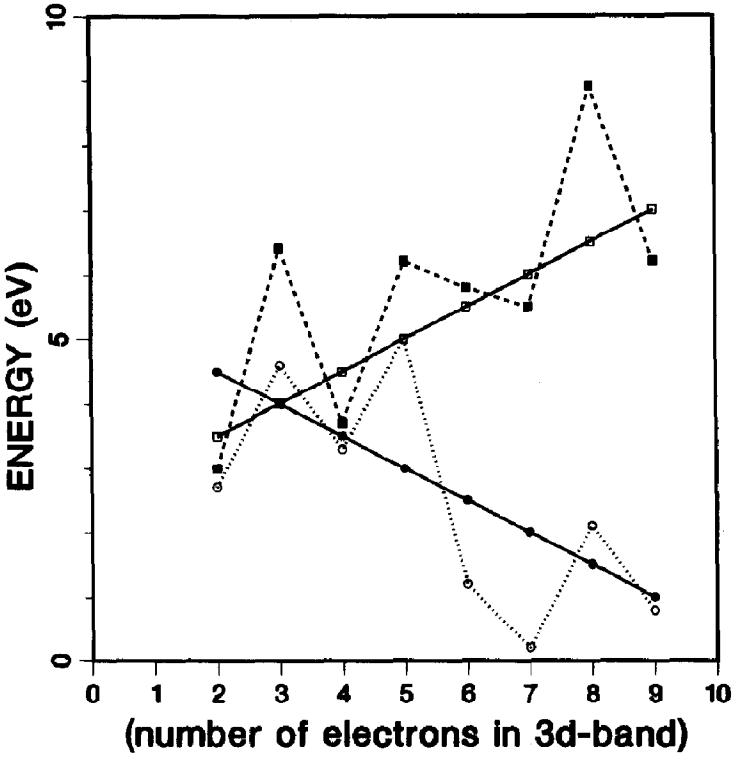

Fig. 37. Estimates for $\tilde{U}_{dd}$ (□, solid line), U_{dd} (■, dashed line), $\bar{\Delta}$ (●, solid line) and Δ (○, dotted line) for a trivalent transition metal oxide.

The parameters used were $B = 0.1$, $C = 0.4$ and $\mathscr{D} = 2.0\,\text{eV}$. The figure as drawn is probably most appropriate for the early trivalent transition metal ions. Trivalent iron oxides with a $3d^5$ configuration have large values of both U_{dd} and Δ and will form charge transfer insulators [Boc92a, Fuj93]. For a discussion of the tetravalent systems the reader is referred to [Boc92a, Fuj93, Deg91t].

5.3.4.5. Effects of the crystal structure. The links between crystal structure and electronic and magnetic structure are the subject of much research and can be found in the papers of, for example, Wilson [Wis72, Wis88], Goodenough [Gle85, Goo71] and Torrance et al. [Tor92], and references therein. As far as the short range Hamiltonians are concerned, the crystal structure will for all affect the hopping term t_{pd}. As discussed, a transition metal ion in a perfect octahedral surrounding of oxygen or a halide will obey the relation $t_{pd\sigma} \approx 2t_{pd\pi}$. Distortions from the octahedral symmetry would need the inclusion of more symmetry specific hopping terms, such as for example in [Laa92a] for D_{3d} symmetry. If one does not allow for more hopping terms, distortions are likely to mix the σ and π bonding of the ligands [Deg93a].

5.3.5. The relation with other parameter sets

Apart from the parameters of the short range model, there are other parameter sets which have been used to describe the transition metal compounds and complexes. For example much work has been done on the 2-parameter ligand field multiplet model, in which optical spectra have been described with two basic parameters: the ligand field splitting $\mathscr{D}$ and the Slater integral reduction B_{eff}. The variations in ligand field splitting have been described with the so-called spectrochemical series. The ligand field strength decreases C > N > O > F > S > Cl > Br > I [Sug70]. The variations in the Slater integrals are denoted as the nephelauxatic series: their values decrease as F > O > N > Cl > Br > I > S > Se > Te [Jor71]. The word "nephelauxatic" refers to an expanding cloud, and it can be seen that the series relates directly to the polarizability of the ligand. (Closely related to the nephelauxatic effect is the covalency factor N, which is used in papers on electron paramagnetic resonance (EPR); the Racah parameters are scaled down with N^4 and the spin–orbit coupling with N^2 [Cur74, Kua92].)

For fluorine the atomic value of the Slater integrals can be used and the values decrease towards tellurium. The nephelauxatic series runs in parallel with the variations in the charge transfer energy Δ. As discussed in Section 4 this relates to the fact that a decreasing Δ effectively increases the mixing of $3d^{N+1}\underline{L}$ in the ground state, which within a short range model description reduces the multiplet splitting. Within the short range model this reduction of Slater integrals can be estimated and Table 13 contains the reduction parameters as obtained

Table 13
The parameters of the short range model[a]

Compound	Charge transfer, Δ	Hopping, $t_{pd\sigma}$	Ligand field splitting, $\mathscr{D}$	Reduction, R/%
NiF_2	6.5	2.0	0.42 (0.79) 0.90	92 (99)
$NiCl_2$	3.6	2.0	0.63 (0.85) 0.95	82 (75)
$NiBr_2$	2.6	2.0	0.75 (0.95) 0.91	75 (65)
NiI_2	1.5	2.0	0.89 (0.99) 0.91	66 (25)
NiF_2	4.3	2.0	0.56 (0.92) 0.90	85 (99)
$NiCl_2$	1.3	1.7	0.74 (0.93) 0.95	65 (75)
$NiBr_2$	0.3	1.4	0.63 (0.83) 0.91	54 (65)

[a] Top series as used by Zaanen and co-workers; bottom series with modified parameters as used by Okada et al. An ionic contribution has been added for the ligand field values in brackets and in the third column the optical values are given. The reduction factors (R) are compared with the optimized values from the Slater integral reduction method (in brackets).

from the parameters of [Laa86a, Zaa86a]. The reduction factor can be determined from

$$R = \frac{1}{2} + \frac{\sqrt{(\Delta_{\Gamma_1}^2 + 4t_{pd}^2)} - \sqrt{(\Delta_{\Gamma_2}^2 + 4t_{pd}^2)}}{2\delta E} \qquad (20)$$

where Δ_{Γ_i} is the final state energy difference of a particular multiplet state Γ_i with the band. δE is the energy difference between the two multiplet states, which is equal to $\Delta_{\Gamma_1} - \Delta_{\Gamma_2}$. If the hopping t_{pd} is zero then $R = 1$. With increasing hopping (and constant charge transfer) R slowly decreases. From comparison with the values obtained from the Slater integral reduction method one finds that these values lie in between the values obtained from the two sets of parameters as used by Zaanen [Zaa86t] and Okada et al. [Oka92a].

The anion spectrochemical series has a more complex relation to the short range model. If Δ is decreased by constant t_{pd}, the ligand field splitting will increase due to the increased mixing of ligand p with metal d states. However the opposite trend is laid down in the spectrochemical series. This apparent discrepancy is related to the fact that the ligand field splitting is partly ionic in origin and the ionic contribution is related to the anion–cation distance, which for the halides is smallest for a fluoride (see for example [Deg90a]). The covalent contribution to the ligand field can be estimated from the short range model parameters as

$$\mathcal{D}_{cov} = \sqrt{(\Delta^2 + 4t_{pd\sigma}^2)} - \sqrt{(\Delta^2 + 4t_{pd\pi}^2)} \qquad (21)$$

The values of the ligand field in Table 13 are determined from the energy difference between t_{2g} states and e_g states assuming the rule $t_{pd\sigma} = 2t_{pd\pi}$. It is noted that if an ionic contribution to the ligand field splitting ($\mathcal{D}_{ion}$) is included this will increase the energy splitting for the σ interaction by $\Delta_\sigma = \Delta + \frac{1}{2}\mathcal{D}_{ion}$ and decrease Δ_π by the same amount. Effectively this will slightly decrease the covalent contribution to the ligand field splitting. By adding ionic contributions to 0.4 eV for fluoride (nickel–fluorine distance is 2.54 Å) and 0.25 eV for chloride (3.14 Å) and bromide (3.27 Å), the total ligand field splittings take the values given in brackets. Notice that the parameter set as used by Okada et al. [Oka92a] gives $NiCl_2$ a larger ligand field splitting than $NiBr_2$, in accord with experiment.

For the metal ions the spectrochemical series is $Mn^{4+} > Co^{3+} > V^{3+} > Cr^{3+} > Fe^{3+} > V^{2+} > Fe^{2+} > Co^{2+} > Ni^{2+} > Mn^{2+}$. The nephelauxatic series reads, $Mn^{2+} > V^{2+} > Ni^{2+} > Co^{2+} > Cr^{3+} > Fe^{3+} > Co^{3+} > Cu^{3+} > Mn^{4+}$. From the valency point of view the series are clear: Mn^{4+} has the largest ligand field splitting and the smallest Slater integrals, which is in accord with the large covalency of the tetravalent materials. Within the short range model, tetravalent materials will have a relatively small Δ compared with t_{pd} [Boc92a]. Within a certain valency the variations are in general small. The $3d^5$ systems have a large Δ and U_{dd}, so they are expected to be most "ionic", implying the smallest ligand field splitting and the largest Slater integrals. This is indeed reflected in the position of Mn^{2+} and Fe^{3+} in both series. For the crystal field a further expected trend is that the late transition metal ions are most localized and have the smallest ligand fields. An exception to this rule is Co^{3+} which turns over to a low-spin configuration thereby largely increasing its crystal field strength.

It is noted that the parameters in the short range model are further expected to have close relationships with, for example, the dielectric constants ($\approx$ Slater integral reduction) and the redox potentials ($\approx$ trends in U_{dd} and Δ). Also there are other models which try to explain the trends in the transition metals, of which the model of Wooley is an interesting alternative [Woo87]. This model uses U_{dd} and t_{pd} as in the short range (Anderson impurity) model (but omitting Δ) and is extended with the electron–lattice coupling effects (v) which can be of a large energy scale in localized systems [Woo87]. These electron–lattice coupling effects are missing in the present short range model approaches to core spectroscopy and a future extension in this direction will be important. A number of studies of short range (Anderson impurity) model calculations with coupling to

vibrations have been performed in the context of superconductivity. The coupling to the lattice can give rise to small polarons which form pairs, leading to the co-existence of narrow boson-pairs with wide fermion bands [Rob87].

6. X-ray magnetic circular dichroism (X-MCD)

In this section the question of the calculation of the X-ray magnetic circular dichroism (X-MCD) signal is addressed. Recently this field has gained much interest because of the promise of the determination of the ground state values of the spin and orbital moments using sum rules.

6.1. The atomic single electron model

An atomic, single electron, model has been worked out by Erskine and Stern [Ers75]. It describes the transitions of the 2p core state to the 3d valence state. $p \rightarrow s$ transitions are neglected and in the model core hole effects are neglected. The valence d states are explicitly written as an expansion of the spin and angular degrees of freedom, using spherical harmonics. The relative intensities of the reduced transition probabilities σ for the various possible combinations of polarization and magnetization are then worked out. They are collected in Table 14, under the additional assumption that the radial part of the matrix element is equal for $J = 3/2$ and $J = 1/2$ core states. For a mathematically rigorous determination of these values I refer to the paper of Brouder and Hikam [Bru91]; here I would like to concentrate only on the resulting numbers.

Table 14
Atomic, single electron model of $p \rightarrow d$ transitions; values given are the relative transition probabilities

Edge	Polarization	Magn. +	Magn. −	No magn.
L_2	+	3	1	4
	−	1	3	4
L_3	+	3	5	8
	−	5	3	8

From Table 14 all intensities and their ratios can be deduced. The overall $L_3 : L_2$ intensity ratio using linear (or non) polarized X-rays is 8:4, as given directly by the J value of the core state. This ratio is also found in the case of circularly polarized X-rays and a non-magnetic system. The X-MCD signal is defined as the normalized difference in absorption between right and left polarized X-rays

$$I_{\mathrm{MCD}} \equiv \frac{\sigma^+ - \sigma^-}{\sigma^+ + \sigma^-} \tag{22}$$

With this definition it is found that for the L_2 edge the X-MCD signal is $-1/2$ and for the L_3 edge it is $+1/4$, hence the $L_3 : L_2$ X-MCD intensity ratio is $-1:1$. The intensity ratios for right polarized X-rays can also be obtained directly from the table. They are 3:3 in the case of a parallel magnetic field and 1:5 for an antiparallel magnetic field. This atomic, single electron, model is often used as a starting point to analyse X-MCD spectra [Bau91, Bru91, Ers75, Kap91, Tob92]. In the following I will try to discuss how to proceed to other models. Here one can follow two routes:

(1) To include band structure effects, including the "Stoner" exchange splitting (I_s^*) and 3d spin–orbit coupling (ζ_d), with relativistic LSD calculations.

(2) To include the multiplet effects of the core hole in the final state.

6.1.1. X-MCD in the multiplet model

I will start with an outline of the second route, that is to include multiplets, in other words the core–valence Slater integrals as well as the valence–valence Slater integrals. In that case the 3J-symbol description, as explained in Section 4, is appropriate. For atoms the matrix element is given by the square of the 3J-symbol

$$\begin{pmatrix} J & 1 & J' \\ -M & q & M' \end{pmatrix}^2 \tag{23}$$

An atom in a magnetic field will have a ground state with $M = -J$. The spectral

Table 15
Branching ratios for different polarizations versus magnetizations; results are given for a series of ions within the atomic multiplet (AM) model[a]

System	Symmetry	Linear	Magn. −	Magn. +
AS-model	All	0.67	0.87	0.50
V^{4+}	$^2D_{3/2}$	0.46	0.63	0.41
Fe^{3+}	$^5T_2$	0.78	0.85	0.61
($\zeta_d = 0$)	$^5T_2$	0.72	0.86	0.59
	$^1A_1$	0.63	0.63	0.63
($\zeta_d = 0$)	$^1A_1$	0.60	0.60	0.60

[a] In the case of the Fe^{3+} ion a small (high-spin) and large (low-spin) ligand field has been added; the values are taken from Table IV in Ref. [Laa91]. The atomic, single electron (AS) model yields the same values for all ions.

shape for left respectively right polarized X-rays will be given by the squared 3J-symbol for respectively $q = \pm 1$ times the final state multiplet [Car91, Tho85a, Tho85b]. An important difference with the atomic, single electron, model is that the branching ratio will be affected by the symmetry of the ground state, which in turn is determined by the dd Slater integrals (Hund's rules). As discussed in Section 5.2.1, because of the interplay between core hole spin–orbit coupling and core hole Slater integrals the branching ratio will not be statistical.

In Table 15 the branching ratios are given for some transition metal ions, as calculated with the multiplet model. They are compared with the values from the atomic, single electron, model. The branching ratios are very sensitive to the ground state symmetry, which has been discussed in detail in Section 5.1 [Laa88a]. The branching ratio is always larger for a high-spin state; compare for example the $^1A_1$ and $^5T_2$ states of trivalent iron. As discussed in Section 5.2.1 the changes in the branching ratio due to the 3d spin–orbit coupling, that is the difference between $\zeta_d = 0$ and its atomic value, are not large (compared to the difference between high-spin and low-spin). Additional effects can occur due to further ligand field symmetry reduction, such as Jahn–Teller distortions.

6.1.2. X-MCD in short range models

As for the discussion of the spectral shape, for the X-MCD spectra the multiplet model can be extended to include charge transfer effects. The short range (Anderson impurity) model has been used to explain the X-MCD in the 2p X-ray absorption spectrum of nickel.

The ground state of nickel is expected to be rather well described with relativistic LSD calculations. This makes the use of short range models less justified compared with, for example, a charge transfer insulator such as NiO. However to account for a correct description of the localized final state of 2p X-ray absorption, including the action of the core-valence Slater integrals, it is necessary also to describe the ground state in a manner that can be used in a short range model analysis. There have been three papers on the description of the 2p MCD in nickel with short range models. In Table 16 the parameters used are collected.

The first calculation was performed by Jo and Sawatzky [Jo91]. They described the ground state of nickel as $17\%|d^8v^2\rangle + 65\%|d^9v\rangle + 18\%|d^{10}\rangle$, using the parameters as collected in the second column. v denotes delocalized electrons positioned in unoccupied states close to the Fermi level. Good

Table 16
Model parameters, ground state ionic energies and occupation numbers of three short range model calculations of nickel

Parameter	X-MCD [Jo91, Jo92]	X-MCD + XPS [Laa92a]	X-MCD + XPS [Tan92b, Tan92c]
Δ/eV	−1.0	+0.75	−0.5
U_{dd}/eV	5.0	1.5	3.5
U_{cd}/eV	6.0	2.5	4.5
t_{vd}/eV	0.65	⟨1.0⟩	0.7
Energies/eV			
d^8	4.0	2.25	3.0
d^9	0.0	0.0	0.0
d^{10}	1.0	−0.75	0.5
Ground state/%			
d^8	17	18	17
d^9	65	49	59
d^{10}	18	33	24

agreement with the 2p MCD spectrum of nickel was obtained. In the subsequent study of Tanaka et al. [Tan92b], the analysis was extended to also include 2p and 3p XPS spectra, which allow for a more critical test on some of the model parameters. It turned out that in order to describe the satellite structure in XPS accurately, it is necessary to decrease U_{dd}, $U_{\underline{c}d}$ and Δ as indicated in the last column. This modifies the energy positions of the different configurations. Because of the decrease of Δ and U_{dd} the energy difference between the lowest energy d^9 configuration and the d^{10} and d^8 configurations decreases. This mostly affects the occupation of the d^{10} configuration which is increased from 18% to 24%.

An alternative calculation by van der Laan and Thole [Laa92a] differs in some aspects. First the calculations of [Jo91] use only one interaction strength t_{pv}, while in [Laa92a] the states are projected to D_{3d} symmetry and different couplings are used for the different symmetries: $a \leftarrow t$, $e \leftarrow t$ and $e \leftarrow e$ ($D_{3d} \leftarrow O_h$). D_{3d} symmetry is chosen because the holes are expected to be formed near the L-points of the Brillouin zone. The ground state is notated as $|d^8\rangle + |d^9\underline{v}\rangle + |d^{10}\underline{v}^2\rangle$, instead of $|d^8v^2\rangle + |d^9v\rangle + |d^{10}\rangle$. That is, holes are used for the reservoir-states instead of electrons. The consequence is that the Δ as given in [Laa92a] (-0.75), must be reversed to $+0.75$ in order to bring it into comparison with the other calculations. A last point of difference is in the approach to $U_{\underline{c}d}$ which is assumed to be spectroscopy dependent and values of 2.5 eV and 4.5 eV are used respectively for XAS and XPS. In contrast with the other calculations, as well as with all calculations of Okada and Kotani discussed in Section 4.3, $U_{\underline{c}d}$ is not varied. For a further discussion of this point the reader is referred to Appendix A. For comparison it is noted that for the determination of the valence band photoemission spectrum of nickel a value of $U_{dd} = 4.3$ eV has been used by Falicov and Victora [Fal84, Vic85], using an exact solution of the Hubbard model in combination with the LSD calculation of Wang and Callaway [Wan77].

The different calculations can best be compared for their ionic energy positions as given in Table 16. It turns out that the ordering of states is different and while the d^{10} configuration is lowest for [Laa92a], the d^9 configuration is lowest for the other calculations. This has a direct consequence for the ground state occupation numbers, with the d^{10} configuration contributing more in [Laa92a]: 33% versus 24%. As far as the description of the spectra is concerned both calculations of [Laa92a] and [Tan92b] give good agreement with the observed spectral shapes in the XAS, X-MCD and XPS spectra. It is concluded that the short range model can give an accurate description of the spectral shapes and X-MCD of nickel, but to accomplish this task there is apparently still a reasonably large range of parameter combinations.

6.1.3. X-MCD in relativistic LSD calculations

A different route to explain the X-MCD spectra is to perform relativistic LSD calculations. This route is certainly most appropriate if multiplet effects can be neglected such as for the K edge of transition metals and (to a large extent) the $L_{2,3}$ edge of rare earths. However relativistic LSD calculations (and all other models neglecting the core hole effects) are not appropriate to describe the $L_{2,3}$ edge of nickel and the other 3d transition metals.

In Fig. 38 a schematic view is given of the various models with the important parameters which are included in various stages. In the band structure approach, the spin-polarized density of states is calculated using relativistic LSD calculations. To date relativistic LSD programs have been developed for KKR [Ack84], MS [Str89], LMTO [Ebe88a, Ebe88b] and ASW [Kru88]. The X-ray absorption spectrum and the X-MCD signal are determined from Fermi's golden rule (Eq. (4)) or with the Green function formulation (Eq. (6)). The relativistic LSD approximation includes the "magnetic" exchange effects and the 3d spin–orbit coupling exactly but neglects all core hole (exchange) effects in the final state. In Fig. 38 the

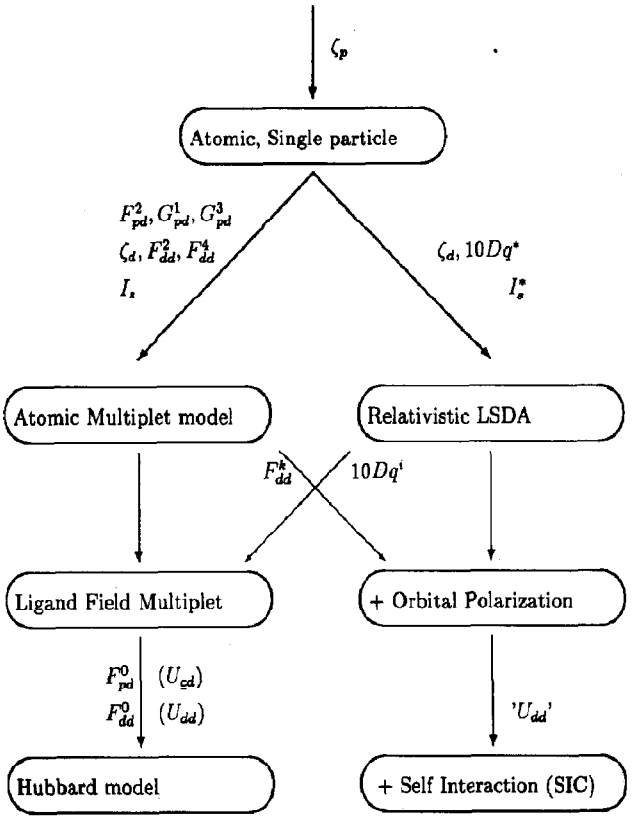

Fig. 38. Schematic picture of the models used for the analysis of MCD spectra.

3d spin–orbit coupling is denoted as ζ_d. The (magnetic) exchange coupling is denoted as I^*_s, that is within the calculational scheme the exchange is not a constant, but from the calculation an effective exchange coupling can be obtained. The same is true for the cubic crystal field splitting (10Dq*).

As has been shown by Schütz and co-workers [Fis90a, Sch87, Sch88, Sch89], an important experimental parameter is the normalized difference in absorption between right and left polarized X-rays as given in Eq. (22). If multiplets are not important it can be shown that its value is related as

$$I_{\mathrm{MCD}} \equiv \frac{\sigma^+ - \sigma^-}{\sigma^+ + \sigma^-} \cong P_e \frac{n^+ - n^-}{n^+ + n^-} \qquad (24)$$

where n is the spin-polarized projected density of states. P_e is a constant related to the Fano effect and its value is determined in the atomic single electron model: P_e is -0.5 for the L_3 edge and 0.25 for L_2. For K edges the value is only about 0.01 due to the absence of core hole spin–orbit coupling [Sch92]. Equation (24) implies that from the X-MCD signal the degree in spin-polarization of the ground state is obtained directly, or in other words as X-ray absorption is a local probe the local magnetic moment. This has been shown for 5d impurities in iron [Sch92, Wie91] and for a series of platinum alloys and Pt–Co multilayers [Ebe91, Rue91, Sch90] (but see next section on sum rules).

It appears that the magnetic moments as determined from X-MCD experiments and Eq. (24) do show close agreement with relativistic LSD calculations for the K edge of iron, the $L_{2,3}$ edges of 5d metals and the L_1 and $L_{2,3}$ edges of gadolinium

[Ebe88a, Ebe88b, Ebe89a, Ebe89b, Ebe90, Ebe91]. In these calculations the spin-up and spin-down projected density of states (of 3d systems) are determined by two important parameters, the 3d spin–orbit coupling and the effective exchange splitting between up and down.

Smith and co-workers [Che91, Smi92] explained the $L_{2,3}$ X-MCD spectrum of nickel from a relativistic LSD model. To obtain the correct branching ratios they had to renormalize the 3d spin–orbit coupling and the effective (Stoner) exchange splitting. This is in contrast to the approach by using the short range model including multiplets, where the largest contribution to the non-statistical branching ratios is the final state effects, that is, the core–valence Slater integrals. Because the core–valence Slater integral effects are important for the pure metals, as can be most directly seen from Fig. 38, a model which does not include them cannot be expected to be correct for the description of the spectral shape. Therefore the renormalization of the 3d spin–orbit coupling and the effective exchange coupling "hides" the final state core hole exchange effects in the ground-state description, which is not a preferable choice. Hence, an accurate description of the ground state is only possible with correct inclusion of final state effects.

6.2. Sum rules

Recently it has been shown by Thole, Carra and co-workers [Car92, Car93, Tho92] that the normalized integrated X-MCD signal can be related to the ground state expectation values of the orbital angular momentum $\langle L_z\rangle$ and the spin momentum $\langle S_z\rangle$. Using the discrete energy range of the $2p \rightarrow 3d$ transitions the optical sum rule as derived by Smith [Smi76] can be used to a good approximation for the $L_{2,3}$ edges of the 3d systems and the $M_{4,5}$ edges of the rare earths [Tho92]. We concentrate here on the $L_{2,3}$ edges which involve a p to d transition. In that case for the orbital moment divided by the number of holes of 3d character (n_h) one finds

$$\frac{\langle L_z\rangle}{n_h} = 2\frac{\int_{edge}(\sigma^+ - \sigma^-)}{\int_{edge}(\sigma^+ + \sigma^- + \sigma^0)} \tag{25}$$

$$\frac{\langle S_z\rangle}{n_h} = +\frac{3}{2}\frac{\int_{L_3 edge}(\sigma^+ - \sigma^-) - 2\int_{L_2 edge}(\sigma^+ - \sigma^-)}{\int_{edge}(\sigma^+ + \sigma^- + \sigma^0)} \tag{26}$$

In the original papers [Tho92, Car93] the prefactors $l(l+1)+2-c(c+1)/l(l+1)$ (c denotes the angular momentum of the core state, l that of the valence state) and $l(l+1)-2-c(c+1)/3c$ were given. For a p ($c=1$) to d ($l=2$) transition they are respectively equal to 1 and 2/3. In using these sum rules the following assumptions have been made: (A0) The radial matrix element is assumed to be energy independent and is hence equal for the L_3 and L_2 edges. This approximation is assumed to hold to within 10%. Also relativistic corrections are not included. (A1) The intensity of the L_3 edge is assumed to be twice the intensity of the L_2 edge. This implies separable edges which, as indicated in [Car93], is correct to about 5% at the end of the transition metal series, but worse in the beginning due to the small core hole spin–orbit coupling. (A2) In the present discussion I omitted for simplicity the magnetic dipole operator ($\langle T_z\rangle$). If one includes a finite $\langle T_z\rangle$, $\langle S_z\rangle/n_h$ must be replaced by $\langle S_z\rangle + (7/2)\langle T_z\rangle/n_h$ [Car93].

These optical sum rules bear a close relationship to the semi-empirical rules as derived by Schütz and co-workers [Sch93, Wie91]

$$\frac{\langle L_z\rangle}{n_h} = \frac{1}{3}\left[\int_{L_3 edge}\frac{4(\sigma^+ - \sigma^-)}{(\sigma^+ + \sigma^-)} + \int_{L_2 edge}\frac{2(\sigma^+ - \sigma^-)}{(\sigma^+ + \sigma^-)}\right] \tag{27}$$

$$\frac{\langle S_z\rangle}{n_h} = \frac{4}{3}\left[\int_{L_3 edge}\frac{(\sigma^+ - \sigma^-)}{(\sigma^+ + \sigma^-)} - \int_{L_2 edge}\frac{(\sigma^+ - \sigma^-)}{(\sigma^+ + \sigma^-)}\right] \tag{28}$$

As these rules were derived from a band structure point of view some additional approximations have been introduced. (A3) Instead of an integral of the dichroic signal and the total cross section, the dichroic signal is divided point by point (chosen because this is experimentally more appropriate). Mathematically this implies that the integration and division are exchanged, hence it is assumed that

$$\frac{\int x}{\int y} = \int \frac{x}{y} \tag{29}$$

This assumption is only exactly correct if the dichroic signal follows the total spectrum, that is if $y = c(\text{constant})x$. It can be expected that this assumption is appropriate if the spectrum consists of a single L_3 and L_2 peak without too much fine structure as often is the case for 3d metals. (A4) The use of $(\sigma^+ + \sigma^-)$ in the denominator implicitly assumes that $\sigma^0 = (\sigma^+ + \sigma^-)/2$, which is correct within band structure, but not necessarily so within multiplet theory.

We now rewrite the formulations (27) and (28) assuming that the approximations (A3) and (A4) hold exactly. In the first step we rewrite the denominator to $(\sigma^+ + \sigma^- + \sigma^0)$. The intensity of $(\sigma^+ + \sigma^-)_{L_3}$ is equal to $(2/3)(\sigma^+ + \sigma^-)$, following approximation (A1). Also, following (A4), $(\sigma^+ + \sigma^-)$ is equal to $(2/3)(\sigma^+ + \sigma^- + \sigma^0)$.

With these modifications Eqs. (27) and (28) are changed to

$$\frac{\langle L_z\rangle}{n_h} = \frac{1}{3}\left[\int_{L_3\text{edge}} \frac{4(\sigma^+ - \sigma^-)}{\frac{2}{3}\frac{2}{3}(\sigma^+ + \sigma^- + \sigma^0)} + \int_{L_2\text{edge}} \frac{2(\sigma^+ - \sigma^-)}{\frac{1}{3}\frac{2}{3}(\sigma^+ + \sigma^- + \sigma^0)}\right] \tag{30}$$

$$\frac{\langle S_z\rangle}{n_h} = \frac{4}{3}\left[\int_{L_3\text{edge}} \frac{(\sigma^+ - \sigma^-)}{\frac{2}{3}\frac{2}{3}(\sigma^+ + \sigma^- + \sigma^0)} - \int_{L_2\text{edge}} \frac{(\sigma^+ - \sigma^-)}{\frac{1}{3}\frac{2}{3}(\sigma^+ + \sigma^- + \sigma^0)}\right] \tag{31}$$

Then using the (mathematically incorrect) identity (A3) one finds

$$\frac{\langle L_z\rangle}{n_h} = 3\frac{\int_{\text{edge}}(\sigma^+ - \sigma^-)}{\int_{\text{edge}}(\sigma^+ + \sigma^- + \sigma^0)} \tag{32}$$

$$\frac{\langle S_z\rangle}{n_h} = 3\frac{\int_{L_3\text{edge}}(\sigma^+ - \sigma^-) - 2\int_{L_2\text{edge}}(\sigma^+ - \sigma^-)}{\int_{\text{edge}}(\sigma^+ + \sigma^- + \sigma^0)} \tag{33}$$

That is, one finds the correct optical sum rules as derived in [Tho92, Car93], but with a different prefactor. For $\langle L_z\rangle$ one finds 3 instead of 2; for $\langle S_z\rangle$ one finds 3 instead of 3/2. In other words in the semi-empirical rules as in [Sch93, Wie91] the factors used were too large (assuming the optical sum rules to be correct).

On the basis of a single particle transition, Stöhr and Wu [Sto93] also derived relations between the observed X-MCD signals and the orbital and spin-moments. Their rule for $\langle L_z\rangle$ is qualitatively equivalent to the optical sum rule, although their prefactor is different. For $\langle S_z\rangle$ they find a qualitatively different relationship, specifically related to their model description [Sto93].

6.2.1. *The use of the sum rules*

The sum rules present a powerful method to determine both the local spin and orbital moment. However in the practical use of the rules there are some problems which will be shortly discussed. The sum rules can be formulated as

$$\langle\ \rangle = cn_h f(\sigma^+, \sigma^-) \tag{34}$$

The constant c is known, but both the number of holes n_h and the experimentally determined function $f(\sigma^+, \sigma^-)$ present some complications.

To find the value for n_h one uses LSD band structure methods and determines site and angular momentum projections of the distribution of states. This gives the number of occupied states of metal 3d character n_d, and with $n_h = 10 - n_d$

the number of holes. There are two complicating factors. First the LSD methods used (LAPW, LMTO and ASW) do contain interstitial regions and/or empty spheres. It is not obvious what to do with the charge density in these regions. Secondly the radius of the sphere around the metal site is chosen to perform a correct calculation, but this sphere does not have much meaning in the sense that the metal atom ends there. That is, the determination of the amount of d character depends on the sphere size which is not obviously "correct" for this purpose. In fact because the experiment probes states starting from the 2p core state this makes the problem even more complicated, because one should use a radius (or radial function) related to the core wavefunction. The consequence is that the number of d character found is at the moment largely method-dependent and not uniformly defined. For this reason it is safer to give the expectation values per hole ($\langle L_z\rangle/n_h$).

To determine the experimental function $f(\sigma^+,\sigma^-)$ there are also some complications. One problem is related to the determination of the normalization by the total absorption cross section $(\sigma^+ + \sigma^- + \sigma^0)$. In an experimental 2p spectrum one finds not only the localized transitions to 3d states, but also the "step-like" absorption edge to delocalized states. Additionally the background is often not horizontal due to experimental conditions and sometimes other absorption edges. This gives a difficult task to first sort out the "correct" absorption spectrum and then to separate it into the localized part and the edge jump. This procedure leaves some space for particular treatments and hence systematic errors. For example it is not obvious how an edge jump should be included and also it is likely that the edge jumps are compound (crystal structure) dependent.

An additional experimental complication is the incomplete circular polarization. If the rate of polarization is known one can generate the 100% polarized spectra, however with loss of statistics. Some monochromators have energy-dependent polarization rates which further complicates this procedure. If one uses left and right polarization (instead of changing the magnetic field) one should take care of small energy shifts and small differences in the degree of polarization. Also the magnetization is in general not 100% and, depending on the detection technique (Section 2), sample preparation and cleaning procedures, the part of the sample under investigation is not always single phase and/or clean. In many cases a clean, single phase sample poses strong technological demands which are not always met. One should always be careful to have quantitative knowledge on the rate of polarization, magnetization and sample purity, if using the sum rules.

As shown by Carra et al. [Car93] the problems related to n_h as well as most experimental complications disappear, or at least strongly diminish, for the determination of the value for $\langle L_z\rangle/\langle S_z\rangle$. This ratio can be found by combining Eqs. (25) and (26)

$$\frac{\langle L_z\rangle}{\langle S_z\rangle} = \frac{4}{3}\frac{\int_{\text{edge}}(\sigma^+ - \sigma^-)}{\int_{L_3\text{edge}}(\sigma^+ - \sigma^-) - 2\int_{L_2\text{edge}}(\sigma^+ - \sigma^-)} \tag{35}$$

It can be seen that, apart from n_h, the normalization disappears from the formula. The remaining values for this ratio can be determined directly from experiment. Some of the experimental problems which remain are incomplete separation of L_3 and L_2, and some of the uncertainties caused by the rate of polarization and magnetization. The values for iron, cobalt and iron determined by this rule from X-MCD experiments do show close agreement with the available neutron data [Car93].

Wu et al. [Wuy92] have used the sum rule to analyse their data of cobalt and a Co/Pd multilayer. Using $n_h = 2$ they have found values for $\langle L_z\rangle$ of respectively 0.17 and 0.24, in good agreement with theoretical predictions from Daalderop et al. [Daa91]. It is noted that the choice for n_h to be equal to two is not well defined, as discussed above.

6.3. Linear dichroism

Linear dichroism, or polarization dependence, is the difference in absorption between transitions of X-rays with $q = \pm 1$ compared to X-rays with $q = 0$.

6.3.1. Experimental

Because synchrotron radiation is linearly polarized, the difference between normal incidence and grazing incidence probes the linear dichroism of the axis perpendicular to the surface, that is for example effects from the surface itself, or from perpendicular magnetization. Grazing incidence spectra are susceptible to "saturation effects", that is the electron yield intensity is not exactly proportional to the absorption coefficient. This happens because the penetration depth of the X-rays can become comparable to the escape depth of the electrons as has been analysed in detail for LaF_3 [Laa88c] and for thin layers of NiO [Ald93]. To avoid the complications due to these saturation effects it is preferable to avoid grazing incidence spectra. The angle at which saturation does not yet play a role depends strongly on the absolute absorption cross section, that is on the material and edge measured. If one wants to measure the linear dichroism spectrum for compounds with an electrostatic and/or magnetic axis, it is preferable to position the axis in the plane of the surface and to measure in normal incidence. In doing so one can measure the linear dichroism by turning the axis under consideration from horizontal to vertical, thereby avoiding any artefacts due to these saturation effects. Additionally the (eventual) linear dichroism effect due to the surface is not altered in this set-up.

6.3.2. Selection rules

The condition for the occurrence of linear dichroism is a macroscopic asymmetry in the electronic and/or magnetic structure. The symmetry criterion which determines a possible polarization dependence is given by the space group of the crystal and not by the point group of the atom. Consider for example a crystal which has a cubic space group and the absorbing atom a tetragonal point group. In this case the shape of the metal 2p spectrum is determined by the point group; however no linear dichroism is found because the potentially dichroic effect of the two atoms, oriented horizontally and vertically, cancels exactly [Bru90a].

The dipole transition can be denoted as P-like ($\Delta J = +1, -1$ or 0) in the atom. From Fig. 28 it can be checked that in octahedral symmetry no polarization dependence can occur, in contrast to tetragonal symmetry. The linear dichroism of all space groups can be deduced directly from the symmetry projection rules [But81]. For a D_{2h} space group there are three different directions, and in principle there will be linear dichroism effects with respect to all axes [Bru90a]. From Fig. 28 it is clear that the linear dichroism of quadrupole transitions (which have atomic D symmetry) is different, and already in octahedral symmetry linear dichroism effects occur. This can be used to distinguish quadrupole and dipole transitions [Bru90a, Hah82].

Linear dichroism can be caused by both electronic and magnetic effects, in contrast to circular dichroism which can only be caused by magnetic effects. Ligand fields can never cause a difference between the $\Delta M = -1$ and $\Delta M = +1$ transitions, which is a direct consequence of Kramer's theorem [Kra30] which states that the lowest state in a static electric field is always at least twofold degenerate. The only way to break the degeneracy of the Kramer's doublet is by means of a time asymmetric field, in other words a magnetic field.

6.3.3. Linear dichroism of layer compounds

Layer compounds contain at least one axis which is distinguishable from the others; hence the X-ray absorption spectra are polarization dependent with respect to this axis. For example $BaCoF_4$ crystallizes in a $C_{2v}^{12}(A_{2_1am})$ space group. Along the [001] direction (a axis) a macroscopic electric polarization has been found, which can be reversed by reordering the CoF_4 sheets. At room temperature

$BaCoF_4$ is ferroelectric and paramagnetic. Below $T_N = 68$ K it is antiferromagnetic [Kev70].

The cobalt 2p X-ray absorption spectra of $BaCoF_4$ show a large linear dichroism for $E \perp a$ and for $E \parallel a$ [Che90a]. It has been shown that the linear dichroism effects of $BaCoF_4$ can be simulated with ligand field multiplet calculations for a $3d^7_{HS} \rightarrow 2p^5 3d^8$ transition [Deg91t]. Atomic Slater integrals have been used and the atomic 3d spin–orbit coupling has been included. The calculations reproduce the observed temperature dependence of the dichroism. The temperature dependence shows a sudden step at 68 K, related to the additional linear dichroism effects of the magnetic exchange coupling [Sin••].

6.3.4. Linear dichroism of surfaces and adsorbates

A surface presents a clear breaking of the (x, y, z) symmetry, and will present a rather large linear dichroism between polarizations in the surface plane and perpendicular to it. A linear polarized X-ray impinging perpendicularly upon a surface excites core electrons to bonds lying in the surface plane. A grazing incident X-ray excites exclusively bonds perpendicular to the surface plane, which can be used to determine the surface electronic structure.

A problem with electron yield is that due to its mean probing depth of the order of 50 Å the surface signal is overwhelmed by the signal from the bulk. To separate the surface signal it is fruitful to use ion yield which, with its probing depth of only 1 or 2 layers, is a true surface probe. The combination of ion-yield and electron-yield detection has been applied to the CaF_2–Si(111) system [Him91].

Surface dichroism effects are particularly useful for adsorbates. A nice example is given for the adsorption of boron on a silicon (111) surface, for which the sharp boron π-peak, related to the silicon–boron bond, is visible solely with p-polarized X-rays [Mcl90]. Given that the adsorbates are present on the surface only, the X-ray absorption spectrum can be measured with any method [Ped89, Som92]. Because electron yield measurements are easier in their use, adsorbates are usually measured with (partial) electron yield. Besides an interest in the structure of the X-ray absorption edges, the surface extended X-ray absorption fine structure (SEXAFS) is important for the determination of, for example, the surface bond lengths [XAS91]. The common procedure of analysis for the "near edge structure" is by means of multiple scattering calculations. Emphasis is given to the complicated problem of correct determination of the surface structure [Ped90].

6.3.5. Linear dichroism of magnetic materials

Magnetic effects generate circular dichroism, but they also have a large effect on the linear dichroism as was first shown by van der Laan et al. [Laa86b]. The magnetic field determines an axial direction in the crystal and with respect to this axis linear dichroism occurs. Within atomic multiplet theory this can be calculated directly by evaluation of the properties of the 3J-symbol. Under the assumption that only the $M_J = -J$ magnetic level of the ground state is filled, a strong correlation between the polarization vector q and the various final states with different J values is found. This correlation is given in Table 17.

Atomic multiplet theory can be used directly for the rare earths and because the J values for the rare earths are found to be in between 5/2 and 8, $\Delta J = \pm 1$ transitions are almost exclusively correlated with $q = \Delta M_J = \pm 1$ transitions.

The polarization averaged spectrum is formed from a combination of all transitions from the $4f^N$ ground state of specific J to all $3d^9 4f^{N+1}$

Table 17
Correlation between ΔJ and ΔM_J

ΔJ	$(\Delta M_J = -q)$		
	-1	0	$+1$
-1	1	0	0
0	$\frac{1}{J+1}$	$\frac{J}{J+1}$	0
$+1$	$\frac{1}{(2J+3)(J+1)}$	$\frac{2J+1}{(2J+3)(J+1)}$	$\frac{(2J+1)(J+1)}{(2J+3)(J+1)}$

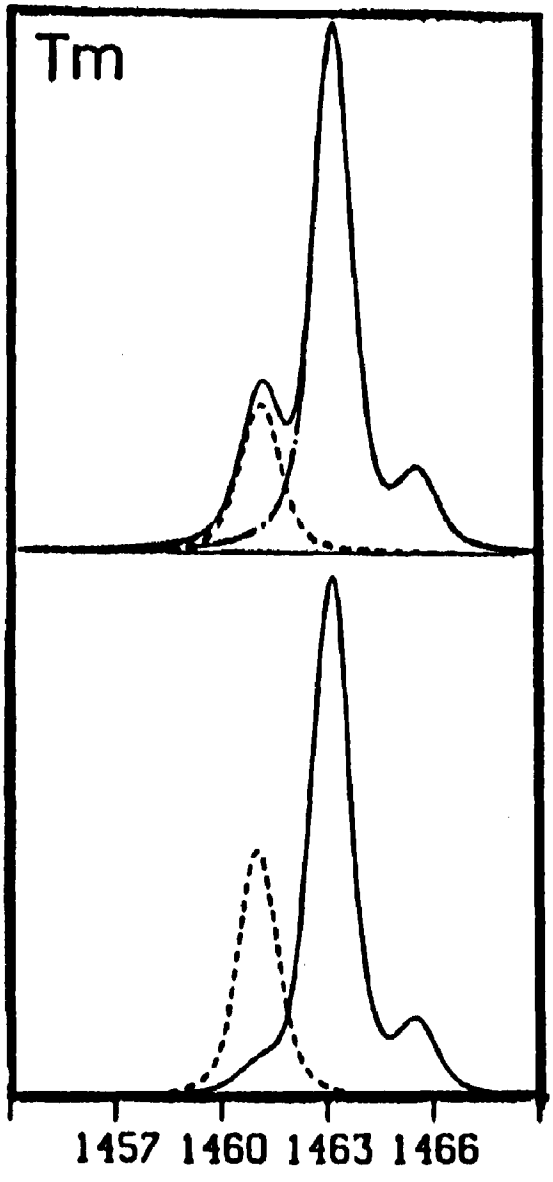

Fig. 39. Atomic multiplet calculation of M_5 edge of thulium. Top spectrum: – – –, $\Delta J = 0$ and –·–·–, $\Delta J = -1$, ——, total spectrum. Bottom spectrum: the resulting spectra for $E \perp M$ (– – –), and $E \parallel M$ (——).

final states of $J+1$, J and $J-1$, and it turns out that the oscillator strength to the final states of the different J values is grouped in different regions of the spectrum [Goe88]. Figure 39 shows the atomic multiplet spectrum for Tm^{3+}.

The M_5 edge has three possible transitions, the first one with $\Delta J = 0$ (dashed line) and the two others with $\Delta J = -1$ (chain-dotted line). Owing to the J_q correlation, the transitions to $\Delta J = -1$ are solely visible in the $q = \pm 1$ spectrum, and the $\Delta J = 0$ transition is largely restricted to $q = 0$ polarized X-rays. The small low-energy shoulder in the $q = \pm 1$ spectrum is an effect of the incomplete correlation. The linear and circular dichroism of the $M_{4,5}$ spectra of all rare earths, including the effects of finite temperature, have been given in [Goe88, Goe89t]. Experimental evidence of linear dichroism, caused by magnetic and electrostatic effects, is given in [Goe89t, Kap92t, Sac91a, Sac91b, Sac92a, Sac92b, Vog93]. For the 3d systems, a nice example of linear dichroism as a result of magnetic ordering has been given for the Morin spin–flip transition in Fe_2O_3 by Kuiper and coworkers [Kui93].

7. Overview of the published metal 2p spectra

In this section an overview is given of the published 2p X-ray absorption spectra. From papers which contain results on a series of minerals, complexes, etc., only some of the compounds will be included. The emphasis is on the papers which focus on the elaboration of the various theoretical models. For the 2p spectra this will be mainly the LFM model and its extension within the short range models, the CT-M model. However the one-particle models, be it LSD band structure or MS, are also developed further and applied to 2p spectra, although it has been argued in Section 5 that one of the crucial ingredients for the shape of the 2p spectra, the pd Slater integrals, is missing in these models.

The 2p spectra can be seen in analogy with a microscope as magnifying the symmetry of the ground state. The ground state symmetry can be studied with optical spectroscopy including X-MCD as well as resonance techniques (EPR, etc.), causing transitions within the $3d^N$ configuration, coupling to vibrations, etc. These studies give much detail and the question about the eventual additional information from X-ray excitations is understandable. However as discussed in

Table 18
Calcium 2p X-ray absorption spectra

Compound	Ref.	Remarks
Ca	[Fin85, Zaa85b]	Hubbard model on band structure
	[Him91]	Atomic multiplet
Ca on Si(111)	[Him91]	Atomic multiplet
$CaCO_3$	[Wad86]	–
CaF_2	[Deg90a, Him91]	LFM: 10Dq = −0.75 eV
	[Bor92]	MS: 10Dq = −1.36 eV
	[Ela93]	Autoionization
$CaCl_2$	[Ela93]	Autoionization
CaO	[Him91]	LFM: 10Dq = +1.2 eV
	[Sol91]	MS
$CaSi_2$	[Him91]	LFM
$Bi_2Sr_2CaCu_2O_8$	[Bor92]	MS

the preceding section, 2p X-ray absorption spectra show characteristic multiplets which can be related back to a particular ground state symmetry. This comes with the enormous advantage over optical spectroscopy of the element selectivity of X-ray absorption, with the opportunity to study in detail the ground state symmetry of low-concentration metal sites in a background of other metallic, inorganic or biological material. Hence, some of the important applications of 2p X-ray absorption can be found in the earth sciences, metal centres in organic complexes and biological systems and materials science. Other applications make use of the (circular) polarization of X-rays obtained at synchrotron radiation sources for the study of magnetic materials.

In the following sections the spectra of the 3d elements are collected and some of the papers focusing on a particular application are highlighted.

7.1. Calcium 2p X-ray absorption spectra

Metallic calcium has been studied in detail by Zaanen et al. [Zaa85b]. They analysed the spectrum as a combination of atomic multiplet effects and band structure. The spectrum, reproduced in Fig. 30, does show little structure and in fact it can be fully reproduced by a Gaussian broadening of the atomic multiplet, i.e. all information on the details of the band structure is lost.

2p X-ray absorption studies are only infrequently applied to surfaces due to the basic problem of a probing depth of 50 Å which always gives a dominant bulk contribution (for normal incidence spectra). The study of Himpsel et al. [Him91] uses ion yield to focus on the real surface layer of a CaF_2 crystal. The analysis with the LFM model shows that the surface introduces additional transitions due to a lowering of the symmetry. In a study by Borg and coworkers [Bor92], the L_2 edge of divalent calcium is considered as not affected by multiplet effects. They attribute the additional feature in between the two main peaks of the L_2 edge to effects of the solid state and show that it can be reproduced by a larger cluster for the multiple scattering calculations. In the LFM calculations this extra feature has been related to a reduced symmetry, as emphasized in the surface spectrum. If the structure is indeed present for the real bulk spectrum, solid state effects must be the cause. However in the spectrum taken of a CaF_2 sample covered with BaF_2, this feature is not present. It is present in other spectra only because of the surface sensitivity of electron yield. From Table 18 it can be seen that the result for the final state ligand field parameter is −0.75 eV with LFM and −1.36 with MS 1.36 eV is also the distance between the peaks in the experimental spectrum. A problem for the determination of the ligand field splitting in the final state of 2p XAS is its definition. In LFM the definition is the magnitude

Table 19
Scandium 2p X-ray absorption spectra

Compound	Ref.	Remarks
Sc	[Fin85, Zaa85b]	Hubbard model on band structure
	[Bar83]	Non-statistical branching ratio
ScF_3	[Deg90a, Set90]	LFM; 10Dq = 1.7 eV
Sc_2O_3	[Deg90a, Wad86]	LFM; 10Dq = 1.8 eV
	[Ela93]	Autoionization

Table 20
Titanium 2p X-ray absorption spectra

Compound	Ref.	Remarks
$CaTiSiO_5$	[Deg92]	Series of minerals
$LaTiO_3$	[Abb91b]	LFM
$La_{1-x}Sr_xTiO_3$	[Abb91b, Fuj92a, Fuj92b]	LFM, mixed valence
Ti	[Fin85,Zaa85b]	Hubbard model on bands
	[Bar83, Gru83]	LDA band structure
	[Lea80, Lea82]	EELS, MO picture
	[Pea86, Pco88]	Branching ratio
TiO_2	[Lea82, Wad86]	EELS
	[Deg90a, Deg92]	LFM, rutile + anatase
	[Laa90b]	"Polaronic" satellites
	[Oka93]	Charge transfer satellites
	[Bry89, Bry92]	MS, rutile + anatase
TiF_3	[Set90]	LFM gives no good agreement
$FeTiO_3$	[Deg92]	Series of minerals
$SrTiO_3$	[Deg92]	LFM: 10DQ = 1.5 eV

of the extra operator in the Hamiltonian with respect to the atomic multiplet. It has been shown in detail [Deg90a] that this does not correspond to a measured splitting in the experiment, though there is a constant (and known) relationship. The experimental splitting is a complex feature built from various ingredients and can be considered as an "effective ligand field splitting".

7.2. Scandium 2p X-ray absorption spectra

Only a few scandium 2p edges have been published. On comparing the spectra of ScF_3 and Sc_2O_3 with the theoretical ligand field multiplet spectra, both show good agreement (see Table 19). An important difference is the much sharper spectrum of ScF_3, which is a typical feature of fluorides [Deg90a]. Within the Anderson impurity description this is caused by the large value of Δ which gives fluorides a ground state which is strongly dominated by $3d^N$ (in this case $3d^0$) character, or in other words fluorides are close to the ionic limit. The admixture of more $3d^1\underline{L}$ character, for example, in the case of oxides implicates a larger broadening due to a large number of possible final states, as has been discussed in [Oka93].

7.3. Titanium 2p X-ray absorption spectra

For titanium compounds (Table 20) a number of problems are discussed frequently. First there is the evidence of a clear satellite structure in the titanium 2p spectra of tetravalent titanium oxides [Laa90b]. These satellites, and their analogues for 2p XPS, are discussed under the same charge transfer origin as the late transition metal oxides by Okada and Kotani [Oka93]. However it is claimed in papers of de Boer et al. [Boe84] and van der Laan [Laa90b] that the origin of the satellites cannot be of charge transfer nature. They formulate an alternative, polaronic, excitation process ($3d^N \rightleftharpoons 3d^N4d\underline{L}$), that is a transition from the valence band to the conduction band accompanying the X-ray absorption process. To date no clear-cut answer can be given to decide between these two (and eventual other) excitation processes.

A series of $La_{1-x}Sr_xTiO_3$ oxides have been measured [Abb91b, Deg90a]. In this series the formal valency of titanium is changed from tetravalent to trivalent, which can be equated with respectively "$3d^0$" and "$3d^1$" like configurations. The oxide systems are rather covalent so the actual electronic configuration has a considerable amount of $3d^{N+1}\underline{L}$ character; however as discussed the symmetry remains largely determined by the $3d^N$ nature. The $La_{1-x}Sr_xTiO_3$ series can then be used as a reference series for unknown mixed valent systems. A series of natural minerals has been published in [Deg92]. For all minerals measured, including a number of silicates, no trivalent titanium could be detected.

Table 21
Vanadium 2p X-ray absorption spectra

Compound	Ref.	Remarks
Cu_3VS_4	[Cre92]	Series of minerals
FeV_2O_4	[Cre92]	Series of minerals
V	[Fin85, Zaa85b]	Impurity model on band structure
VF_3	[Deg90b, Set90]	LFM
	[Tan92a]	LFM, temperature effects
V_2O_3	[Spa84, Abb93a]	LFM
VO_2	[Abb91a]	Phase transition
V_2O_5	[Deg91t, Abb93a]	LFM
$Zn_{1-x}Li_xV_2O_4$	[Deg91t]	LFM, mixed valence

7.4. Vanadium 2p X-ray absorption spectra

An important aspect of vanadium oxides is the occurrence of a series of phase transitions as a function of temperature in, for example, VO_2, V_2O_3 and $LiVO_2$ [Goo71], and also as a function of concentration in, for example, $Zn_{1-x}Li_xV_2O_4$ [Goo71]. For VO_2 it has been shown that this phase transition is reflected in the oxygen 1s X-ray absorption spectrum [Abb91a]. However the vanadium 2p X-ray absorption spectra show in general no clear sign of the phase transition (see Table 21). This can be related to the fact that the metal 2p X-ray absorption spectra are largely dominated by the local symmetry and are only slightly affected by the modifications in their surroundings (in the sense of ligand field effects), while most phase transitions for vanadium oxides occur due to some kind of vanadium–vanadium interactions and/or coupling to vibrations, which are only of relatively minor influence on the symmetry state of the vanadium ions. These effects can be expected to be of far more influence on oxygen 1s spectra which are directly related to the empty density of states. (In contrast if the spin state is affected in the phase transition, such as the high-spin to low-spin transition in $LaCoO_3$, this is directly and clearly observable in the metal 2p edges [Abb93b].)

7.5. Chromium 2p X-ray absorption spectra

Chromium compounds are on the borderline between the early, rather delocalized, transition metal compounds and the late transition metal compounds, dominated by localized features. CrO is a notorious compound because of its non-existence and the stable divalent chromium compounds are characteristic because of their strong Jahn–Teller distortions. Trivalent chromium has a stable $3d^3$ configuration such as in Cr_2O_3. Their 2p X-ray absorption spectra (Table 22) do correspond closely to the LFM calculations for a $3d^3[^4A_2]$ ground state. CrO_2 is ferromagnetic and recently its X-MCD spectrum has been measured [Knu93]. Because of its strong covalent character, it is rather surprising that this X-MCD spectrum can be simulated accurately with ligand field multiplet theory without the need to include charge transfer effects [Knu93].

Table 22
Chromium 2p X-ray absorption spectra

Compound	Ref.	Remarks
Cr	[Lea80, Fin85]	Branching ratio
CrF_2	[Set90]	Jahn–Teller distorted
CrF_3	[Nak85]	
Cr_2O_3	[Lea82, Krv90]	
CrO_2	[Knu93]	X-MCD
K_2CrO_4	[Deg••]	LFM, reduced Slater integrals
$CrAu_4$	[Pea86]	
$La_{1-x}Sr_xCrO_3$	[Pot••]	LFM, mixed valence

The chromium 2p spectra of the Cr^{6+} oxides are characteristic for a $3d^0$ configuration. In order to obtain quantitative agreement with the observed spectral shape the ligand field multiplet calculations must be performed with the Slater integrals decreased to about 25% of their atomic value [Deg••], a sign of the strong covalent character.

7.6. Manganese 2p X-ray absorption spectra

Most compounds contain manganese in its formal valencies 2, 3 and 4. Mn^{2+} contains five 3d electrons which in most compounds constitute a high-spin $^6A_1$ ground state. Divalent manganese compounds have large values of U_{dd} and Δ (see Section 5.3.4) and because of their A_1 nature their

Table 23
Manganese 2p X-ray absorption spectra

Compound	Ref.	Remarks
Mn	[Fin85]	EELS
$Mn_2(CO)_{10}$	[Hit90]	Series of complexes
MnF_2	[Nak85, Set90]	Crystal field effects
	[Deg90b]	LFM
$MnFe_2O_4$	[Cre92]	Series of minerals
MnO	[Deg91t]	LFM
	[Pat90, Spa84]	EELS
Mn_3O_4	[Krv90, Pat90]	EELS
Mn_2O_3	[Pat90, Spa84]	EELS
MnO_2	[Pat90, Spa84]	EELS
$MnPS_3$	[Ohn85]	
MnS	[Cra91b]	LFM, ligand field splittings
$KMnO_4$	[Spa84]	Mn^{7+}
$K_4Mn(CN)_6$	[Cra91b]	Low-spin Mn^{2+}
$LaMnO_3$	[Abb92a]	LFM
$La_{1-x}Sr_xMnO_3$	[Abb92a, Deg91t]	Mixed valence
$LiMnO_2$	[Deg91t]	LFM
$LiMn_2O_4$	[Deg91t]	LFM
Li_2MnO_3	[Deg91t]	LFM
$SrMnO_3$	[Deg91t]	LFM
ZnMnS	[Wei90]	Atomic multiplets

spectral shape is not sensitive to 3d spin–orbit coupling and symmetry distortions. These circumstances enable the 2p X-ray absorption spectra of divalent manganese compounds (see Table 23) to be described accurately by the LFM calculations [Cra91b]. One of the results of this comparison has been that the ligand field value determined as such is smaller (by 25%) than its optical analogue. The cyanide $K_4Mn(CN)_6$ contains divalent manganese in its low-spin configuration [Cra91b].

Mn^{3+} has a high-spin ground state of ^5E symmetry (in octahedral symmetry) susceptible to Jahn–Teller distortions. In addition this d^4 state is less stable than its d^5 and d^3 neighbours. Mn^{4+} has a stable $^4A_2$ ground state. In a study of the spectral variations with valency a series of lithium–manganese oxides have been measured. Figure 40 shows their spectral shape. The spectra show many-peaked fine structure and shift to higher energy with valency. The mixed valence series $La_{1-x}Sr_xMnO_3$ shows similar spectra to $LiMnO_2$ and Li_2MnO_3 [Abb92a].

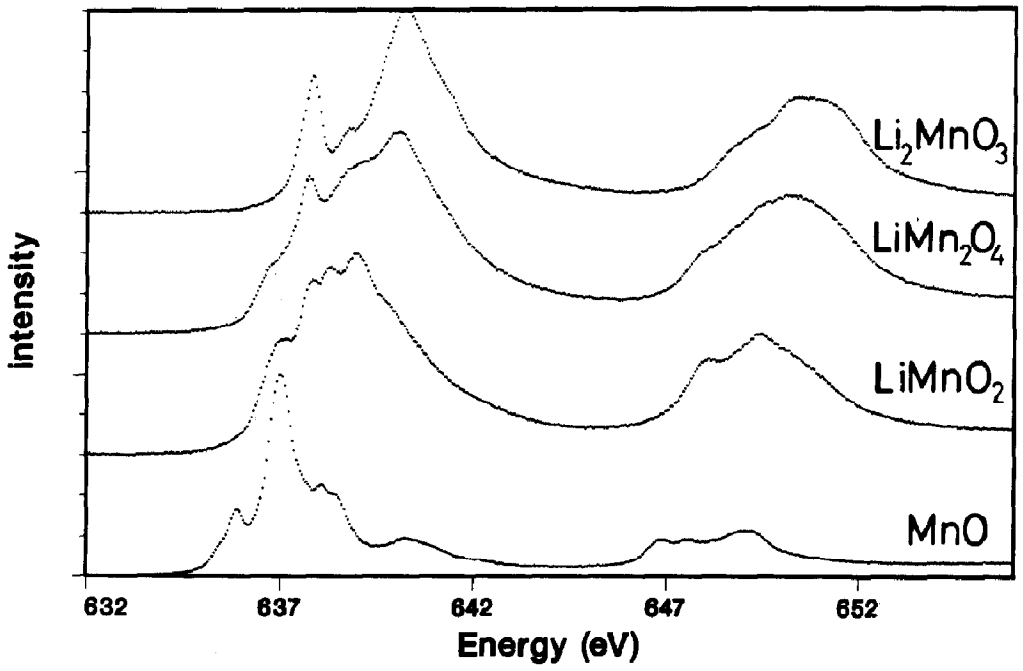

Fig. 40. The manganese 2p X-ray absorption spectra of a series of lithium manganese oxides: MnO + 1% Li (bottom), $LiMnO_2$, $LiMn_2O_4$ and Li_2MnO_3 (top).

7.7. Iron 2p X-ray absorption spectra

Iron has two basic valencies: divalent iron has a $3d^6$ configuration in either a high-spin ($^5T_2$) or a low-spin ($^1A_1$) state and trivalent iron is similar to divalent manganese and has in general a high-spin symmetry ($^6A_1$). Cyanides and some other complexes are low-spin ($^2T_1$).

The high-spin and low-spin states of divalent iron are close to degenerate in many divalent compounds and complexes. In a number of cases a transition occurs as a function of temperature and/or pressure. A nice example is $Fe(phen)_3(NCS)_2$, which undergoes a sharp high-spin to low-spin transition at 170 K (see Table 24). The iron 2p X-ray absorption spectra taken below and above this temperature are a direct confirmation of the respective spin states [Cat93].

The trivalent iron in Fe_2O_3 undergoes a magnetic phase transition at 250 K. In this so-called Morin spin–flip transition the high-spin state is not changed, but the direction of the magnetization is changed by 90°. As discussed, a magnetic field gives rise to both linear and circular dichroism, with the additional complication that the linear dichroism can also be caused by an asymmetric electrostatic field. The spectra for Fe_2O_3 below and above the Morin spin–flip transition temperature do show complete reversal of the linear dichroism signal, or in other words of the direction of the magnetic orientation in the crystal [Kui93].

Another range of problems is connected with the question of mixed valence, that is with systems containing both Fe^{2+} and Fe^{3+} in equivalent, or in non-equivalent sites. In such situations iron 2p X-ray absorption is a direct probe of the occurrence of the actual valencies and sites [Cre92]. However with regard to the nature of doping related effects on the electronic configuration 2p X-ray absorption is not a favourable spectroscopy, and instead more detailed information can be gained from, for example, oxygen 1s X-ray absorption [Abb92a, Deg91t] or photoemission experiments [Boc92a].

Like manganese, iron is an important element for metal centres in biological systems, such as, for example, rubredoxin. The iron 2p X-ray absorption spectra of rubredoxin of *Pyrococcus furiosus* have been studied in its oxidized and reduced form and the spectra can be related to respectively the Fe^{3+} and Fe^{2+} therein [Geo92].

Table 24
Iron 2p X-ray absorption spectra

Compound	Ref.	Remarks
Fe	[Gru83, Fin85]	Branching ratio
	[Set91]	X-MCD
$Fe(Cp)_2$	[Hit89b, Hit90]	(Cp = cyclopentadiene)
FeF_2	[Nak85, Set90]	Sharp features
$Fe(NEt_4)(Br_4)$	[Cat91]	Series of complexes
$Fe(Phen)_2(NCS)_2$	[Cat93, Che93]	Spin transition
FeO	[Col91, Lea82]	EELS
Fe_2O_3	[Col91, Krv90]	EELS, α and γ forms
	[Cat91, Wad86]	
	[Kui93]	LFM, Linear dichroism
Fe_3O_4	[Col91]	
FePC	[Koc85,Tho88a]	First use of LFM
Fe_3Pt	[May91, May92]	
$FePS_3$	[Ohn85]	
Amphibole	[Cre92]	Series of minerals
Chromite	[Taf82]	EELS, site specific detection
$CoFe_2O_4$	[Set91]	MCD
Fayalite	[Kri90]	Series of minerals
$Gd_3Fe_5O_{12}$	[Rud92, Set91]	MCD, temperature dependence
$La_{1-x}Sr_xFeO_3$	[Abb93b]	LFM, mixed valence
Leucite	[Kri90]	Series of minerals

7.8. Cobalt 2p X-ray absorption spectra

In the ligand field multiplet analysis of CoF_2 and CoO it became evident that the effects of 3d spin–orbit coupling are important [Deg90b, Deg93b, Tan92a]. This has been discussed in Section 5.1.4. For CoO a study including both charge transfer and multiplets has been performed by Okada and Kotani [Oka92b] (see Section 5.3.3). A detailed temperature dependent study of the linear dichroism of $BaCoF_4$ has been performed by Sinkovic and coworkers [Sin••]. In this study the peak-asymmetry related to the linear dichroism is shown to give a jump at the Néel temperature

Table 25
Cobalt 2p X-ray absorption spectra

Compound	Ref.	Remarks
Co	[Fin85]	Branching ratio
	[Set91]	X-MCD
Co on Si(111)	[Dec89]	Adsorption
Co/Pt multilayer	[Wuy92]	MCD, orbital polarization
$Co(Cp)_2$	[Hit90]	(Cp = cyclopentadiene)
CoF_2	[Deg90b, Set90]	LFM, 3d spin–orbit
	[Tan92a]	LFM, 3d spin–orbit and temp. dep.
$CoFe_2O_4$	[Set91]	X-MCD
	[Ima92]	X-MCD with LFM
CoO	[Krv90, Szy90]	EELS
	[Deg93b]	LFM, 3d spin–orbit
Co_3O_4	[Szy90]	
$BaCoF_4$	[Che90a, Set90]	Linear dichroism
$LaCoO_3$	[Abb93b]	High-spin to low-spin transition
$LiCoO_2$	[Deg93b]	LFM

which marks the onset of the additional linear dichroism effects of the antiferromagnetic ordering. At low temperatures $LaCoO_3$ has a low-spin ($^1A_1$) ground state. It is known that with temperature a gradual occupation of the high-spin ($^5T_2$) ground state takes place, which is nicely reflected in the cobalt 2p X-ray absorption spectra taken at different temperatures [Abb93b] (see Table 25).

7.9. Nickel 2p X-ray absorption spectra

The analysis of the nickel 2p X-ray absorption (and photoemission) spectra listed in Table 26 has

Table 26
Nickel 2p X-ray absorption spectra

Compound	Ref.	Remarks
Ni	[Fin85, Sha87]	Branching ratio
	[Lea80, Lea82]	EELS
	[Che91]	X-MCD
Ni on Cu(100)	[Tje91]	MCD, temperature and thickness dep.
NiAl	[Pea79, Sha87]	
$Ni_{1-x}P_x$	[Cho85]	
Ni_2Si	[Dep86]	
NiSb	[Sha87]	
La_2NiO_4	[Kui91]	
$NiBr_2$	[Laa86a]	Impurity model, CT-M
$NiCl_2$	[Bon66]	
	[Laa86a, Oka91]	Impurity model, CT-M
NiF_2	[Nak85]	
	[Laa86a]	Impurity model
NiI_2	[Laa86a]	Impurity model
NiO	[Laa86a]	Impurity model
	[Dav86a, Krv90]	
$Ni_{1-x}Li_xO$	[Kui90t]	Effects of doping
$LiNiO_2$	[Vel91b]	"LFM of $3d^8\underline{L}$"
$Cs[NiCr(CN)_6] \cdot 2H_2O$	[Sai93]	X-MCD

been discussed in detail in Sections 5.3.1 and 5.3.2. The X-MCD of the 2p X-ray absorption spectrum of nickel has been the stereotype for X-MCD spectra and analysis [Che91, Jo91, Laa92a, Smi92] and has been discussed in Section 6.

7.10. Copper 2p X-ray absorption spectra

The divalent copper oxides have attracted enormous interest because of the superconductivity found in doped, layered copper oxides. A divalent copper ion contains nine 3d electrons and its symmetry is ^2D. In octahedral symmetry the only non-occupied 3d state has ^2E symmetry, which is a Jahn–Teller sensitive state. The degeneracy of the d_{z^2} and $d_{x^2-y^2}$ orbitals will be broken and in the tetragonal, or ultimately square planar, surroundings the empty state will have $d_{x^2-y^2}$ symmetry. In actual systems the symmetry of the ground state can contain admixtures of other symmetries.

The copper L_3 (and L_2) edges of the copper oxides have been much studied (see Table 27). For papers published between 1987 and 1989 the reader is referred to [Als90]. The final state has the configuration $2p^53d^{10}$, that is the single hole has become occupied. Because in the final state the 3d band is full, the Slater integrals, which dominated the other 3d systems, become ineffective and do not play any role for the spectral shape. The spectrum will consist of a single transition to a $2p^53d^{10}$ "exciton" and at higher energy there will be structures related to unoccupied states of d and s character. The absence of Slater integrals implies that one-particle models should be correct to describe the spectral shape (taking into account the core hole potential, etc., as discussed in Section 8). For this purpose multiple scattering has been used [Bia92, Pom91]. It is found that in the undoped systems the "d^{10}" peak has constant energy [Pom91], while for doped systems the peak shows a small energy-dependence with polarization [Abb90, Bia88].

8. Metal and ligand 1s X-ray absorption

In this section the interpretation of both ligand and metal 1s X-ray absorption spectra is discussed.

Table 27
Copper 2p X-ray absorption spectra

Compound	Ref.	Remarks
$CuFeS_2$	[Gri89b]	Effects of valency
Cu_2O	[Hul84, Gri89b]	
	[Tje92a]	Resonant photoemission
Cu_2S	[Gri89b]	Series of compounds
Cu_3VS_4	[Cre92]	Series of minerals
Cu	[Fin85]	
	[Lea80, Lea82]	EELS
CuO	[Lea82, Krv90]	EELS
	[Lop92, Tje92a]	Resonant photoemission
$Bi_2Sr_2CaCu_2O_8$	[Tje92a]	Resonant photoemission
	[Bia92]	MS, polarized
$Bi_2Sr_2CaCu_2O_{8+\delta}$	[Bia88]	Polarized, shift of "d^{10}"
$Bi_{1.7}Pb_{0.3}Sr_2CaCu_2O_8$	[Abb90]	Polarized, shift of "d^{10}"
La_2CuO_4	[Gri89b]	
	[Pom91]	MS, polarized
$La_{2-x}Sr_xCuO_4$	[Als90]	Bibliography 1987–1989
	[Che92a]	Linear dichroism
$YBa_2Cu_3O_{7-x}$	[Als90]	Bibliography 1987–1989
$NaCuO_2$	[Kai89]	Cu^{3+}
Na_3CuF_6	[Cat90]	Cu^{3+}

In Sections 3 and 4 it has been explained that 1s X-ray absorption spectra can be rather accurately described with single particle methods within density functional theory. Both band structure methods and multiple scattering calculations can be used. From the work of von Barth and Grossmann [Von79, Von82] it is clear that one should include the core hole in the calculation, that is one should calculate the distribution of empty states in the final state of the absorption process; the final state rule [Alm83].

From the discussion in Section 3 it evolved that the two-electron Coulomb interactions in the 3d band might cause problems. For the distribution of empty states U is not important directly, but the "orbital polarization" (Section 3.8) might give rise to a modification of the spectral shape at the edge. They are discussed in Section 8.3.2.

According to the final state rule, the 1s X-ray absorption cross section is given as the squared transition matrix from the core state (Φ^c) to the empty valence states (Φ_p^v) times the p-projected final state density of states (n_p^*). The explicit relation has been given, for example, in the work of Müller and co-workers [Mul78, Mul82, Mul84].

$$\sigma = \frac{\omega}{6|\langle\Phi_p^v|}|\langle\Phi_p^v|\mathbf{r}_q|\Phi^c\rangle|^2 n_p^* \tag{36}$$

Because it is rather involved to calculate the final state density of states, often the ground state density of states is compared directly with the X-ray absorption spectrum. Final state calculations are discussed in Section 8.3.6. Also the matrix elements are not always calculated and instead the site (α) and symmetry (p) projected density of states (n_p^α) is used. This site and symmetry projection implicitly assumes the matrix element to be unity within the sphere allocated to a particular site, being zero elsewhere.

8.1. Band structure techniques

As discussed in Section 3.2 various methods exist to calculate the single particle density of states. A short overview focusing on the unoccupied states is given in [Zel92]. Frequently used techniques for X-ray absorption are the linearized augmented plane wave (LAPW) method, for example in [Mul78, Mul82, Mul84]; the linearized muffin-tin orbital (LMTO) method [And75, And84, And85], the augmented spherical wave (ASW) method [Wil79] and the localized (augmented) spherical wave (LSW) method [Leu90].

8.2. Multiple scattering formulation

An alternative route to the calculation of the X-ray absorption cross section is presented by the multiple scattering calculations. In multiple scattering theory the Schrödinger equation is reformulated in scattering theory. This approach is particularly appropriate for the calculation of the empty states which can be calculated for arbitrary large energies. Multiple scattering calculations are usually performed with the Green function approach, that is the Lippmann–Schwinger equation is used as the starting point. The Green function $\mathscr{G}_0 = (e^{ik|r-r'|})/(4\pi|r-r'|)$ describes the propagation of the electron in the solid, which is scattered by the atoms surrounding the absorbing atom. The X-ray absorption cross section is then written as a correlation function (compare with Eq. (8)) [Duh82, Vvd92]

$$\sigma \approx \mathscr{S} \sum_{L,L'} \langle\phi_i|\mathbf{r}_q|\tilde{\phi}_L^0(r)\rangle \tau_{LL'}^{00} \langle\tilde{\phi}_{L'}^0(r)|\mathbf{r}_q|\phi_i\rangle \tag{37}$$

where L stands for both l and m. $\tilde{\phi}_L^0(r)$ is essentially an atomic quantity and it is related to the wavefunction within the muffin-tin potential as discussed in [Gyo73, Vvd92]. $\tau_{LL'}^{00}$ describes the reaction of the surroundings containing all scattering paths. It can be rewritten to describe the effective reflectivity of the surrounding medium, transforming an outgoing wave from the excited atom to an incoming wave toward the excited atom [Vvd92]. For detailed accounts of the multiple scattering method the reader is referred to [Bru91, Nat86b, Reh93, Vvd92] and references therein.

There are a number of advantages of the multiple scattering formulation. Because it can be

performed as a cluster calculation, the calculations can relatively easily be done not only for the bulk but also for surfaces, interfaces, etc. In general any ordered and disordered system can be calculated. To accomplish this in a band structure calculation, in general the unit cell must be extended to account for the possible disorder effects, such as slab-calculations for surfaces, etc. This also implies that the core hole potential on the absorbing atom can be added directly in multiple scattering, while for a band structure calculation it necessitates super-cells (see below). Another advantage of multiple scattering is that it can be performed in steps of growing cluster sizes and it is an appealing picture to observe the (theoretical) spectral changes from the effects of increasing the number of back-scatterers and scattering paths around the absorbing atom. Also particular scattering paths can be selected, etc. A disadvantage of (most) multiple scattering calculations is that the potential used is not determined self-consistently.

It has been shown that the multiple scattering formalism and the band structure formalism indeed give equivalent results if worked out rigorously in their mathematical basis [Nat86a, Bru91, Reh93]. For comparison to experiment both the LSD and the multiple scattering results will be treated on the same footing, using the "density of states" picture as guidance.

8.3. Ligand 1s X-ray absorption

Ligand 1s X-ray absorptions have excitation energies which for the often studied light elements, carbon, nitrogen, oxygen and fluorine, are positioned between 300 and 700 eV, that is in the soft X-ray range. The interpretation of 1s spectra in the soft X-ray range is dominated by band structure approaches, in contrast to the hard X-ray region where multiple scattering is most often used. One of the reasons for this is the energy scale of the spectra. For soft X-rays most studies are oriented towards electronic structure determinations of correlated systems and in general only the first 20 to 30 eV of the edge are measured, with the focus on the states at the edge. This 20 eV energy range is relatively easily accessible with band structure methods, which offer the advantage of self-consistently determined potentials. In the hard X-ray range emphasis is on EXAFS analysis and the near-edge region is measured over its full range and analysed with multiple scattering over about 50 to 100 eV in many cases. Such an energy range is not trivially obtained with band structure methods; see Section 8.3.2.

8.3.1. Oxides with empty 3d bands

I will first focus on transition metal compounds with an empty 3d band. As an example the 1s X-ray absorption spectra of titanium oxides are discussed. Figure 41 compares the oxygen p-projected density of states with the oxygen 1s X-ray absorption spectrum of $SrTiO_3$ and TiO_2 (rutile) [Deg93a]. The spectra have been aligned at the position of the first peak. For rutile the spectral shape is reproduced and if the broadening is optimized a close to perfect fit of the experiment can be obtained [Deg93a]. It thus can be concluded that the density of states as obtained from a ground state calculation gives an accurate description of the oxygen 1s X-ray absorption spectral shape. This implies that, (1) the core hole potential does not have a large influence on the spectral shape, and (2) the transition matrix elements do not have to be considered explicitly. Thus in the case of TiO_2, the oxygen 1s X-ray absorption spectral shape gives a direct picture of the oxygen p-projected density of states. Overall, for $SrTiO_3$ similar features are also seen, though some difference between theory and experiment is observed. The sharp t_{2g} peak is followed by a small e_g peak in experiment, which is blurred by the next structure in the calculations. This difference is caused by the core hole potential [Deg93a].

The conclusion is that overall for transition metal oxides with an empty 3d band the oxygen p-projected density of states of a LSD calculation gives a good simulation of the spectral shape. As far as reproducing the oxygen 1s spectral shape

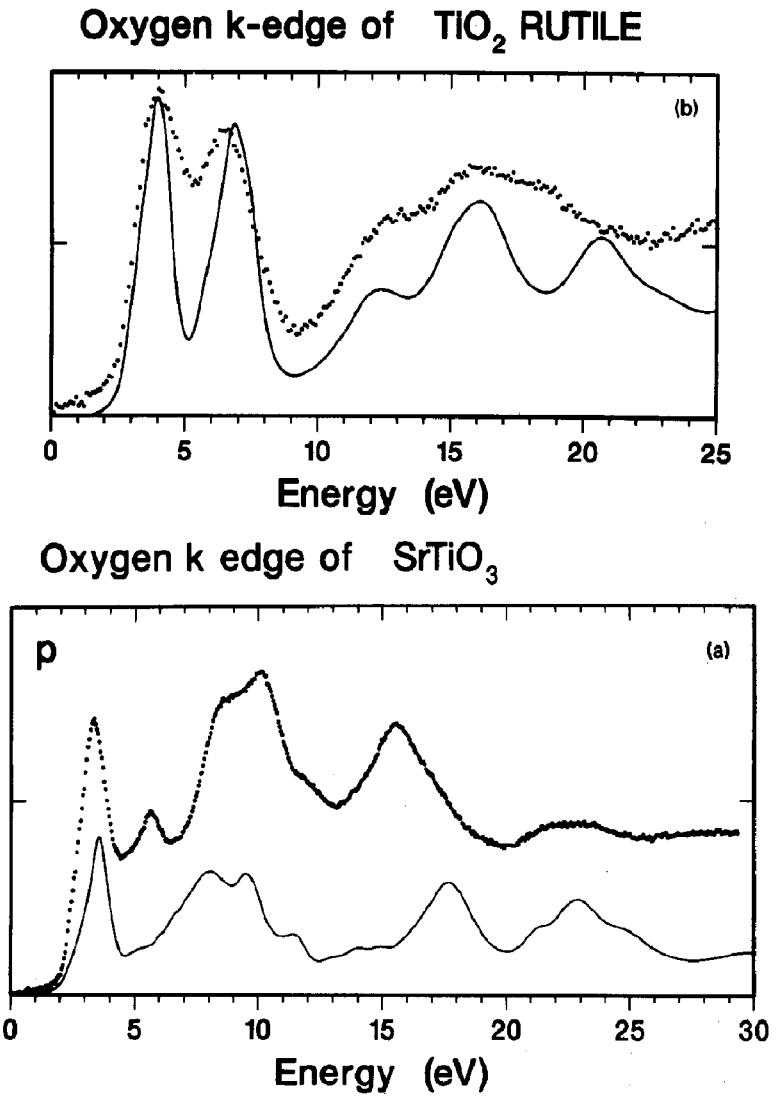

Fig. 41. Ground state oxygen p-projected density of states compared with oxygen 1s X-ray absorption spectra for (a) $SrTiO_3$ and (b) TiO_2.

is concerned, the effectiveness of the core hole potential largely depends on details in the crystal structure.

8.3.2. Oxides with partly filled 3d bands

For oxides with a partly filled 3d band some limitations of normal LSD calculations are met. This has been discussed in Section 3, where a number of recent extensions to LSD were briefly discussed. To account for the observed band gaps it seems to be unavoidable to include the Hubbard "U" in one way or another, such as is attempted in LSD + U calculations [Ani91a, Czy93] and also by LSD + SIC calculations [Sva92, Szo93]. For oxygen 1s X-ray absorption spectra, probing the unoccupied oxygen p states, it is important to remark that the unoccupied density of states is largely unaffected by self-interaction effects. The self-interactions directly affect only the occupied states and their effect on the empty states is indirect, via the reordering of the occupied states. The unoccupied density of states of the LSD + SIC

(and also the LSD + U) calculations performed so far [Ani91a, Czy93, Szo93] do show large similarities to their analogues as determined from normal LSD calculations [Ogu84]. This result leads to the conclusion that for comparison to oxygen 1s X-ray absorption spectra it is a rather good approximation to use the oxygen p-projected density of states of a LSD calculation.

In the literature comparisons between LSD results and oxygen 1s X-ray absorption spectra have been made for CuO [Gri89a] and $LiCoO_2$ (Czy92]. In both cases a close overall agreement has been found. Also for VO_2 and $LiVO_2$ [Pen••] and for MnO_2 and CrO_2 [Deg••] good agreement is found. The LSD calculations for MnO and CoO as performed by Terakura et al. [Ter84] show the empty spin-down t_{2g} and e_g bands split by the cubic crystal field, in close agreement with the oxygen 1s X-ray absorption results [Deg89, Deg91t].

Thus it can be concluded that the observations made so far do not pinpoint clear differences between LSD calculations and oxygen 1s X-ray absorption and fair agreement can be obtained.

8.3.2.1. Multiplet effects on oxygen 1s spectra. It has been argued that oxygen 1s spectra will be susceptible to multiplet effects, as far as the 3d part of the spectrum is concerned [Vel90t, Vel91a]. For transition metal oxides with a partly filled 3d band the two-electron Coulomb integrals are important for the electronic structure (see Section 3.8). Cluster calculations with the short range model including multiplet effects, originally developed for inverse photoemission spectroscopy (IPS), have been used to simulate the oxygen 1s X-ray absorption spectra of CoO and NiO [Vel91a]. The absorption process is simulated as the transition $3d^{N+1}\underline{L} \rightarrow 3d^{N+1}$ with the normal configurations for the initial and final states. Agreement has been found for both IPS and XAS, though there are problems with regard to the intensity ratio of the t_{2g} to e_g peak which is not correctly reproduced for X-ray absorption. Also there are questions with regard to the usability of the model because in the model the number of electrons is changed by 1, which is correct for IPS but not for X-ray absorption which is a charge neutral process and the extra valence electron is counterbalanced by the core hole, resulting in a charge neutral process. The "neglect of the core hole" leaves a number of uncertainties, for example, with regard to the parameters to be used in the final state. Because of these uncertainties it is not yet possible to give a detailed answer to the question of the importance of two-electron integrals in oxygen 1s X-ray absorption.

8.3.3. Oxygen 1s spectra of the "CuO" superconductors

The oxygen 1s X-ray absorption spectra of the high T_c superconductors, based on copper-oxide layers, have been much studied in the last six years, both experimentally and theoretically. The non-doped systems, for example La_2CuO_4, consist of a single peak at threshold followed by a structure related to the delocalized states. This single peak can be identified with a "$d^9 \rightarrow d^{10}$" transition, or more precisely a transition of $d^{10}\underline{L}$ character mixed into the d^9 ground state to d^{10}. This peak can be identified with the "upper Hubbard band" [Esk91a, Hyb92], but one can also formulate the transition in a single particle manner as the transitions to the empty states of the copper 3d band [Ben93]. As the Coulomb interaction U has no large effect on the description of the empty states no real distinction can be made between these two descriptions of the X-ray absorption spectrum.

Upon doping a new electronic state occurs related to Cu^{3+}. It has been shown convincingly that the ground state of Cu^{3+} is dominated by $d^9\underline{L}$ character, with little contribution of d^8; see [Esk92t] for an introduction and detailed explanations. In experiment a new peak evolves as a function of the doping, while the second peak drops in intensity. In the single particle (MS) description this is identified with the increased intensity of the 3d band due to the increased number of holes. (The lower energy is caused by the higher effective valence.) The total

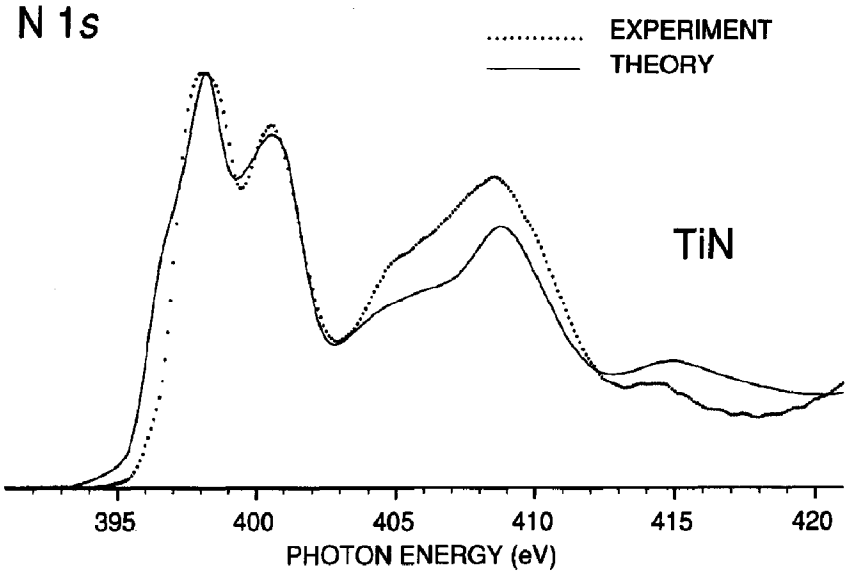

Fig. 42. Ground state nitrogen p-projected density of states (solid line) compared with nitrogen 1s X-ray absorption spectra for TiN (dots) (from [Sor93]).

spectrum is then formed by the addition of doped and undoped cases [Ben93]. In the correlated model Hamiltonian the two situations of Cu^{2+} (undoped) and Cu^{3+} (doped) are coupled and intensity is transferred to the peak at lowest energy, basically because of spectral weight interference effects [Esk91b]. (It is noted that the spectral weight transfer is zero in the ionic limit [Esk91b].) Though not all experimental data can clearly identify spectral weight transfer, it is clear in, for example, $La_{2-x}Sr_xCuO_4$ [Che92a] and Li-doped NiO [Kui89].

8.3.4. 1s Edges of nitrides, silicides and sulphides

For other, in general more covalent, ligands such as nitrides, silicides and sulphides a similar interpretation as for oxides is expected to hold. Thus their ligand 1s X-ray absorption spectra are expected to show close comparison to the projected density of states from LSD band structure calculation, which has been used for nitrides and silicides. For sulphides a comparison will be made with a multiple scattering calculation. For nitrides a detailed comparison between an LSD calculation and a nitrogen 1s spectrum has been published for TiN [Sor93], reproduced in Fig. 42. The calculation has been performed with the LSW method using an extended basis set in order to accurately reproduce the unoccupied states.

The sulphur and silicon 1s edges at about 1500 and 2300 eV have been traditionally more related to the hard X-ray absorption spectra interpreted with real space multiple scattering techniques.

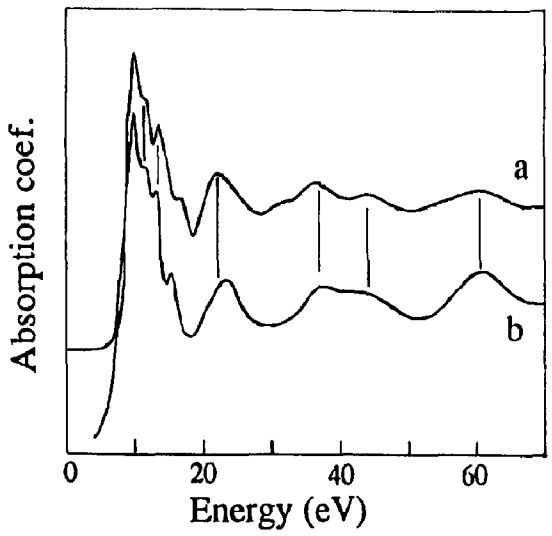

Fig. 43. Real space multiple scattering calculations (b), compared with the sulphur 1s edge of ZnS (a) (from [Sai89]).

For ZnS a multiple scattering calculation has been performed by Sainctavit et al. [Sai89], reproduced in Fig. 43. They used the "screened and relaxed" atomic potentials (implying the inclusion of the core hole potential) and found that best agreement with experiment is obtained with the use of the Dirac–Hara exchange potential. A disadvantage over LSD band structure calculations is that no self-consistent potential is used in these multiple scattering calculations, which leads to a basic problem that even if the calculated spectral shape converges for a particular cluster size, the uncertainty in the potential remains. An important advantage of multiple scattering is that if it is performed in steps of growing cluster sizes, an appealing picture is obtained of the relative importance of the various shells. The same is true if only a particular kind of scattering path is included and the effects on the spectral shape are monitored. For ZnS the spectral shapes are given for 1, 3 and 5 shells in [Sai90], where it is found that a five shell calculation is capable of reproducing the experimental spectral shape rather accurately.

The silicon 1s spectra of a series of transition metal silicides have been studied by Weijs et al. [Wey91]. They compared the observed spectral shapes with a series of ground state LSD calculations using the LSW method. As an example the comparison for the monosilicides is given in Fig. 44. Reasonable agreement could be obtained, though it is clear that in the experimental spectra weight appears contracted to lower energy. This phenomenon is likely to be related to the effect of the core hole potential, not included in the calculations as given in Fig. 44 (see below).

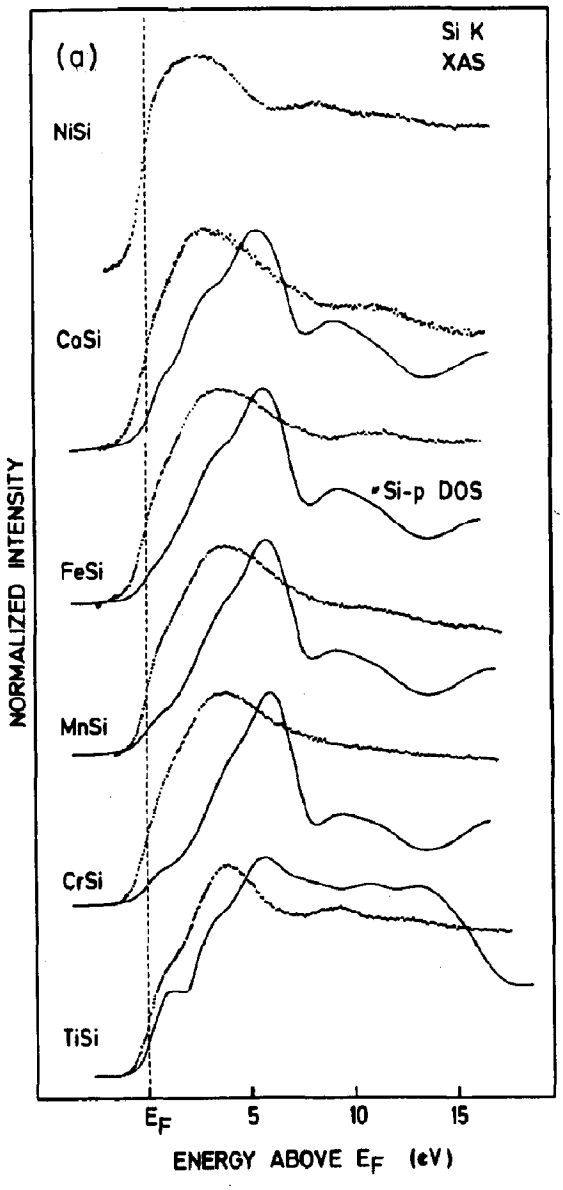

Fig. 44. Ground state silicon p-projected density of states compared with silicon 1s X-ray absorption spectra for a series of transition metal monosilicides (from [Wey91]).

8.3.5. Inclusion of the core hole potential

The core hole potential has been included in the LSD calculations by the removal of a core electron of one of the atoms. To reduce non-physical interactions between two sites with a core hole, the size of the unit cell must increase. For this so-called supercell, a new self-consistent calculation of n_{zN+1} instead of n_N must be performed. This approach has been applied successfully to the silver 2p edges of Ag_2O [Czy89, Czy90], the silicon 1s edge of TiSi and $TiSi_2$ [Czy90, Wey91] and the oxygen 1s edge of $LiCoO_2$ [Czy92].

The inclusion of the core hole potential has clear effects on the density of states of $TiSi_2$. If the unoccupied silicon p-projected density of states is compared with experiment a quantitatively correct

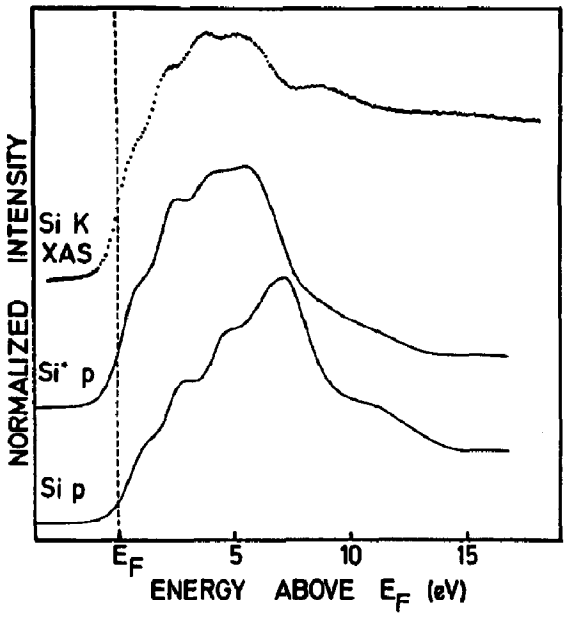

Fig. 45. Silicon p-projected density of states for the ground state (Sip) and final state (Si*p) compared with silicon 1s X-ray absorption spectrum of $TiSi_2$ (from [Wey91]).

"contraction" of the states is found as can be seen in Fig. 45. In some cases this core hole effect can also be simulated with a Clogston–Wolff model calculation using the ground state density of states as an input [Van90, Van90t, Wey91].

A second example of a calculation for which a super cell calculation of the final state is performed is the case of $LiCoO_2$. In $LiCoO_2$ cobalt has the low-spin $3d^6$ configuration ($^1A_1$ symmetry) and consequently the t_{2g} band is full, while all e_g states are empty. The oxygen 1s X-ray absorption spectrum probes the e_g band and at higher energies the other empty bands. Figure 46 compares the X-ray absorption spectrum with the density of states, with and without inclusion of the core hole. A general agreement is found and the overestimation of the intensity of the e_g band is clearly removed after inclusion of the core hole. The core hole effect as calculated for the $LiCoO_2$ spectrum confirms that an oxygen 1s core hole will pull down states to the bottom of

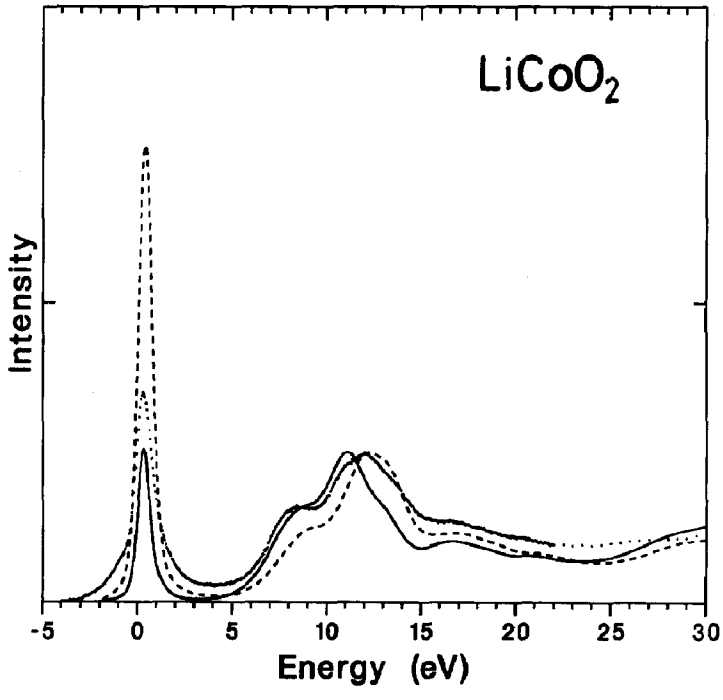

Fig. 46. The oxygen 1s X-ray absorption spectrum of $LiCoO_2$ (dots) compared with the broadened oxygen p-projected density of states. The dashed line refers to the ground state density of states. The solid line refers to the density of states after inclusion of the oxygen 1s core hole $\mathscr{P}_{\underline{c}N+1}$ (from [Czy92]).

the bands. This implies for 3d metal oxides that the dispersional broadening is counteracted. The bands at higher energy are less influenced because they are more extended. The main effect is a redistribution of spectral weight which in general results in an increase of intensity at the bottom of each band.

8.4. Metal 1s X-ray absorption spectra

The metal 1s edges can be interpreted with LSD calculations. As the core hole is created on the metal site, charge transfer (in this context denoted as "multichannel effects") might be expected to have a larger influence, as will be discussed below. The higher energy of the X-rays also makes quadrupole transitions more important, and they have to be considered.

8.4.1. Multiple scattering versus band structure

The metal 1s edges have energies ranging from about 4 to 9 keV. They are often used for EXAFS and their related near edge spectra, denoted as XANES in this context, are traditionally interpreted with multiple scattering methods. A reason for the use of multiple scattering (instead of band structure DOS) is that the XANES spectra are normally measured over an energy range of about 50 eV, which is not easily calculated with band structure methods based on basis functions (such as LAPW, LMTO, ASW and LSW). Real space multiple scattering, and its reciprocal space analogue (the so-called KKR method) do not enter into these basis set problems which makes them more suited for larger energy scales. However with the recent efforts to extend the basis sets to larger energy regions, dedicated to the unoccupied states, the band structure methods are applied also to metal 1s edges, at least for the first 30 eV above the edge [Czy93].

Multiple scattering calculations have been performed, for example, for a series of 3d metal oxides by Norman et al. [Nor85], for TiO_2 in the rutile and anatase forms by Brydson and co-workers [Bry87, Bry89, Bry92] and also by Ruiz-Lopez and Munoz-Paez [Rui91] and for a

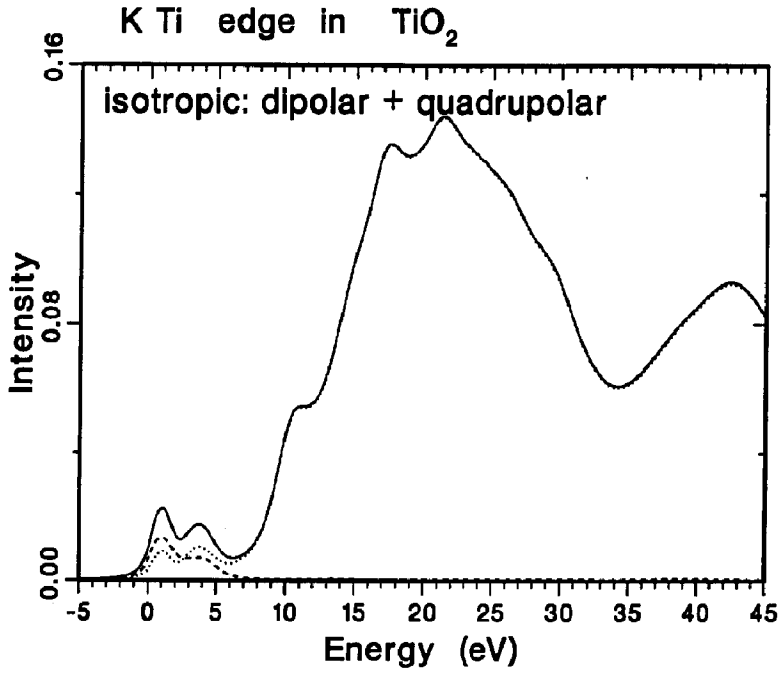

Fig. 47. Simulated titanium 1s edge of TiO_2 from a LSW band structure calculation by Czyżyk et al. [Czy••]). Indicated are the dipole transition (dots), the quadrupole transition (dashed line) and the total DOS (solid line).

Table 28
Ligand 1s X-ray absorption spectra for titanium compounds

Compound	Ref.	Element	Remarks
TiC	[Pfl82]	C	EELS
TiN	[Pfl82]	N	EELS
	[Sor93]	N	DOS from LSD
TiO	[Nak87]	O	MS
TiO_2	[Bro86a, Gru83]	O	Molecular orbitals
	[Deg89, Deg93a]	O	DOS from LSD
Ti_2O_3	[Bro86a]	O	
TiS_2	[Fis73, Ohn83]	S	
Ti_2S_3	[Bon86]	S	
TiSi	[Czy90, Wey91]	Si	DOS from LSD
$TiSi_2$	[Czy90, Wey91]	Si	LSD (core hole)
$La_{1-x}Sr_xTiO_3$	[Abb91b]	O	Mixed valence
$SrTiO_3$	[Deg93a]	O	DOS from LSD

high-spin to low-spin transition in an iron(II) complex by Cartier et al. [Cat93]. For TiO_2, band structure approaches have been used by Poumellec and co-workers [Pou91] and Czyżyk [Czy93]. As mentioned above the basic problem is the limited basis set which makes the calculation unreliable above a certain energy. The calculation of [Czy93] has the largest basis set and is expected to be reliable up to about 25 to 30 eV above the edge. The oxygen p-projected density of states of the ground state calculation is reproduced in Fig. 47. This result is in close agreement with experiment up to about 25 eV.

It is concluded that both band structure and multiple scattering methods are able to reproduce the near edge spectrum. Multiple scattering contains problems with regard to the choice of the potential, while band structure methods have a self-consistent potential but suffer from problems

Table 29
Ligand 1s X-ray absorption spectra for vanadium compounds

Compound	Ref.	Element	Remarks
V_2O_3	[Abb93a, Deg91t]	O	
VO_2	[Abb91a]	O	Phase transition
V_2O_5	[Abb93a, Deg91t]	O	
VN	[Pfl82]	N	EELS
V_2S_3	[Bon86]	S	
VSi_2	[Van90, Wey91]	Si	DOS from LSD
$Zn_{1-x}Li_xV_2O_4$	[Deg91t]	O	Mixed valence

Table 30
Ligand 1s X-ray absorption spectra for chromium compounds

Compound	Ref.	Element	Remarks
Cr_2O_3	[Gru83]	O	Molecular orbitals
CrSi	[Wey91]	Si	DOS from LSD
$CrSi_2$	[Van90, Wey91]	Si	DOS from LSD

related to the limitations of the basis set and hence limitations of the energy range.

8.4.2. The "pre-edge" region

The "pre-edge" region of the transition metal 1s edges has led to a number of debates regarding the quadrupole and/or dipole nature and possible excitonic effects. The "pre-edge" region is related to transitions to the 3d bands. Both direct 1s → 3d quadrupole transitions and dipole transitions to p character hybridized with the 3d band are possible. For the quadrupole transitions the matrix elements are only about 1% of the dipole transition, but the amount of the 3d character in the 3d band is far larger than the p character. This can make, depending on the particular system, the contributions of quadrupole and dipole transitions equivalent in intensity. A direct manner to check the nature of the transitions is to measure the polarization dependence which is different for quadrupole and dipole (as discussed in Section 5.1). This has been checked by Hahn et al. for $CuCl_4^{2-}$ [Hah82] and by Brouder et al. for (the first peak of) TiO_2 [Bru90b]. In both cases a clear and dominant quadrupole contribution could be proven. Recently Yamazaki et al. showed that for the X-MCD spectrum of the "pre-edge" in holmium–iron–garnet

Table 31
Ligand 1s X-ray absorption spectra for manganese compounds

Compound	Ref.	Element	Remarks
$Mn_2(CO)_{10}$	[Hit89a]	C	Organometallic molecules
MnF_2	[Nak88]	F	
MnO	[Nak87]	O	
MnO_2	[Deg89]	O	
MnSi	[Wey91]	Si	
$La_{1-x}Sr_xMnO_3$	[Abb92a]	O	Mixed valence
$LiMnO_2$	[Deg91t]	O	

Table 32
Ligand 1s X-ray absorption spectra for iron compounds

Compound	Ref.	Element	Remarks
$CuFeS_2$	[Sai91]	S	MS
Fe_4B	[Bla89]	B	
FeF_2	[Nak88]	F	
FeMo-protein	[Hem91]	S	Oxidation–reduction
FeO	[Bro86a, Gru83]	O	
	[Col91, Nak87]	O	
α-Fe_2O_3	[Col91, Bro86a]	O	
γ-Fe_2O_3	[Col91]	O	
Fe_3O_4	[Col91]	O	
Fe_2SiO_4	[Bro86a]	O	
$La_{1-x}Sr_xFeO_3$	[Abb93b]	O	Mixed valence

the quadrupole contribution is less than 0.1% [Yaz93].

The case of TiO_2 in its rutile crystal structure has been strongly debated. There are three pre-peaks and the traditional interpretation has been to subscribe the second and third peaks to, respectively, the t_{2g}-like and e_g-like states and the first peak to some kind of exciton. Uozumi et al. [Uoz92] described the "pre-edge" region as a superposition of a quadrupole transition to 3d states and a dipole transition to p states. Both are split by the crystal field and the two doublets are shifted with respect to each other due to the stronger interaction with the 1s core hole with the states of 3d nature. Both the crystal field splitting and the difference in core hole coupling are (assumed to be) about 2.5 eV. The result is three peaks, the first of pure quadrupole nature, the second a mixture and the third a pure dipole peak. This interpretation explains the quadrupole polarization dependence of the first peak. The second peak has a smaller but still considerable quadrupole polarization dependence in the theoretical simulation [Uoz92], but it is almost completely absent in experiment [Bru90b]. Czyżyk also performed a simulation of the "pre-edge" peaks using the projected density of states of a final state band structure calculation [Czy93]. This calculation yields an excitonic peak which is completely dominated by 3d character followed by the t_{2g} and e_g peaks which contain a mixture of d and p character. Including the matrix elements one obtains a first peak which is dominated by quadrupole transitions, though with a dipole contribution of about 25%. The second peak is dominated by dipole transitions, with less than 10% quadrupole and the third peak (and the rest of the spectrum) is almost pure dipole in nature. This result explains better the quadrupole polarization dependence of the first peak and its absence in the second peak. The three-peaked structure has also been reproduced by a ground state LSD calculation [Rui91], which is not compatible with the analysis as given above.

The intensity of the "pre-edge" region is much larger for compounds in which the metal site has tetrahedral symmetry than for (distorted) octahedral systems [Bia85, Lyt88]. In tetrahedral symmetry the local mixing of p and d nature is symmetry allowed, while for a system with inversion symmetry such as octahedral symmetry it is

Table 33
Ligand 1s X-ray absorption spectra for cobalt compounds

Compound	Ref.	Element	Remarks
CoF_2	[Nak88]	F	
CoO	[Szy90]	O	
Co_3O_4	[Szy90]	O	
$Co_{1-x}Li_xO$	[Deg93b, Vel91a]	O	
CoSi	[Wey91]	Si	LSD (core hole)
$CoSi_2$	[Van90, Wey91]	Si	
$LaCoO_3$	[Abb93b]	O	Phase transition
$LiCoO_2$	[Czy92]	O	LSD
$ZnCo_2O_4$	[Szy90]		

Table 34
Ligand 1s X-ray absorption spectra for nickel compounds

Compound	Ref.	Element	Remarks
$LiNiO_2$	[Vel92]	O	Multiplet effects
$Ni(Cp)_2$	[Hit89a]	C	(Cp = cyclopentadiene)
NiF_2	[Nak88]	F	
NiO	[Gru83, Nak87]	O	
	[Dav86b, Vel92]	O	
Ni_2SiO_4	[Bro86a]	O	
NiSi	[Wey91]	Si	DOS from LSD
$NiSi_2$	[Van90, Wey91]	Si	DOS from LSD

"forbidden". This rule is relaxed in the solid and if the density of states is calculated with band structure methods one finds small admixture of p states into the 3d band, as shown for cubic $SrTiO_3$ [Deg91t]. However this admixture is far smaller than for tetrahedral systems which explains the small "pre-edge".

If an octahedral metal site is distorted then, depending on the particular distortion taking place, in general more p character will be mixed into the 3d band. The result is that a distortion of the octahedron will show up as an increased intensity of the "pre-edge" peak(s). That this is indeed the case has been shown by Waychunas for a series of minerals [Way87]; a roughly linear relationship between the bond angle variance (a measure of the distortion) and the "pre-edge" intensity relative to the "step" was demonstrated.

8.4.3. *"Multichannel" effects*

In their description of the copper 1s edge spectrum of $CuCl_2$ Bair and Goddard [Bai80] introduce the possibility of a "shake-down" satellite structure. Within the framework of the short-range (Anderson impurity) models used for the interpretation of 2p XPS and 2p XAS this process can be related to a charge transfer satellite. Copper is divalent and its ground state is written as $3d^9 + 3d^{10}\underline{L}$. Because of the 1s core hole in the final state the ordering of the ionic configurations is reversed in the final state similar to the case of 2p XPS. This results in two final states ($1s^1 3d^9$ and $1s^1 3d^{10}\underline{L}$). The 1s X-ray absorption spectrum is then assumed to be a multiplication of this double peak structure with the "projected unoccupied states". That is if the two peaks are separated by 7 eV and have an intensity ratio of 1:2 then the 1s XAS spectrum is a superposition of the (projected empty) DOS and this DOS shifted over 7 eV with half the intensity. If one of the two peaks completely dominates (or if the energy difference is small) these "multichannel" effects will not appear. This "multichannel" interpretation is used to interpret the characteristic double structure in the copper 1s spectra of the divalent copper oxides such as La_2CuO_4 [Tol92, Tol93]. This double structure is absent in the structurally related Pr_2NiO_4.

8.4.4. *The $1/R^2$ rule*

Under certain conditions the peak positions of the XANES spectrum can be correlated with the nearest neighbour distances. This phenomenon is known as the $1/R^2$ rule which states that the $\Delta E/R^2$ is constant. This relation between $1/R^2$ and the energy position has often been encountered, for example by Müller et al. [Mul82]. Natoli

Table 35
Ligand 1s X-ray absorption spectra for copper compounds

Compound	Ref.	Element	Remarks
CuF_2	[Nak88]	F	
$CuFeS_2$	[Sai91]	S	MS
$CuGaS_2$	[Sai91]	S	MS
CuO	[Gru83, Nak87]	O	LSD
	[Gri89a]	O	LSD
$CuAl_2O_4$	[Szy90]	O	
$La_{2-x}Sr_xCuO_4$	[Che92a]	O	Linear dichroism
$Ba_2Cu_3O_{7-x}$	[Kui88]	O	

Table 36
Titanium 1s X-ray absorption spectra

Compound	Ref.	Remarks
Ti	[Gru83]	
Ti in B	[Won89]	3d Metals in boron
TiC	[Baz83]	
$TiCl_4$	[Kue90]	
TiFe	[Baz83]	
TiO	[Nor85]	MS
TiO_2	[Baz80, Gru83]	Molecular orbitals
	[Mot90]	Mineral
	[Dur90]	Temperature dependence
	[Bru90b]	Temp. + pol. dependence
	[Pou90]	Polarization dependence
	[Rui91]	MS; 3 prepeaks in ground state
	[Uoz92]	Charge transfer model; quadrupole transition
	[Czy93]	LSD plus core hole; quadrupole transition
Ti_2O_3	[Way87]	Trivalent
$Ti^{4+}[O_4)$	[Bia85]	Tetrahedral site
$BaTiO_3$	[Baz80, Baz83]	
Ba_2TiO_4	[Mot90]	Tetrahedral site
Kaersutite	[Way87]	Series of minerals
$LaTiO_3$	[Kna82]	
$LiTi_2O_4$	[Dur90]	
$SrTiO_3$	[Baz80]	
	[Fis90b]	High pressure

[Nat83] justified the use of this rule for non-atomic resonances, that is resonances with a small variation in phase shifts (related to the lattice parameter). ΔE refers to the energy difference between the peak position and the point of "zero kinetic energy" which has the problem that it is not well defined within an experimental spectrum.

This $1/R^2$ rule has been used successfully by Bianconi [Bia83b], Sette et al. [Set84] and Stöhr et al. [Sto84] for the determination of the bond length of (adsorbed) small molecules. The rule can be used as a measure to directly relate the peak positions to the distances around the absorbing atom. It is used as such for example for NiO and Cu by Lytle et al. [Lyt88]. Because copper in its divalent oxides contains large Jahn–Teller distortions there exist two different nearest neighbour oxygen–copper distances which for X-ray

Table 37
Vanadium 1s X-ray absorption spectra

Compound	Ref.	Remarks
V in B	[Won89]	3d Metals in boron
VO	[Kut84, Won84]	
	[Lyt88]	
VO_x	[Kut84]	Effects of vacancies
V_2O_3	[Won84]	Series of vanadium compounds
V_4O_7	[Won84]	
VO_2	[Bia82a, Won84]	
V_2O_5	[Bia82a, Won84]	
	[Sti89]	Polarization dependence
VN	[Won84]	
VSi_2	[Won84]	
$V^{5+}(H_2O)$	[Bia85]	Tetrahedral site
V (porphyrin)	[Rui86]	

Table 38
Chromium 1s X-ray absorption spectra

Compound	Ref.	Remarks
Cr	[Gru83, Kit86]	
Cr_2O_3	[Gru83]	
K_2CrO_4	[Bia91]	Multielectron excitations
	[Kut80]	
$LaCrO_3$	[Kna82]	

Table 39
Manganese 1s X-ray absorption spectra

Compound	Ref.	Remarks
Mn	[Bel80]	
Mn (atom)	[Arp91]	Atomic manganese
Mn in CaF_2	[Bak92]	
Mn $(acac)_3$	[Cat86a]	Coordination complexes
MnF_2	[Bak92]	
MnF_3	[Bak92]	
Mn_2CrO_4	[Cal86]	
MnO	[Bel80, Nor85]	
	[Kna82, Lyt88]	
	[Ham93]	Spin-polarized; reduced life-time
Mn_2O_3	[Bel80]	
MnO_2	[Bel80]	
$MnHPO_4$	[Bel80]	
Mn-photosystem	[Kus91]	Pre-edge structure
$KMnO_4$	[Bel80]	
	[Bia91]	Multielectron excitations
$KMnF_3$	[Kit90, Shu76]	
$LaMnO_3$	[Kna82]	
TTF $(MnCl_4)_{0.28}$	[Bri92]	(TTF is tetrathiafulvalene)

absorption spectra can be disentangled by the use of polarization dependent measurements. This has been shown nicely by Tolentino and co-workers [Tol92, Tol93] for a series of copper oxides. They included a measurement of Nd_2CuO_4 and because the axial oxygens are "at infinite distance" in this compound the point of "zero energy" has been chosen at the position of the first peak in the Nd_2CuO_4 spectrum [Tol92] and it is found that $\Delta E/R^2$ is indeed constant.

In a recent paper of Kizler [Kiz92a] the $1/R^2$ rule is re-examined with a detailed comparison to multiple scattering calculations and it is claimed that the rule is "disproved for bulk materials"; that is, it is shown that the rule cannot be used for shells other than the first (and second) nearest neighbours. Thus an extensive use as for example in [Lyt88] is disproved, but not its use for the nearest neighbours as for example in [Tol92]. This warning concerning the (limited) use of the rule has also been given in Natoli's paper [Nat83].

8.5. *Overview of the ligand 1s spectra*

A partial overview is given of a choice of published ligand 1s spectra of 3d transition metal compounds (Tables 28–35). The emphasis is given to oxides and the list is far from complete particularly for chlorides and sulphides. Also more application-oriented studies on catalysis, earth sciences and organic complexes are only partially included. The ligand spectra are

Table 40
Iron 1s X-ray absorption spectra of iron compounds

Compound	Ref.	Remarks
Fe	[Buf87, Gru83]	
	[Kit86]	MS
$FeAl_2O_4$	[Jac91, Kna82]	
	[Bro86b]	
Fe_2B	[Kiz89]	
Fe_4B	[Kiz88, Kiz91]	
$FeCr_2O_4$	[Cal86, Pei83]	
$Fe(Cp)_2$	[Iwa86]	(Cp is cyclopentadiene)
Fe/Gd	[Ito93]	X-MCD (multilayers)
$Fe_5Ho_3O_{12}$	[Yaz93]	X-MCD
FeO	[Chu86, Gru83]	
	[Gar87, Nor85]	MS
	[Lyt88, Mot91]	
$Fe_{0.5}Mg_{0.5}O$	[Kna82]	
$Fe_{0.05}Mg_{0.95}O$	[Way90]	
α-Fe_2O_3	[Chu86, Gru83]	
Fe_3O_4	[Chu86, Gar87]	
$Fe_{1-x}Ni_x$	[Sak93]	X-MCD
FePC	[Fra86]	(PC is phthalocyanine)
Fe_4(RE)	[Kob93]	X-MCD (where RE is Sm, Gd, Tb, Dy)
FeS_2	[Pei83]	
Fe_3Si	[Bud89]	(Doped with V, Mn and Co)
Fe_2SiO_4	[Cal86]	(Olivine)
$FeW_{1-x}Nb_xO_4$	[Gar87]	
Fe_2SiO_4	[Jac91]	High temperature
$Fe(phen)_2(NCS)_2$	[Cat86b]	Complexes
Fe(porphyrin)	[Ver86]	
	[Pen91]	Pol. dependent pre-edges
Fe (haemoglobin)	[Bia83a]	
Gillespite	[Way90]	Polarization dependence
$KFeF_3$	[Kit90, Shu76]	
$K_3Fe(CN)_6$	[Bia82b]	(also $K_4Fe(CN)_6$)
$K_4[Fe_2(CN)_{10}]$	[Edw89]	
$LaFeO_3$	[Buf87, Kna82]	
$LiFeO_2$	[Way83]	
$Na_2FeSi_3O_8$	[Bro86b]	Fe in silicates
$Ni_xFeCr_{2-x}O_4$	[Len86]	
Orthopyroxene	[Mot91]	
$SrFeO_3$	[Buf87]	
Staurolite	[Pei83]	Pre-edge

Table 41
Cobalt 1s X-ray absorption spectra

Compound	Ref.	Remarks
Co	[Buf87, Len88]	
$CoAl_2O_4$	[Kna82]	
Co_2CrO_4	[Cal86]	
CoO	[Len88, Nor85]	
	[Kna82]	
Co_3O_4	[Len88]	
$CoRh_2O_4$	[Len88]	
$CuCoO_2$	[Len88]	
$LaCoO_3$	[Buf87, Kna82]	
	[Kag91]	Temperature dependence
$La_{0.5}Sr_{0.5}CoO_3$	[Kag91]	Temperature dependence
$La_2Li_{0.5}Co_{0.5}O_6$	[Buf87]	
$KCoF_3$	[Kit90, Shu76]	
$Co(imad)_2$	[Des83]	
$TTF(CoCl_4)_{0.28}$	[Bri92]	(TTF = tetrathiafulvalene)

tabulated per metal ion, starting with titanium and ending with copper. Most studies on the high T_c superconducting copper oxides have not been included.

8.6. Overview of the metal 1s spectra

A partial overview is given on the metal 1s X-ray absorption spectra (Tables 36–43). In this context hard X-rays are often denoted as X-ray absorption near edge structure (XANES), to distinguish them from the EXAFS analysis. Emphasis is given to recent papers on simple, mostly inorganic, compounds and papers which concentrate on theory.

Table 42
Nickel 1s X-ray absorption spectra

Compound	Ref.	Remarks
Ni	[Gru83]	
Ni_4B	[Kiz88]	
$NiCr_2O_4$	[Len86, Cal86]	
NiF_2	[Len86]	
$NiFe_{2-x}Cr_xO_4$	[Len86]	
$Ni(N_4)$	[Sco89]	Ni^{II} metalloenzymes
NiO	[Gru83, Nor85]	
	[Kna82, Len86]	
Ni(PC)	[Loo89]	MS, (phthalocyanines)
Ni(urease)	[Has83]	
$KNiF_3$	[Shu76, Kit90]	
La_2NiO_4	[Tan93]	Hole doping

Table 43
Copper 1s X-ray absorption spectra

Compound	Ref.	Remarks
Cu	[Gru83]	
Cu (atom)	[Arp91]	Atomic copper
Cu in B	[Won89]	3d Metals in boron
CuO	[Gru83]	Molecular orbitals
	[Kau87]	
Cu_2O	[Nor85]	MS
CuCl	[Haz90]	
$CuCl_4^{2-}$	[Hah82]	Quadrupole transition
CuI	[Haz90]	
$CuTiO_3$	[Lyt88]	$1/R^2$ rule
Cu(II) CN-SOD	[Str91]	(SOD is superoxide dismutase)
$La_{2-x}Sr_xCuO_4$	[Als90]	Bibliography 1987–1989
	[Tan93]	
$La_2CuO_{4-\delta}$	[Oya89]	Polarization dependence
	[Tol92]	Polarization dependence
$YBa_2Cu_3O_7$	[Lyt88]	$1/R^2$ rule
	[Als90]	Bibliography 1987–1989

A recent review concentrating on the structural aspects of XANES spectra is given by Kizler [Kiz92b]. A review focusing on linear polarization dependence is given by Brouder [Bru90a]. Most studies on the high T_c superconducting copper oxides have not been included.

9. Concluding remarks and outlook

9.1. The metal 2p X-ray absorption spectra

The metal 2p X-ray absorption spectra are described with short range Hamiltonians such as the Anderson impurity model, including multiplets. Because in the final state the Coulomb repulsions U_{dd} and U_{cd} largely cancel, the ligand field multiplet model is appropriate for ionic compounds. The ligand field multiplet model has the advantage of its simplicity and the absence of adjustable parameters apart from an effective cubic ligand field strength.

9.2. The ligand 1s X-ray absorption spectra

The 1s X-ray absorption spectra do show large similarities with single particle calculations of the

empty states. For these calculations use can be made of band structure methods such as LAPW, LMTO, ASW and LSW or of multiple scattering methods. If the empty density of states is calculated with a self-consistent potential and large enough basis sets, accurate agreement with the X-ray absorption spectra is found. The agreement is improved if the core hole potential is included, while it turns out that matrix elements can, to good approximation, be taken as energy independent. Small effects of multiplets are expected in the part of the spectrum related to the 3d band, but the quantitative results available are not conclusive.

9.3. The valency and symmetry of the metal ions

2p X-ray absorption is an excellent means for the determination of the valency and the symmetry (spin-state) of 3d transition metal ions in compounds and complexes. Due to the "fingerprint" provided by the characteristic final state multiplet structure the valency and spin state can be determined directly and conclusively. More detailed studies, including linear and circular dichroism, can provide additional information on the 3d spin–orbit coupling, lower symmetries, the magnetic ordering and the orbital polarization.

9.4. The electronic configuration

With regard to the details of the electronic configuration 2p X-ray absorption is not the ideal tool, mainly because of the insensitivity of some of the parameters of the model Hamiltonians to the simulations of the spectral shape. In this respect 2p XPS and valence band photoemission are better tools in order to determine the parameter values in the various short range models presently in use.

9.5. The short range model Hamiltonians

Much is still unclear for short range model Hamiltonians as used for core spectroscopies. There are variations and uncertainties in the Hamiltonian itself, the values of the parameters, final state effects and multiplet effects.

Important Hamiltonians presently in use include the Hubbard model (one band with Coulomb repulsion), the Anderson impurity model (two bands, one with repulsion), the Kimball–Falicov model (adding interband repulsion) and the three-band Hubbard model (adding repulsion also in the second band). Additionally these models can be made to interact with the lattice.

The values of the parameters used in these models are normally determined empirically from the simulation of various experiments, or alternatively they are determined from ab initio electronic structure models. In any case the values are model dependent and in that sense "effective" and there is a particular uncertainty with respect to their values.

With respect to the simulation of core spectroscopies there is the problem of the values of the parameters in the final state. A core excitation is expected to modify the electronic structure and as a consequence the effective parameters used for the ground state can (and will) be modified. The way in which this happens can largely be predicted, but many questions still remain.

Multiplet effects play a role in the ground state of 3d systems, but this role is enormously magnified if a 2p core hole is created, due to its strong couplings with the partly filled 3d band. These multiplet effects, or in other words the higher-order terms of the Coulomb repulsions and exchange interactions, play an important role in 2p XPS and particularly in 2p XAS.

9.6. The use of X-ray absorption for the study of materials

Due to the experimental progress in synchrotron radiation, the resolution of soft X-ray monochromators and detection techniques, (soft) X-ray absorption has become an important new tool for the study of materials in basically all fields which study 3d systems. X-ray absorption is element

selective and sensitive to "impurities", which includes the role of metal centres in biological systems, catalysis, mineralogy, the search for new magnetic and electronic materials (including superconductors), etc. The analysis with the ligand field multiplet model provides a wealth of information on metal centres (see above), which can "compete", or better assist, the information from for example optical (laser) spectroscopies and resonance experiments.

Acknowledgements

This review is dedicated to the memory of Professor John C. Fuggle. For discussions and advice on particular points I should like to thank Ferdi Aryasetiawan, Christian Brouder, Chien-Te Chen, Steve Cramer, Marek Czyżyk, Henk Eskes, Alain Fontaine, Olle Gunnarsson, Volker Heine, John Inglesfield, Ove Jepsen, Pieter Kuiper, Sasha Liechtenstein, John Michiels, Maurizio Sacchi, Gisela Schütz, Hao Tjeng, Jan van Elp and Jan Vogel. Special thanks to Miguel Abbate, George Sawatzky and Theo Thole. This work was partially supported by the European Community Human Capital and Mobility program.

I thank M. Abbate, V. Anisimov, M. Czyżyk, J. Goedkoop, J. Fink, A. Kotani, K. Okada, Ph. Sainctavit, L. Soriano, S. Sugano, Z. Szotek, K. Terakura, G. van der Laan, P.J. Weiss and also the Journal of Electron Spectroscopy, the Journal of Physics Condensed Matter, the Journal of the Physical Society of Japan, Physica B, Physical Review B, Physics and Chemistry of Minerals, and Surface and Interface Analysis for permission to reproduce their figures.

References

[Abb90] M. Abbate, M. Sacchi, J.J. Wnuk, W.M. Schreurs, Y.S. Wang, R. Lof and J.C. Fuggle, Phys. Rev. B, 42 (1990) 7914.

[Abb91a] M. Abbate, F.M.F. de Groot, J.C. Fuggle, Y.J. Ma, C.T. Chen, F. Sette, A. Fujimori, Y. Ueda and K. Kosuge, Phys. Rev. B, 43 (1991) 7263.

[Abb91b] M. Abbate, F.M.F. de Groot, J.C. Fuggle, A. Fujimori, Y. Tokura, Y. Fujishima, O. Strebel, M. Domke, G. Kaindl, J. van Elp, B.T. Thole, G.A. Sawatzky, M. Sacchi and N. Tsuda, Phys. Rev. B, 44 (1991) 5419.

[Abb92a] M. Abbate, F.M.F. de Groot, J.C. Fuggle, A. Fujimori, O. Strebel, F. Lopez, M. Domke, G. Kaindl, B.T. Thole, G.A. Sawatzky, M. Takano, Y. Takeda, H. Eisaki and S. Uchida, Phys. Rev. B, 46 (1992) 4511.

[Abb92b] M. Abbate, J.B. Goedkoop, F.M.F. de Groot, M. Grioni, J.C. Fuggle, S. Hoffman, H. Petersen and M. Sacchi, Surf. Interface Anal., 18 (1992) 65.

[Abb93a] M. Abbate, H. Pen, M.T. Czyżyk, F.M.F. de Groot, J.C. Fuggle, Y.J. Ma, C.T. Chen, F. Sette, A. Fujimori, Y. Ueda and K. Kosuge, J. Electron Spectrosc. Relat. Phenom., 62 (1993) 185.

[Abb93b] M. Abbate, J.C. Fuggle, A. Fujimori, L.H. Tjeng, C.T. Chen, R. Potze, G.A. Sawatzky, H. Eisaki and S. Uchida, Phys. Rev. B, 47 (1993) 16124.

[Ack84] B. Ackermann, R. Feder and E. Tamura, J. Phys. F, 14 (1984) L173.

[Ahl84] R. Ahlrichs and P. Scharf, Adv. Chem. Phys., 67 (1987) 501.

[Ald93] D. Alders, unpublished results.

[Alm83] C.O. Almbladh and L. Hedin, Beyond the one-electron model: many-body effects in atoms, molecules and solids, in E.E. Koch (Ed.), Handbook on Synchrotron Radiation, Vol. 1A, North Holland, Amsterdam, 1983, p. 607.

[Als90] F. Al-Shamma and J.C. Fuggle, Physica C, 169 (1990) 325.

[And75] O.K. Andersen, Phys. Rev. B, 12 (1975) 3060.

[And79] O.K. Andersen, H.L. Skriver, H. Nohl and B. Johansson, Pure Appl. Chem., 52 (1979) 93.

[And84] O.K. Andersen and O. Jepsen, Phys. Rev. Lett., 53 (1984) 2571.

[And85] O.K. Andersen, O. Jepsen and D. Glötzel, in F. Bassani, F. Fumi and M. Tosi (Eds.), Highlights of Condensed Matter Theory, North Holland, Amsterdam, 1985, pp. 59 ff.

[And87] O.K. Andersen, O. Jepsen and M. Sob, Linearized band structure methods, in M. Yussouf (Ed.), Electronic Band Structure and its Applications, Springer Lecture Notes, 1987.

[Ani91a] V.I. Anisimov, J. Zaanen and O.K. Andersen, Phys. Rev. B, 44 (1991) 943.

[Ani91b] V.I. Anisimov and O. Gunnarsson, Phys. Rev. B, 43 (1991) 7570.

[Ani92a] V.I. Anisimov, M.A. Korotin, J. Zaanen and O.K. Andersen, Phys. Rev. Lett., 68 (1992) 345.

[Ano61] P.W. Anderson, Phys. Rev., 124 (1961) 41.

[Arp91] U. Arp, G. Materlik, M. Meyer, M. Richter and B. Sonntag, in S.S. Hasnain (Ed.), X-ray Absorption Fine Structure, Ellis Horwood, Chichester, 1991, p. 44.

[Ary92] F. Aryasetiawan, Phys. Rev. B, 46 (1992) 13051.

[Ary93] F. Aryasetiawan, unpublished results.

[Asa75] S. Asada, C. Satako and S. Sugano, J. Phys. Soc. Jpn., 37 (1975) 855.
[Asa76] S. Asada and S. Sugano, J. Phys. Soc., Jpn., 41 (1976) 1291.
[Bag73] P.S. Bagus, A.J. Freeman and F. Sasaki, Phys. Rev. Lett., 30 (1973) 851.
[Bag89] P. Bagno, O. Jepsen and O. Gunnarsson, Phys. Rev. B, 40 (1989) 1997.
[Bai80] R.A. Bair and W.A. Goddard III, Phys. Rev. B, 22 (1980) 2767.
[Bak92] J.H. Barkyoumb and A.N. Mansour, Phys. Rev. B, 46 (1992) 8768.
[Bal62] C.J. Ballhausen, Introduction to Ligand Field Theory, McGraw-Hill, New York, 1962
[Bar83] J. Barth, F. Gerken and C. Kunz, Phys. Rev. B, 28 (1983) 3608.
[Bas83] F. Bassani and M. Altarelli, Interaction of radiation with condensed matter, in E.E. Koch (Ed.), Handbook on Synchrotron Radiation, Vol. 1A, North Holland, Amsterdam, 1983, p. 463.
[Bau91] F. Baudelet, E. Dartyge, A. Fontaine, C. Brouder, G. Krill, J.P. Kappler and M. Piecuch, Phys. Rev. B, 43 (1991) 5857.
[Baz80] A. Balzarotti, F. Comin, L. Incoccia, M. Piacentini, S. Mobilio and A. Savoia, Solid State Commun., 35 (1980) 145.
[Baz83] A. Balzarotti, in A. Bianconi, L. Incoccia and S. Stipcich (Eds.), EXAFS and Near Edge Structure, Springer-Verlag, Berlin 1983, p. 135.
[Bec88] A.D. Becke, Phys. Rev. A, 38 (1988) 3098.
[Bel80] M. Belli, A. Scafati, A. Bianconi, S. Mobilio, L. Palladino, A. Reale and E. Burattini, Solid State Commun., 35 (1980) 355.
[Ben93] M. Benfatto, Z.Y. Wu and C.R. Natoli, Jpn. J. Appl. Phys., 32 (1993) 590.
[Ber87] S. Bernstorff et al., Phys. Scr., 36 (1987) 15.
[Bia82a] A. Bianconi, Phys. Rev. B, 26 (1982) 2741.
[Bia82b] A. Bianconi, M. Dell' Ariccia, P.J. Durham and J.B. Pendry, Phys. Rev. B, 26 (1982) 6502.
[Bia83a] A. Bianconi, in A. Bianconi, L. Incoccia and S. Stipcich (Eds.), EXAFS and Near Edge Structure, Springer-Verlag, Berlin, 1983, p. 118.
[Bia83b] A. Bianconi, M. Dell'Ariccia, A. Gargano and C.R. Natoli, in A. Bianconi, L. Incoccia and S. Stipcich (Eds.), EXAFS and Near Edge Structure, Springer-Verlag, Berlin, 1983, p. 57.
[Bia85] A. Bianconi, E. Fritsch, G. Calas and J. Petiau, Phys. Rev. B, 32 (1985) 4292.
[Bia88] A. Bianconi, M. De Santis, A.M. Flank, A. Fontaine, P. Lagarde, A. Marcelli, H. Katayama-Yoshida and A. Kotani, Phys. Rev. B, 38 (1988) 7196.
[Bia91] A. Bianconi, J. Garcia, M. Benfatto, A. Marcelli, C.R. Natoli and M.F. Ruiz-Lopez, Phys. Rev. B, 43 (1991) 6885.
[Bia92] A. Bianconi, C. Li, S. Della Longa and M. Pompa, Phys. Rev. B, 45 (1992) 4989.
[Bla89] W. Blau, R. Dudde and H. Petersen, Solid State Commun., 69 (1989) 147.
[Boc92a] A.E. Bocquet, A. Fujimorui, T. Mizokawa, T. Saitoh, H. Namatame, S. Suga, N. Kimizuka, Y. Takeda and M. Takano, Phys. Rev. B, 45 (1992) 1561.
[Boc92b] A.E. Bocquet, T. Mizokawa, T. Saitoh, H. Namatame and A. Fujimori, Phys. Rev. B, 46 (1992) 3771.
[Boe84] D.K.G. de Boer, C. Haas and G.A. Sawatzky, Phys. Rev. B, 29 (1984) 4401.
[Bog57] P.F. Bongers, Ph.D. Thesis, University of Leiden, 1957.
[Bog75] P.F. Bongers, in C.J.M. Rooymans and A. Rabenau (Eds.), Crystal Structure and Chemical Bonding in Inorganic Chemistry, Elsevier, Amsterdam, 1975, Chap. 4.
[Bon66] C. Bonnele, Ann. Phys., 1 (1966) 439.
[Bon86] D. Bonnin, J. Phys. (Paris) C, 8 (1986) 623.
[Bor92] A. Borg, P.L. King, P. Pianetta, I. Lindau, D.B. Mitzi, A. Kapitulnik, A.V. Soldatov, S. Della Longa and A. Bianconi, Phys. Rev. B, 46 (1992) 8487.
[Bri92] V. Briois, R.M. Lequan, M. Lequan, C. Cartier, G. van der Laan, A. Michalowicz and M. Verdaguer, Chem. Mater., 4 (1992) 484.
[Bro78] F.C. Brown, R.Z. Bachrach and N. Lien, Nucl. Instrum. Methods, 152 (1978) 73.
[Bro86a] G.E. Brown Jr., G.A. Waychunas, J. Stohr and F. Sette, J. Phys. (Paris) C, 8 (1986) 685.
[Bro86b] G.E. Brown Jr., G.A. Waychunas, C.W. Ponader, W.E. Jackson and D.A. Mckeown, J. Phys. (Paris) C, 8 (1986) 661.
[Bru90a] C. Brouder, J. Phys. C, 2 (1990) 701.
[Bru90b] C. Brouder, J.P. Kappler and E. Beaurepaire, in A. Balerna, E. Bernieri and S. Mobilio (Eds.), Proc. 2nd European Conference on Progress in X-ray Synchrotron Radiation Research, Rome, November 1989, SIF, Bologna, 1990, p. 19.
[Bru91] C. Brouder and M. Hikam, Phys. Rev. B, 43 (1991) 3809.
[Bry87] R. Brydson, B.G. Williams, W. Engel, H. Sauer, E. Zeitler and J.M. Thomas, Solid State Commun., 64 (1987) 609.
[Bry89] R. Brydson, H. Sauer, W. Engel, J.M. Thomas, E. Zeitler, N. Kosugi and H. Kuroda, J. Phys. Condensed Matter, 1 (1989) 797.
[Bry92] R. Brydson, H. Sauer, W. Engel and F. Hofer, J. Phys. Condensed Matter, 4 (1992) 3429.
[Bud89] J.I. Budnick, Z. Tan and D.M. Pease, Physica B, 158 (1989) 31.
[Buf87] B. Buffat and M.H. Tuilier, Solid State Commun., 64 (1987) 401.
[But81] P.H. Butler, Point Group Symmetry Applications: Methods and Tables, Plenum Press, New York, 1981.
[Cal86] G. Calas, J. Petiau and A. Manceau, Phys. (Paris) C, 8 (1986) 813.
[Car90] P. Carra and M. Altarelli, Phys. Rev. Lett., 64 (1990) 1286.

[Car91] P. Carra, B.N. Harmon, B.T. Thole, M. Altarelli and G.A. Sawatzky, Phys. Rev. Lett., 66 (1991) 2495.

[Car92] P. Carra, Synchrotron Radiat. News, 5 (1992) 6:21.

[Car93] P. Carra, B.T. Thole, M. Altarelli and X. Wang, Phys. Rev. Lett., 70 (1993) 694.

[Cat86a] C. Cartier, M. Verdaguer, S. Menage, J.J. Girerd, J.P. Tuchagues and B. Mabad, J. Phys. (Paris) C, 8 (1986) 623.

[Cat86b] C. Cartier, P. Thuery, M. Verdaguer, J. Zarembowitch and A. Michailowicz, J. Phys. (Paris) C, 8 (1986) 563.

[Cat90] C. Cartier, M. Verdaguer, A.M. Flank, P. Lagarde, F. Baudelet, J. Darriet, A. Tressaud and A. Lelirzin, in A. Balerna, E. Bernieri and S. Mobilio (Eds.), Proc. 2nd European Conference on Progress in X-ray Synchrotron Radiation Research, Rome, November 1989, SIF, Bologna, 1990, p. 907.

[Cat91] C. Cartier and A.M. Flank, in S.S. Hasnain (Ed.), X-ray Absorption Fine Structure, Ellis Horwood, Chichester, 1991, p. 659.

[Cat92] C. Cartier, P. Rudolf, A.M. Flank and C.T. Chen, J. Phys. Chem., 96 (1992) 6196.

[Cat93] C. Cartier dit Moulin, A.M. Flank, P. Rudolf and C.T. Chen, Jpn. J. Appl. Phys., 32 (1993) 308.

[Che87] C.T. Chen, Nucl. Instrum. Methods, 256 (1987) 595.

[Che89] C.T. Chen and F. Sette, Rev. Sci. Instrum., 60 (1989) 1616.

[Che90a] C.T. Chen and F. Sette, Phys. Scr. T, 31 (1990) 119.

[Che90b] C.T. Chen, F. Sette and N.V. Smith, Appl. Opt., 29 (1990) 4235.

[Che91] C.T. Chen, N.V. Smith and F. Sette, Phys. Rev. B, 43 (1991) 6785.

[Che92a] C.T. Chen, L.H. Tjeng, J. Kwo, H.L. Kao, P. Rudolf, F. Sette and R.M. Fleming, Phys. Rev. Lett., 68 (1992) 2543.

[Che92b] C.T. Chen, Rev. Sci. Instrum., 63 (1992) 1223.

[Che93] C.T. Chen, Jpn. J. Appl. Phys., 32 (1993) 155.

[Cho85] M. Choi, D.M. Pease, W.A. Hines, G.H. Hayes, J.I. Budnick, S.M. Heald, R. Hasegawa and H.E. Schone, Phys. Rev. B, 32 (1985) 7670.

[Chu86] S.H. Chou, J. Guo and D.E. Ellis, Phys. Rev. B, 34 (1986) 12.

[Cit76] P.H. Citrin, P. Eisenberger and B.M. Kincaid, Phys. Rev. Lett., 36 (1976) 1346.

[Col91] C. Colliex, T. Manoubi and C. Ortiz, Phys. Rev. B, 44 (1991) 11402.

[Con35] E.U. Condon and G.H. Shortley, The Theory of Atomic Spectra, University Press, Cambridge, UK, 1935.

[Cow81] R.D. Cowan, The Theory of Atomic Structure and Spectra, University of California Press, Berkeley, 1981, p. 307.

[Cra88] S.P. Cramer, O. Tench and G.N. George, Nucl. Instrum. Methods A, 266 (1988) 586.

[Cra91a] S.P. Cramer, H. Kraner, S.J. George, L. Rogers, S. Rescia, V. Radeka, M. Yocum, J. Coloresi, O. Tench and O.C. Mullins, in S.S. Hasnain (Ed.), X-ray Absorption Fine Structure, Ellis Horwood, Chichester, 1991, p. 640.

[Cra91b] S.P. Cramer, F.M.F. de Groot, Y. Ma, C.T. Chen, F. Sette, C.A. Kipke, D.M. Eichhorn, M.K. Chan, W.H. Armstrong, E. Libby, G. Christou, S. Brooker, V. McKee, O.C. Mullins and J.C. Fuggle, J. Am. Chem. Soc., 113 (1991) 7937.

[Cre92] G. Cressey, C.M.B. Henderson and G. van der Laan, Phys. Chem. Miner., 20 (1993) 111.

[Cur74] D. Curie, C. Barthon and B. Canny, J. Chem. Phys., 61 (1974) 3048.

[Czy89] M.T. Czyżyk, R.A. de Groot, G. Dalba, P. Fornasini, A. Kisiel, F. Rocca and E. Burattini, Phys. Rev. B, 39 (1989) 9831.

[Czy90] M.T. Czyżyk and R.A. de Groot, in A. Balerna, E. Bernieri and S. Mobilio (Eds.), Proc. 2nd European Conference on Progress in X-ray Synchrotron Radiation Research, Rome, November 1989, SIF, Bologna, 1990, p. 47.

[Czy92] M.T. Czyżyk, R. Potze and G.A. Sawatzky, Phys. Rev. B, 46 (1992) 3729.

[Czy93] M.T. Czyżyk, unpublished results.

[Daa91] G.H.O. Daalderop, P.J. Kelly and M.F.H. Schuurmans, Phys. Rev. B, 44 (1991) 12054.

[Dav86a] I. Davoli, A. Marcelli, A. Bianconi, M. Tomellini and M. Fanfoni, Phys. Rev. B, 33 (1986) 2979.

[Dav86b] I. Davoli, M. Tomellini and M. Fanfoni, J. Phys. (Paris) C, 8 (1986) 517.

[Dec89] M. de Crescenzi, J. Derrien, E. Chainet and K. Orumchian, Phys. Rev. B, 39 (1989) 5520.

[Ded84] P.H. Dederichs, S. Blügel, R. Zeller and H. Akai, Phys. Rev. B, 53 (1984) 2512.

[Deg89] F.M.F. de Groot, M. Grioni, J.C. Fuggle, J. Ghijsen and G.A. Sawatzky, Phys. Rev. B, 40 (1989) 5715.

[Deg90a] F.M.F. de Groot, J.C. Fuggle, B.T. Thole and G.A. Sawatzky, Phys. Rev. B, 41 (1990) 928.

[Deg90b] F.M.F. de Groot, J.C. Fuggle, B.T. Thole and G.A. Sawatzky, Phys. Rev. B, 42 (1990) 5459.

[Deg91t] F.M.F. de Groot, Ph.D. Thesis, University of Nijmegen, 1991.

[Deg92] F.M.F. de Groot, M.O. Figueiredo, M.J. Basto, M. Abbate, H. Petersen and J.C. Fuggle, Phys. Chem. Miner., 19 (1992) 140.

[Deg93a] F.M.F. de Groot, J. Faber, J.J.M. Michiels, M.T. Czyżyk, M. Abbate and J.C. Fuggle, Phys. Rev. B, 48 (1993) 2074.

[Deg93b] F.M.F. de Groot, M. Abbate, J. van Elp, G.A. Sawatzky, Y.J. Ma, C.T. Chen and F. Sette, J. Phys. Condensed Matter, 5 (1993) 2277.

[Deg93c] F.M.F. de Groot, J. Electron Spectrosc. Relat. Phenom., 62 (1993) 111.

[Deg●●] F.M.F. de Groot, unpublished results.

[Dep86] U. del Pennino, C. Mariani, S. Valeri, G. Ottavianni, M.G. Betti, S. Nannarone and M. de Crescenzi, Phys. Rev. B, 34 (1986) 2875.

[Des83] A. Desideri and C. Rotilio, in A. Bianconi, L.

Incoccia and S. Stipcich (Eds.), EXAFS and Near Edge Structure, Springer-Verlag, Berlin, 1983, p. 342.

[Dol91] M. Dolg, P. Fulde, W. Küchle, C.S. Neumann and H. Stoll, J. Chem. Phys., 94 (1991) 3011.

[Dom91] M. Domke, C. Xue, A. Puschmann, T. Mandel, E. Hudson, D.A. Shirley, G. Kaindl, C.H. Greene, H.R. Sadeghpour and H. Petersen, Phys. Rev. Lett., 66 (1991) 1306.

[Duh82] P.J. Durham, J.B. Pendry and C.H. Hodges, Comp. Phys. Commun., 25 (1982) 193.

[Dur90] O. Durmeyer, J.P. Kappler, E. Beaurepaire, J.M. Heintz and M. Drillon, J. Phys. Condensed Matter, 2 (1990) 6127.

[Ebe88a] H. Ebert, P. Strange and B.L. Gyorffy, J. Appl. Phys., 63 (1988) 3055.

[Ebe88b] H. Ebert, P. Strange and B.L. Gyorffy, Z. Phys. B, 73 (1988) 77.

[Ebe89a] H. Ebert and R. Zeller, Physica B, 161 (1989) 191.

[Ebe89b] H. Ebert, B. Drittler, R. Zeller and G. Schütz, Solid State Commun., 69 (1989) 485.

[Ebe90] H. Ebert and R. Zeller, Phys. Rev. B, 42 (1990) 2744.

[Ebe91] H. Ebert, R. Wienke, G. Schütz and W.M. Temmerman, Physica B, 172 (1991) 71.

[Edw89] B. Edwards, C.D. Garner and G. Stedman, Physica B, 158 (1989) 223.

[Ela93] M. Elango, A. Ausmees, A. Kikas, E. Nommiste, A. Saar, J.F. van Acker, J.N. Andersen, R. Nyholm and I. Martinson, Phys. Rev. B, 47 (1993) 11736.

[Eme87] V.J. Emery, Phys. Rev. Lett., 58 (1987) 2794.

[Erb88] A. Erbil, G.S. Cargill III, R. Frahm and R.F. Boehme, Phys. Rev. B, 37 (1988) 2450.

[Eri90a] O. Eriksson, L. Nordström, A. Pohl, L. Severin, A.M. Boring and B. Johansson, Phys. Rev B, 41 (1990) 11807.

[Eri90b] O. Eriksson, B. Johansson, R.C. Albers, A.M. Boring and M.S.S. Brooks, Phys. Rev. B, 42 (1990) 2707.

[Ers75] J.L. Erskine and E.A. Stern, Phys. Rev. B, 12 (1975) 5016.

[Esk91a] H. Eskes and G.A. Sawatzky, Phys. Rev. B, 43 (1991) 119.

[Esk91b] H. Eskes, M.B.J. Meinders and G.A. Sawatzky, Phys. Rev. Lett., 67 (1991) 1035.

[Esk92t] H. Eskes, Some Unusual Aspects of Correlated Systems, Ph.D. Thesis, University of Groningen, 1992.

[Fal84] L.M. Falicov and R.H. Victora, Phys. Rev. B, 30 (1984) 1695.

[Fin85] J. Fink, Th. Müller-Heinzerling, B. Scheerer, W. Speier, F.U. Hillebrecht, J.C. Fuggle, J. Zaanen and G.A. Sawatzky, Phys. Rev. B, 32 (1985) 4899.

[Fis73] D.W. Fisher, Phys. Rev. B, 8 (1973) 3576.

[Fis90a] P. Fisher, G. Schütz and G. Wiesinger, Solid State Commun., 76 (1990) 777.

[Fis90b] M. Fisher, B. Bonello, J.P. Itie, A.P. Polian, E. Dartyge, A. Fontaine and H. Tolentino, Phys. Rev. B, 42 (1990) 8494.

[Fra86] K.H. Frank, E.E. Koch and H.W. Biester, in J. Phys. (Paris) C, 8 (1986) 653.

[Fug88] J.C. Fuggle, G.A. Sawatzky and J.W. Allen (Eds.), Narrow Band Phenomena, Plenum Press, New York, 1988, p. 3.

[Fug90] J.C. Fuggle, Core Level Spectroscopies and Synchrotron Radiation, in R. Rosei (Ed.), Proc. Int. School of Physics, North Holland, Amsterdam, 1990, p. 127.

[Fug91] I.H. Munro, C.A. Boardman and J.C. Fuggle, World Compendium of Synchrotron Radiation Facilities, European Synchrotron Radiation Society, 1991.

[Fuj84a] A. Fujimori, F. Minami and S. Sugano, Phys. Rev. B, 29 (1984) 5225.

[Fuj84b] A. Fujimori and F. Minami, Phys. Rev. B, 30 (1984) 957.

[Fuj92a] A. Fujimori, I. Hase, H. Namatame, Y. Fujishima, Y. Tokura, M. Nakamura, A. Misu, M. Abbate, F.M.F. de Groot, M.T. Czyżyk, J.C. Fuggle, O. Strebel, F. Lopez, M. Domke and G. Kaindl, Phys. Rev. B, 46 (1992) 9841.

[Fuj92b] A. Fujimori, I. Hase, Y. Tokura, M. Abbate, F.M.F. de Groot, J.C. Fuggle, H. Eisaki and S. Uchida, Physica B, 186–188 (1993) 981.

[Fuj93] A. Fujimori, A.E. Bocquet, T. Saitoh and T. Mizokawa, J. Electron Spectrosc. Relat. Phenom., 62 (1993) 141.

[Ful91] P. Fulde and H. Stoll, J. Chem. Phys., 97 (1992) 4185.

[Gar87] K.B. Garg, H.S. Chauhan, U. Chandra, K.S. Jerath and F. Grandjean, Solid State Commun., 62 (1987) 575.

[Geo92] S. George, J. van Elp, J. Chen, Y. Ma, C.T. Chen, J.B. Park, M.W.W. Adams, B.G. Searle, F.M.F. de Groot, J.C. Fuggle and S.P. Cramer, J. Am. Chem. Soc., 114 (1992) 4426.

[Gie91] A. Giesekus and L.M. Falicov, Phys. Rev. B, 44 (1991) 10449.

[Gle85] C. Gleitzer and J.B. Goodenough, Struct. Bonding (Berlin), 61 (1985) 1.

[God88] R.W. Godby, M. Schlüter and L.J. Sham, Phys. Rev. B, 37 (1988) 10159.

[God92] R.W. Godby, in J.C. Fuggle and J.E. Inglesfield (Eds.), Unoccupied Electronic States, Springer, Berlin, 1992, p. 51.

[Goe88] J.B. Goedkoop, B.T. Thole, G. van der Laan, G.A. Sawatzky, F.M.F. de Groot and J.C. Fuggle, Phys. Rev. B, 37 (1988) 2086.

[Goe89t] J.B. Goedkoop, X-ray Dichroism of Rare Earth Materials, Ph.D. Thesis, University of Nijmegen, 1989.

[Goo63] J.B. Goodenough, Magnetism and the Chemical Bond, Wiley Interscience, New York, 1963.

[Goo71] J.B. Goodenough, in H. Reiss (Ed.), Progress in Solid State Chemistry, Pergamon Press, Oxford, 1971.

[Grf64] J.S. Griffith, The Theory of Transition Metal Ions, University Press, Cambridge, UK, 1964, Chapt. 9.

[Gri89a] M. Grioni, M.T. Czyżyk, F.M.F. de Groot, J.C. Fuggle and B.E. Watts, Phys. Rev. B, 39 (1989) 4886.
[Gri89b] M. Grioni, J.B. Goedkoop, R. Schoorl, F.M.F. de Groot, J.C. Fuggle, F. Schäfers, E.E. Koch, G. Rossi, J.M. Esteva and R.C. Karnatak, Phys. Rev. B, 39 (1989) 1541.
[Gru83] L.A. Grunes, Phys. Rev. B, 27 (1983) 2111.
[Gun74] O. Gunnarsson, B.I. Lundqvist and J.W. Wilkins, Phys. Rev. B, 10 (1974) 1319.
[Gun83] O. Gunnarsson and K. Schönhammer, Phys. Rev. B, 28 (1983) 4315.
[Gun85] O. Gunnarsson and K. Schönhammer, Phys. Rev. B, 31 (1985) 4815.
[Gun88a] O. Gunnarsson, O.K. Andersen, O. Jepsen and J. Zaanen, in J. Kanamori and A. Kotani (Eds.), Core-Level Spectroscopy in Condensed Systems, Springer-Verlag, Berlin, 1988, p. 82.
[Gun88b] O. Gunnarsson and O. Jepsen, Phys. Rev. B, 38 (1988) 3568.
[Gun89a] O. Gunnarsson, O.K. Andersen, O. Jepsen and J. Zaanen, Phys. Rev. B, 39 (1989) 1708.
[Gun89b] O. Gunnarsson and K. Schönhammer, Phys. Rev. B, 40 (1989) 4160.
[Gun90] O. Gunnarsson, Phys. Rev. B, 41 (1990) 514.
[Gup74] R.P. Gupta and S.K. Sen, Phys. Rev. B, 10 (1974) 71.
[Gup75] R.P. Gupta and S.K. Sen, Phys. Rev. B, 12 (1975) 15.
[Gyo73] B.L. Gyorffy and M.J. Stott, in D.J. Fabian and L.M. Watson (Eds.), Band Structure Spectroscopy in Metals and Alloys, Academic Press, London, 1973, p. 385.
[Hah82] J.E. Hahn, R.A. Scott, K.O. Hodgson, D. Doniach, S.R. Desjardins and E.I. Solomon, Chem. Phys. Lett., 88 (1982) 595.
[Ham93] K. Hämäläinen, C.C. Kao, J.B. Hastings, D.P. Siddons, L.E. Berman, V. Stojanoff and S.P. Cramer, Phys. Rev. B, 46 (1992) 14274.
[Has83] S.S. Hasnain and B. Piggott, in A. Bianconi, L. Incoccia and S. Stipcich (Eds.), EXAFS and Near Edge Structure, Springer-Verlag, Berlin, 1983, p. 358.
[Haz90] S. Hamza, M.A. Khan, S. Lewonczuk, J. Ringeissen, J. Petiau and P. Sainctavit, in A. Balerna, E. Bernieri and S. Mobilio (Eds.), Proc. 2nd European Conference on Progress in X-ray Synchrotron Radiation Research, Rome, November 1989, SIF, Bologna, 1990, p. 809.
[Hed65] L. Hedin, Phys. Rev. A, 139 (1965) 796.
[Hed69] L. Hedin and B.I. Lundqvist, Solid State Phys., 23 (1969) 1.
[Hem91] B. Heddman, P. Frank, K.O. Hodgson, B.J. Feldman, S.F. Gheller, F.A. Schutz and W.E. Newton, in S.S. Hasnain (Ed.), X-ray Absorption Fine Structure, Vol. VI, Ellis Horwood, Chichester, 1991, p. 168.
[Hen79] B.L. Henke, J. Liesegang and S.D. Smith, Phys. Rev. B, 19 (1979) 3004.
[Him91] F.J. Himpsel, U.O. Karlsson, A.B. McLean, L.J. Terminello, F.M.F. de Groot, M. Abbate, J.C. Fuggle, J.A. Yarmoff, B.T. Thole and G.A. Sawatzky, Phys. Rev. B, 43 (1991) 6899.
[Hit89a] A.P. Hitchcock and E. Rühl, Physica B, 158 (1989) 403.
[Hit89b] A.P. Hitchcock, S. Bodeur and M. Tronc, Physica B, 158 (1989) 257.
[Hit90] A.P. Hitchcock, A.T. Wen and E. Rühl, Chem. Phys., 147 (1990) 51.
[Hoh64] P.C. Hohenberg and W. Kohn, Phys. Rev., 136 (1964) 864.
[Hu85] C.D. Hu and D.C. Langreth, Phys. Scr., 32 (1985) 391.
[Hub63] J. Hubbard, Proc. R. Soc. London, Ser. A, 276 (1963) 238.
[Hub64] J. Hubbard, Proc. R. Soc. London, Ser. A, 277 (1964) 237.
[Hub67] J. Hubbard, Proc. R. Soc. London, Ser. A, 281 (1967) 401.
[Hul84] S.L. Hulbert, B.A. Bunker, F.C. Brown and P. Pianetta, Phys. Rev. B, 30 (1984) 2120.
[Hun27] F. Hund, Linienspektren und Periodisches System der Elemente, Julius Springer, Berlin, 1927, pp. 124 ff.
[Hyb89] M.S. Hybertsen, M. Schlüter and N.E. Christensen, Phys. Rev. B, 39 (1989) 9028.
[Hyb92] M.S. Hybertsen, E.B. Stechel, W.M.C. Foulkes and M. Schlüter, Phys. Rev. B, 45 (1992) 32.
[Ima89a] S. Imada and T. Jo, J. Phys. Soc. Jpn., 58 (1989) 402.
[Ima89b] S. Imada and T. Jo, J. Phys. Soc. Jpn., 58 (1989) 2665.
[Ima90] S. Imada and T. Jo, Phys. Scr., 41 (1990) 115.
[Ima92] S. Imada and T. Jo, J. Magn. Magn. Mater., 104 (1992) 2001.
[Ing91] J.E. Inglesfield, Principles of Band Structure, Workshop, Vlieland, April 1991, unpublished.
[Ish90] Y. Ishii and K. Terakura, Phys. Rev. B, 42 (1990) 10924.
[Ito93] F. Itoh, M. Nakamura, H. Sakurai, H. Kiriake, M. Nawate, S. Honda and H. Kawata, Jpn. J. Appl. Phys., 32 (1993) 326.
[Iva44] D. Ivanenko and J. Pomeranchuk, Phys. Rev., 65 (1944) 343.
[Iwa86] K. Iwai, M. Iwai, K. Suto, S. Nakashima, I. Motoyama, H. Sano, I. Ikemoto, N. Kosugi and H. Kuroda, Bull. Chem. Soc. Jpn., 59 (1986) 2675.
[Jac91] W.E. Jackson, G.E. Brown Jr., G.A. Waychunas, J. Mustre de Leon, S.D. Conradson and J.M. Combes, in S.S. Hasnain (Ed.), X-ray Absorption Fine Structure, Vol. VI, Ellis Horwood, Chichester, 1991, p. 298.
[Jak77] J. Jaklevic, J.A. Kirby, M.P. Klein, A.S. Robertson, G.S. Brown and P. Eisenberger, Solid State Commun., 23 (1977) 679.
[Jan88] G.J.M. Jansen and W.C. Nieuwport, Phys. Rev. B, 38 (1988) 3449.

[Jo88a] T. Jo and A. Kotani, Theory of high energy spectroscopy in CeO_2, in J. Kanamori and A. Kotani (Eds.), Core Level Spectroscopy, Springer-Verlag, Berlin, 1988, p. 34.
[Jo88b] T. Jo and A. Kotani, J. Phys. Soc. Jpn., 57 (1988) 2288.
[Jo88c] T. Jo and A. Kotani, Phys. Rev. B, 38 (1988) 830.
[Jo89a] T. Jo, J. Phys. Soc. Jpn., 58 (1989) 1452.
[Jo89b] R.O. Jones and O. Gunnarsson, Rev. Mod. Phys., 61 (1989) 689.
[Jo91] T. Jo and G.A. Sawatzky, Phys. Rev. B, 43 (1991) 8771.
[Jo92] T. Jo, A. Yoshida and G.A. Sawatzky, J. Magn. Magn. Mater., 104 (1992) 2087.
[Jon68] K.H. Johnson, Phys. Lett. A, 27 (1968) 138.
[Jor62] C.K. Jorgensen, Absorption Spectra and Chemical Bonding in Complexes, Pergamon Press, Oxford, 1962.
[Jor71] C.K. Jorgensen, Modern Aspects of Ligand Field Theory, North Holland, Amsterdam, 1971.
[Kag91] H. Kageyama and N. Kamijo, in S.S. Hasnain (Ed.), X-ray Absorption Fine Structure, Vol. VI, Ellis Horwood, Chichester, 1991, p. 442.
[Kai89] G. Kaindl, O. Strebel, A. Kolodziejczyk, W. Schäfer, R. Kiemel, S. Lösch, S. Kemmler-Sack, R. Hoppe, H.P. Müller and D. Kissel, Physica B, 158 (1989) 446.
[Kap91] R.J.H. Kappert, H.R. Borsje and J.C. Fuggle, J. Magn. Magn. Mater., 100 (1991) 363.
[Kap92t] R.J.H. Kappert, Spectroscopic Studies of Local Magnetic Properties in Metals, Ph.D. Thesis, University of Nijmegen, 1992.
[Kar70] K.M. Karplus and R.N. Porter, Atoms and Molecules, Benjamin, Marlo Park, 1970.
[Kau87] L.S. Kau, D.J. Spira-Solomon, J.E. Penner-Hahn, K.O. Hodgson and E.I. Solomon, J. Am. Chem. Soc., 109 (1987) 6433.
[Kev70] E.T. Keve, S.C. Abrahams and J.L. Bernstein, J. Chem. Phys., 53 (1970) 3279.
[Kit86] M. Kitamura, S. Muramatsu and C. Sugiura, Phys. Rev. B, 33 (1986) 5294.
[Kit90] M. Kitamura and S. Muramatsu, Phys. Rev. B, 41 (1990) 1158.
[Kiz88] P. Kizler, P. Lamparter and S. Steeb, Z. Naturforsch., Teil A, 44 (1988) 189.
[Kiz89] P. Kizler, P. Lamparter and S. Steeb, Physica B, 158 (1989) 392.
[Kiz91] P. Kizler, Phys. Rev. Lett., 67 (1991) 3555.
[Kiz92a] P. Kizler, Phys. Rev. B, 46 (1992) 10540.
[Kiz92b] P. Kizler, Phys. Lett. A, 172 (1993) 66.
[Kna82] G.S. Knapp, B.W. Veal, H.K. Pan and T. Klippert, Solid State Commun., 44 (1982) 1343.
[Knu93] M. Knülle, S. Stähler, G. Schütz, P. Fisher, F.M.F. de Groot, P. Blaha and K. Schwartz, submitted to Phys. Rev. B.
[Kob93] K. Kobayashi, H. Maruyama, H. Maeda and H. Yamazaki, Jpn. J. Appl. Phys., 32 (1993) 311.
[Koc77] E.E. Koch, B. Kunz and B. Sonntag, Phys. Rep., 29 (1977) 153.
[Koc85] E.E. Koch, Y. Yugnet and F.J. Himpsel, Chem. Phys. Lett., 116 (1985) 7.
[Koh65] W. Kohn and L.J. Sham, Phys. Rev., 140 (1965) 1133.
[Kot89] A. Kotani, H. Ogasawara, K. Okada, B.T. Thole and G.A. Sawatzky, Phys. Rev. B, 40 (1989) 65.
[Kot92] A. Kotani and K. Okada, Core-level spectroscopy in transition metal compounds, in Recent Advances in Magnetism of Transition Metal Compounds, World Scientific, Singapore, 1992.
[Kra30] K. Kramers, Akad van Wetenschappen, Amsterdam, 33 (1930) 959.
[Kri90] K.M. Krishnan, Ultramicroscopy, 32 (1990) 309.
[Kro90] A. Krol, C.J. Sher and Y.H. Kao, Phys. Rev. B, 42 (1990) 3829.
[Kru88] B.C.H. Krutzen and F. Springelkamp, J. Phys. Condensed Matter, 1 (1989) 8369.
[Krv90] O.L. Krivanek and J.H. Paterson, Ultramicroscopy, 32 (1990) 313.
[Kua92] X.Y. Kuang, Z. Wu and I. Morgenstern-Badarau, Phys. Rev. B, 45 (1992) 8104.
[Kue90] U. Kuetgens and J. Hormes, in A. Balerna, E. Bernieri and S. Mobilio (Eds.), Proc. 2nd European Conference on Progress in X-ray Synchrotron Radiation Research, Rome, November 1989, SIF, Bologna, 1990, p. 59.
[Kui88] P. Kuiper, G. Kruizinga, J. Ghijsen, M. Grioni, P.J.W. Weijs, F.M.F. de Groot, G.A. Sawatzky, H. Verweij, L.F. Feiner and H. Petersen, Phys. Rev. B, 37 (1988) 6483.
[Kui89] P. Kuiper, G. Kruizinga, J. Ghijsen and G.A. Sawatzky, Phys. Rev. Lett., 62 (1989) 221.
[Kui90t] P. Kuiper, Ph.D. Thesis, University of Groningen, 1990.
[Kui91] P. Kuiper, J. van Elp, G.A. Sawatzky, A. Fujimori, S. Hosoya and D.M. de Leeuw, Phys. Rev. B, 44 (1991) 4570.
[Kui93] P. Kuiper, B.G. Searle, P. Rudolf, L.H. Tjeng and C.T. Chen, Phys. Rev. Lett., 70 (1993) 1549.
[Kus91] M. Kusunoki, T. Ono, Y. Inoue, M. Suzuki, A. Uehara, T. Matsushita and H. Oyanagi, in S.S. Hasnain (Ed.), X-ray Absorption Fine Structure, Vol. VI, Ellis Horwood, Chichester, 1991, p. 174.
[Kut80] F.W. Kutzler, C.R. Natoli, D.K. Misemer, S. Doniach and K.O. Hodgson, J. Chem. Phys., 73 (1980) 3274.
[Kut84] F.W. Kutzler and D.E. Ellis, Phys. Rev. B, 29 (1984) 6890.
[Laa86a] G. van der Laan, J. Zaanen, G.A. Sawatzky, R. Karnatak and J.-M. Esteva, Phys. Rev. B, 33 (1986) 4253.
[Laa86b] G. van der Laan, B.T. Thole, G.A. Sawatzky, J.B. Goedkoop, J.C. Fuggle, J.-M. Esteva, R.C. Karnatak, J.P. Remeika and H.A. Dabkowska, Phys. Rev. B, 34 (1986) 6529.

[Laa87] G. van der Laan, J.B. Goedkoop and A.A. MacDowell, J. Phys. E, 20 (1987) 1496.
[Laa88a] G. van der Laan and B.T. Thole, Phys. Rev. Lett., 60 (1988) 1977.
[Laa88b] G. van der Laan and B.T. Thole, Phys. Rev. B, 37 (1988) 6587.
[Laa88c] G. van der Laan and B.T. Thole, J. Electron Spectrosc. Relat. Phenom., 46 (1988) 123.
[Laa90a] G. van der Laan and B.T. Thole, Phys. Rev. B, 42 (1990) 6670.
[Laa90b] G. van der Laan, S.C. Mythen and H.A. Padmore, Europhys. Lett., 11 (1990) 67.
[Laa90c] G. van der Laan, Phys. Rev. B, 41 (1990) 12366.
[Laa90d] G. van der Laan, in A. Balerna, E. Bernieri and S. Mobilio (Eds.), Proc. 2nd European Conference on Progress in X-ray Synchrotron Radiation Research, Rome, November 1989, SIF, Bologna, 1990, p. 243.
[Laa91] G. van der Laan and B.T. Thole, Phys. Rev. B, 43 (1991) 13401.
[Laa92a] G. van der Laan and B.T. Thole, J. Phys. Condensed Matter, 4 (1992) 4181.
[Laa92c] G. van der Laan and Kirkmann, J. Phys. Condensed Matter, 4 (1992) 4189.
[Lan80] D.C. Langreth and J.P. Perdew, Phys. Rev. B, 21 (1980) 5469.
[Lan83] D.C. Langreth and M.J. Mehl, Phys. Rev. B, 28 (1983) 1809.
[Lea80] R.D. Leapman and L.A. Grunes, Phys. Rev. Lett., 45 (1980) 397.
[Lea82] R.D. Leapman, L.A. Grunes and P.L. Fejes, Phys. Rev. B, 26 (1982) 614.
[Len86] M. Lenglet, R. Guillamet, A.D. D'Huyser, J. Dürr and C.K. Jorgensen, J. Phys. (Paris) C, 8 (1986) 764.
[Len88] M. Lenglet, A.D. D'Huyser and J. Dürr, Ann. Chim. Fr., 13 (1988) 505.
[Leu90] H. van Leuken, A. Lodder, M.T. Czyżyk, F. Springelkamp and R.A. de Groot, Phys. Rev. B, 41 (1990) 5613.
[Loo89] M. Loos, P. Friant, J.M. Barbe and R. Guillard, Physica B, 158 (1989) 231.
[Lop92] M.F. Lopez, A. Höhr, C. Laubschat, M. Domke and G. Kaindl, Europhys. Lett., 20 (1992) 357.
[Lyn87] D.W. Lynch and R.D. Cowan, Phys. Rev. B, 36 (1987) 9228.
[Lyt88] F.W. Lytle, R.B. Greegor and A.J. Panson, Phys. Rev. B, 37 (1988) 1550.
[Mae86] H. Maezawa, S. Nakai, S. Mitani, H. Noda, T. Namioka and T. Sasaki, Nucl. Instrum. Methods, 246 (1986) 310.
[Mar85t] D. van der Marel, Ph.D. Thesis, University of Groningen, 1985.
[Mar88] D. van der Marel and G.A. Sawatzky, Phys. Rev. B, 37 (1988) 10674.
[Mas92b] S. Massida, M. Posternak and A. Baldereshi, Phys. Rev. B, 46 (1992) 11705.
[Mat72a] L.F. Mattheiss, Phys. Rev. B, 5 (1972) 290.
[Mat72b] L.F. Mattheiss, Phys. Rev. B, 5 (1972) 306.
[May91] H. Maruyama, T. Iwazumi, H. Kawata, A. Koizumi, M. Fujita, H. Sakurai, F. Itoh, K. Namikawa, H. Yamazaki and M. Ando, J. Phys. Soc. Jpn., 60 (1991) 1456.
[May92] H. Maruyama, A. Koizumi, H. Yamazaki, T. Iwazumi and H. Kawata, J. Magn. Magn. Mater., 104 (1992) 2055.
[Mcc65] J.B. McChesney, R.C. Sherwood and J.F. Potter, J. Chem. Phys., 43 (1965) 1907.
[Mcl90] A.B. McLean, L.J. Terminello and F.J. Himpsel, Phys. Rev. B, 41 (1990) 7694.
[Mcm88a] A.K. McMahan, R.M. Martin and S. Satpathy, Phys. Rev. B, 38 (1988) 6650.
[Mcm88b] A.K. McMahan and R.M. Martin, in J.C. Fuggle, G.A. Sawatzky and J.W. Allen (Eds.), Narrow Band Phenomena, Plenum Press, New York, 1988, p. 133.
[Mey71] W. Meyer, Int. J. Quantum Chem., S5 (1971) 341.
[Miy91] T. Miyazaki, Y. Ishii and K. Terakura, Prog. Theor. Phys., Suppl., 106 (1991) 173.
[Mol34] C. Møller and M.S. Plesset, Phys. Rev., 46 (1934) 618.
[Mot90] A. Mottana, E. Paris, G. Della Ventura and J.L. Robert, Rend. Fis. Acc. Lincei, 1 (1990) 387.
[Mot91] A. Mottana, E. Paris, I. Davoli and L.M. Anovitz, Rend. Fis. Acc. Lincei, 2 (1991) 379.
[Mul78] J.E. Müller, O. Jepsen, O.K. Andersen and J.W. Wilkins, Phys. Rev. Lett., 40 (1978) 720.
[Mul82] J.E. Müller, O. Jepsen and J.W. Wilkins, Solid State Commun., 42 (1982) 365.
[Mul84] J.E. Müller and J.W. Wilkins, Phys. Rev. B, 29 (1984) 4331.
[Nak85] S.I. Nakai, K. Ogata, M. Ohashi, C. Sugiura, T. Mitsuishi and H. Maezawa, J. Phys. Soc. Jpn., 54 (1985) 4034.
[Nak87] S.I. Nakai, T. Mishuishi, H. Sugawara, H. Maezawa, T. Matsukawa, S. Mitani, K. Yamasaki and T. Fujikawa, Phys. Rev. B, 36 (1987) 9241.
[Nak88] S.I. Nakai, A. Kawata, M. Ohashi, M. Kitamura, C. Sugiura, T. Mitsuishi and H. Maezawa, Phys. Rev. B, 37 (1988) 10895.
[Nat83] R. Natoli, in A. Bianconi, L. Incoccia and S. Stipcich (Eds.), EXAFS and Near Edge Structure, Springer-Verlag, Berlin, 1983, p. 43.
[Nat86a] C.R. Natoli and M. Benfatto, J. Phys. (Paris) C, 8 (1986) 11.
[Nat86b] C.R. Natoli, M. Benfatto and S. Doniach, Phys. Rev. B, 34 (1986) 4682.
[Nie63] C.W. Nielson and G.F. Koster, Spectroscopic Coefficients for the p^N, d^N and f^N Configurations, M.I.T. Press, Cambridge, Massachusetts, 1963.
[Nor85] D. Norman, K.B. Garg and P.J. Durham, Solid State Commun., 56 (1985) 895.
[Nor90] M.R. Norman, Phys. Rev. Lett., 64 (1990) 1162; 64 (1990) 2466 (E).

[Ogu83] T. Oguchi, T.K. Terakura and A.R. Williams, Phys. Rev. B, 28 (1983) 6443.
[Ogu84] T. Oguchi, K. Terakura and A.R. Williams, J. Appl. Phys., 55 (1984) 2318.
[Ohn83] Y. Ohno, K. Hirama, S. Nakai, C. Sugiura and S. Okada, Phys. Rev. B, 27 (1983) 3811.
[Ohn85] Y. Ohno and S.I. Nakai, J. Phys. Soc. Jpn., 54 (1985) 3591.
[Oka89] K. Okada and A. Kotani, J. Phys. Soc. Jpn., 58 (1989) 2578.
[Oka90] K. Okada and A. Kotani, J. Electron Spectrosc. Relat. Phenom., 53 (1990) 313.
[Oka91a] K. Okada and A. Kotani, J. Phys. Soc. Jpn., 60 (1991) 772.
[Oka92a] K. Okada, A. Kotani and B.T. Thole, J. Electron Spectrosc. Relat. Phenom., 58 (1992) 325.
[Oka92b] K. Okada and A. Kotani, J. Phys. Soc. Jpn., 61 (1992) 449.
[Oka93] K. Okada and A. Kotani, J. Electron Spectrosc. Relat. Phenom., 62 (1993) 131.
[Oya89] H. Oyanagi, K. Oka, H. Unoki, Y. Nishihara and K. Murata, Physica B, 158 (1989) 436.
[Pad87] H. Padmore, in Proceedings of the International Conference on Soft X-ray Optics and Technology, SPIE J., 733 (1987) 253.
[Pad89] H. Padmore, Rev. Sci. Instrum., 60 (1989) 1608.
[Par88] J. Park, S. Ryu, M.S. Han and S.J. Oh, Phys. Rev. B, 37 (1988) 10867.
[Pat90] J.H. Paterson and O.L. Krivanek, Ultramicroscopy, 32 (1990) 319.
[Ped89] M. Pedio, J.C. Fuggle, J. Somers, E. Umbach, J. Haase, Th. Lindner, U. Höfer, M. Grioni, F.M.F. de Groot, B. Hilert, L. Becker and A. Robinson, Phys. Rev. B, 40 (1989) 7924.
[Ped90] M. Pedio, L. Becker, B. Hillert, S.D. Addato and J. Haase, Phys. Rev. B, 41 (1990) 7462.
[Pea79] D.M. Pease and L.V. Azaroff, J. Appl. Phys., 50 (1979) 6605.
[Pea86] D.M. Pease, S.D. Bader, M.B. Brodsky, J.I. Budnick, T.I. Morrison and N.J. Zaluzec, Phys. Lett. A, 114 (1986) 491.
[Pei83] J. Petiau and C. Calas, in A. Bianconi, L. Incoccia and S. Stipcich, EXAFS and Near Edge Structure, Springer-Verlag, Berlin, 1983, p. 144.
[Pen91] J.E. Penner-Hahn, S. Wang and G.S. Waldo, in S.S. Hasnain (Ed.), X-ray Absorption Fine Structure, Ellis Horwood, Chichester, 1991, p. 146.
[Pen●●] H. Pen, unpublished results.
[Peo88] D.H. Pearson, B Fultz and C.C. Ahn, Appl. Phys. Lett., 53 (1988) 1405.
[Per79] J.P. Perdew, Chem. Phys. Lett., 64 (1979) 127.
[Per80] J.P. Perdew and A. Zunger, Phys. Rev. B, 23 (1980) 5048.
[Per86a] J.P. Perdew and Y. Wang, Phys. Rev. B, 33 (1986) 8800.
[Per86b] J.P. Perdew, Phys. Rev. B, 33 (1986) 8822.
[Per92a] J.P. Perdew and Y. Wang, Phys. Rev. B, 45 (1992) 13298.
[Per92b] J.P. Perdew, J.A. Chevary, S.H. Vosko, K.A. Jackson, M.R. Pederson, D.J. Singh and C. Fiolhais, Phys. Rev. B, 46 (1992) 6671.
[Pet82] H. Petersen, Opt. Commun., 40 (1982) 402.
[Pet86] H. Petersen, Nucl. Instrum. Methods A, 246 (1986) 260.
[Pfl82] J. Pflüger, J. Fink, G. Crecelius, K.P. Bohnen and H. Winter, Solid State Commun., 44 (1982) 489.
[Pom91] M. Pompa, C. Li, A. Bianconi, A. Congiu Catellano, S. Della Longa, A.M. Flank, P. Lagarde and D. Udron, Physica C, 184 (1991) 51.
[Pot●●] R. Potze, unpublished results.
[Pou90] B. Poumellec, R. Cortes, G. Tourillon and J. Berthon, in A. Balerna, E. Bernieri and S. Mobilio (Eds.), Proc. 2nd European Conference on Progress in X-ray Synchrotron Radiation Research, Rome, November 1989, SIF, Bologna, 1990, p. 23.
[Pou91] B. Poumellec, P.J. Durham and G.Y. Guo, J. Phys. Condensed Matter, 3 (1991) 8195.
[Raj63] K. Rajnak and B.G. Wybourne, Phys. Rev., 132 (1963) 280.
[Raj64] K. Rajnak and B.G. Wybourne, Phys. Rev., 134 (1964) 596.
[Reh93] J.J. Rehr, Jpn. J. Appl. Phys., 32 (1993) 8.
[Rob87] S. Robaszkiewicz, R. Micnas and J. Ranninger, Phys. Rev. B, 36 (1987) 180.
[Rud92] P. Rudolf, F. Sette, L.H. Tjeng, G. Meigs and C.T. Chen, J. Magn. Magn. Mater., 109 (1992) 109.
[Rue91] S. Rüegg, G. Schütz, P. Fisher, R. Wienke, W.P. Zeper and H. Ebert, J. Appl. Phys., 69 (1991) 5655.
[Rui86] M.F. Ruiz-Lopez, D. Rinaldi, C. Esselin, J. Goulon, J.L. Poncet and R. Guillard, J. Phys. (Paris) C, 8 (1986) 637.
[Rui91] M.F. Ruiz-Lopez and A. Munoz-Paez, J. Phys. Condensed Matter, 3 (1991) 8981.
[Sac91a] M. Sacchi, O. Sakho and G. Rossi, Phys. Rev. B, 43 (1991) 1276.
[Sac91b] M. Sacchi, R.J.H. Kappert, J.C. Fuggle and E.E. Marinero, Appl. Phys. Lett., 59 (1991) 872.
[Sac92a] M. Sacchi, F. Sirotti, G. Rossi, R.J.H. Kappert, J. Vogel and J.C. Fuggle, J. Electron Spectrosc. Relat. Phenom., 58 (1992) 240.
[Sac92b] M. Sacchi, F. Sirotti and G. Rossi, Solid State Commun., 81 (1992) 977.
[Sai89] P. Sainctavit, J. Petiau, M. Benfatto and C.R. Natoli, Physica B, 158 (1989) 347.
[Sai90] P. Sainctavit, J. Petiau, M. Benfatto and C.R. Natoli, in A. Balerna, E. Bernieri and S. Mobilio (Eds.), Proc. 2nd European Conference on Progress in X-ray Synchrotron Radiation Research, Rome, November 1989, SIF, Bologna, 1990, p. 31.
[Sai91] P. Sainctavit and J. Petiau, in S.S. Hasnain (Ed.), X-ray Absorption Fine Structure, Ellis Horwood, Chichester, 1991, p. 35.
[Sai92] P. Sainctavit, D. Lefebvre, C. Cartier, C. Laffon, G. Krill, C. Brouder, J.P. Kappler, J.P. Schille and J. Goulon, J. Appl. Phys., 72 (1992) 1985.
[Sai93] P. Sainctavit, D. Lefebvre, M.A. Arrio, C. Cartier

dit Moulin, J.P. Kappler, J.P. Schille, G. Krill, C. Brouder and M. Verdaguer, Jpn. J. Appl. Phys., 32 (1993) 295.

[Sak93] H. Sakurai, F. Itoh, H. Maruyama, A. Koizumi, K. Kobayashi, H. Yamazaki, Y. Tanji and H. Kawata, J. Phys. Soc. Jpn., 62 (1993) 459.

[San83] J.M. Sanz and S. Hoffman, Surf. Interface Anal., 5 (1983) 210.

[Sar91] B.K. Sarpal, C. Blancard, J.P. Connerade, J.M. Esteva, J. Hormes, R.C. Karnatak and U. Kuetgens, J. Phys. B, 24 (1991) 1593.

[Saw84] G.A. Sawatzky and J.W. Allen, Phys. Rev. Lett., 53 (1984) 2339.

[Saw88] G.A. Sawatzky, in J. Kanamori and A. Kotani (Eds.), Core-Level Spectroscopy in Condensed Systems, Springer Series in Solid State Science, Berlin, 1988, p. 99.

[Scf92] F. Schäfers, B.R. Müller, J. Wong, T. Tanaka, Y. Kamimura, M. Krumrey and P. Müller, BESSY Jahresbericht, 1991.

[Sch87] G. Schütz, W. Wagner, W. Wilhelm, P. Kienle, R. Zeller, R. Frahm and G. Materlik, Phys. Rev. Lett., 58 (1987) 737.

[Sch88] G. Schütz, M. Knülle, R. Wienke, W. Wilhelm, P. Kienle and R. Frahm, Z. Phys. B, 73 (1988) 67.

[Sch89] G. Schütz, R. Wienke, W. Wilhelm, W. Wagner, P. Kienle and R. Frahm, Z. Phys. B, 75 (1989) 495.

[Sch90] G. Schütz, R. Wienke, W. Wilhelm, W.P. Zeper, H. Ebert and K. Spörl, J. Appl. Phys., 67 (1990) 4456.

[Sch92] G. Schütz and P. Fisher, Z. Phys. A, 341 (1992) 227.

[Sch93] G. Schütz, P. Fisher, S. Stähler, M. Knülle and K. Attenkofer, Jpn. J. Appl. Phys., 32 (1993) 869.

[Sci46] J. Schwinger, Phys. Rev., 70 (1946) 798.

[Sco89] R.A. Scott, Physica B, 158 (1989) 84.

[Sea79] M.P. Seah and W.A. Dench, Surf. Interface Anal., 1 (1979) 2.

[Set84] F. Sette, Stöhr and A.P. Hitchcock, Chem. Phys. Lett., 110 (1984) 517.

[Set90] F. Sette and C.T. Chen, in A. Balerna, E. Bernieri and S. Mobilio (Eds.), Proc. 2nd European Conference on Progress in X-ray Synchrotron Radiation Research, Rome, November 1989, SIF, Bologna, 1990, p. 363.

[Set91] F. Sette, C.T. Chen, Y. Ma, S. Modesti and N.V. Smith, in S.S. Hasnain (Ed.), X-ray Absorption Fine Structure, Vol. VI, Ellis Horwood, Chichester, 1991, p. 96.

[Sev93] L. Severin, M.S.S. Brooks and B. Johansson, Int. J. Mod. Phys. B, 7 (1993) 255.

[Sha87] T.K. Sham, Solid State Commun., 64 (1987) 1103.

[Shi82] S. Shin, S. Suga, M. Taniguchi, H. Kanzaki, S. Shibuya and T. Yamaguchi, J. Phys. Soc. Jpn., 51 (1982) 906.

[Shu76] R.G. Shulman, Y. Yafet, P. Eisenberger and W.E. Blumberg, Proc. Natl. Acad. Sci. USA, 73 (1976) 1384.

[Sin●●] B. Sinkovic, unpublished results.

[Smi76] D.Y. Smith, Phys. Rev. B, 13 (1976) 5303.

[Smi92] N.V. Smith, C.T. Chen, F. Sette and L.F. Mattheiss, Phys. Rev. B, 46 (1992) 1023.

[Sol91] A.V. Soldatov, T.S. Ivanchenko, S. Della Longa and A. Bianconi, Phys. Status Solidi B, 168 (1991) K43.

[Som92] J. Somers, X-ray absorption spectroscopy of small molecules, in J.C. Fuggle and J. Inglesfield (Eds.), Unoccupied Electronic States, Springer, Berlin, 1992, p. 177.

[Sor93] L. Soriano, M. Abbate, H. Pen, M.T. Czyżyk and J.C. Fuggle, J. Electron Spectrosc. Relat. Phenom., 62 (1993) 197.

[Spa84] T.G. Sparrow, B.G. Williams, C.N.R. Rao and J.M. Thomas, Chem. Phys. Lett., 108 (1984) 547.

[Sti89] S. Stizza, G. Mancini, M. Benfatto, C.R. Natoli, J. Garcia and A. Bianconi, Phys. Rev. B, 40 (1989) 12229.

[Sto84] J. Stöhr, F. Sette and A.L. Johnson, Phys. Rev. Lett., 53 (1984) 1684.

[Sto93] J. Stöhr and Y. Wu, New directions in research with third generation soft X-ray synchrotron radiation sources, NATO-ASI Ser., Kluwer, Deventer, 1993.

[Str89] P. Strange, H. Ebert, J.B. Staunton and B.L. Gyorffy, J. Phys. Condensed Matter, 1 (1989) 2959.

[Str91] R.W. Strange, L.W. Murphy, P. Durham and S.S. Hasnain, in S.S. Hasnain (Ed.), X-ray Absorption Fine Structure, Vol. VI, Ellis Horwood, Chichester, 1991, p. 32.

[Stu89] R. Stumm von Bordwehr, Ann. Phys. Fr., 14 (1989) 377.

[Sug70] S. Sugano, Y. Tanabe and H. Kitamura, Multiplets of Transition Metal Ions, Academic Press, New York, 1970.

[Sug82] S. Suga, S. Shin, M. Taniguchi, K. Inoue, M. Seki, I. Nakada, S. Shibuya and T. Yamaguchi, Phys. Rev. B, 25 (1982) 5487.

[Sva88a] A. Svane and O. Gunnarsson, Phys. Rev. B, 37 (1988) 9919.

[Sva88b] A. Svane and O. Gunnarsson, Europhys. Lett., 7 (1988) 171.

[Sva90a] A. Svane and O. Gunnarsson, Phys. Rev. Lett., 65 (1990) 1148.

[Sva90b] A. Svane and O. Gunnarsson, Solid State Commun., 76 (1990) 851.

[Sva92] A. Svane, Phys. Rev. Lett., 68 (1992) 1900.

[Szo93] Z. Szotek, W.M. Temmermann and H. Winter, Phys. Rev. B, 47 (1993) 4029.

[Szy90] R. Szymanski and E. Payen, in A. Balerna, E. Bernieri and S. Mobilio (Eds.), Proc. 2nd European Conference on Progress in X-ray Synchrotron Radiation Research, Rome, November 1989, SIF, Bologna, 1990, p. 805.

[Taf82] J. Taftø and O.L. Krivanek, Phys. Rev. Lett., 48 (1982) 560.

[Tan92a] A. Tanaka and T. Jo, J. Phys. Soc. Jpn., 61 (1992) 2040.

[Tan92b] A. Tanaka, T. Jo and G.A. Sawatzky, J. Phys. Soc. Jpn., 61 (1992) 2636.
[Tan92c] A. Tanaka and T. Jo, J. Phys. Soc. Jpn., 61 (1992) 2669.
[Tan93] Z. Tan, S.M. Heald, S.W. Cheong, A.S. Cooper and A.R. Moodenbaugh, Phys. Rev. B, 47 (1993) 12365.
[Tem93] W.M. Temmermann, Z. Szotek and H. Winter, Phys. Rev. B, 47 (1993) 11533.
[Ten85] I.M. Ternov, V.V. Mikhailov and V.R. Khalilov, Synchrotron Radiation and its Applications, Harwood Academic, 1985.
[Ter84] K. Terakura, T. Oguchi, A.R. Williams and J. Kübler, Phys. Rev. B, 30 (1984) 4734.
[Tho85a] B.T. Thole, G. van der Laan and G.A. Sawatzky, Phys. Rev. Lett., 55 (1985) 2086.
[Tho85b] B.T. Thole, G. van der Laan, J.C. Fuggle, G.A. Sawatzky, R.C. Karnatak and J.-M. Esteva, Phys. Rev. B, 32 (1985) 5107.
[Tho85c] B.T. Thole, R.D. Cowan, G.A. Sawatzky, J. Fink and J.C. Fuggle, Phys. Rev. B, 31 (1985) 6856.
[Tho88a] B.T. Thole, G. van der Laan and P.H. Butler, Chem. Phys. Lett., 149 (1988) 295.
[Tho88b] B.T. Thole and G. van der Laan, Phys. Rev. B, 38 (1988) 3158.
[Tho88c] B.T. Thole and G. van der Laan, Phys. Rev. A, 38 (1988) 1943.
[Tho92] B.T. Thole, P. Carra, F. Sette and G. van der Laan, Phys. Rev. Lett., 68 (1992) 1943.
[Tje91] L.H. Tjeng, Y.U. Idzerda, P. Rudolf, F. Sette and C.T. Chen, J. Appl. Phys., 70 (1991) 5939.
[Tje92a] L.H. Tjeng, C.T. Chen and S.W. Cheong, Phys. Rev. B, 45 (1992) 8205.
[Tob92] J.G. Tobin, G.D. Waddill and D.P. Pappas, Phys. Rev. Lett., 68 (1992) 3642.
[Tog86] R. Torge, F. Riemer, E. Heynacher and W. Opitz, Zeiss Inform., 29 (1986) 55.
[Tol92] H. Tolentino, M. Medarde, A. Fontaine, E. Dartyge, D. Guay and G. Tourillon, Phys. Rev. B, 45 (1992) 8091.
[Tol93] H. Tolentino, M. Medarde, A. Fontaine, F. Baudelet and E. Dartyge, J. Electron Spectrosc. Relat. Phenom., 62 (1993) 167.
[Tor92] J.B. Torrance, P. Lacorre, A.I. Nazzal, E.J. Ansaldo and Ch. Niedermayer, Phys. Rev. B, 45 (1992) 8209.
[Tro90] L. Tröger, D. Arvanitis, H. Rabus, L. Wenzel and K. Baberschke, Phys. Rev. B, 41 (1990) 7297.
[Uoz92] T. Uozumi, K. Okada, A. Kotani, O. Durmeyer, J.P. Kappler, E. Beaurepaire and J.C. Parlebas, Europhys. Lett., 18 (1992) 85.
[Van90] J.F. van Acker, P.J.W. Weijs, W. Speier, J.C. Fuggle and R. Zeller, in A. Balerna, E. Bernieri and S. Mobilio (Eds.), Proc. 2nd European Conference on Progress in X-ray Synchrotron Radiation Research, Rome, November 1989, SIF, Bologna, 1990, p. 55.
[Van90t] J.F. van Acker, Magnetism and Covalence: The Electronic Structure of Localized Perturbations, Ph.D. Thesis, University of Nijmegen, 1990.
[Vee93a] M. van Veenendaal and G.A. Sawatzky, Phys. Rev. Lett., 70 (1993) 2459.
[Vee93b] M. van Veenendaal, H. Eskes and G.A. Sawatzky, Phys. Rev. B, 47 (1993) 11463.
[Vel90t] J. van Elp, Ph.D. Thesis, University of Groningen, 1990.
[Vel91a] J. van Elp, J.L. Wieland, P. Kuiper, G.A. Sawatzky, F.M.F. de Groot and T.S. Turner, Phys. Rev. B, 44 (1991) 6090.
[Vel91b] J. van Elp, B.G. Searle, G.A. Sawatzky and M. Sacchi, Solid State Commun., 80 (1991) 67.
[Vel92] J. van Elp, H. Eskes, P. Kuiper and G.A. Sawatzky, Phys. Rev. B, 45 (1992) 1612.
[Ver86] M. Verdaguer, C. Cartier, M. Momenteau, E. Dartyge, A. Fontaine, G. Tourillon and A. Michalowicz, J. Phys. (Paris) C, 8 (1986) 649.
[Vic85] R.H. Victora and L.M. Falicov, Phys. Rev. Lett., 55 (1985) 1140.
[Vog93] J. Vogel, M. Sacchi, F. Sirotti and G. Rossi, Appl. Surf. Sci., 65/66 (1993) 170.
[Von79] U. von Barth and G. Grossmann, Solid State Commun., 32 (1979) 645.
[Von82] U. von Barth and G. Grossmann, Phys. Rev. B, 25 (1982) 5150.
[Vvd92] D.D. Vvedensky, in J.C. Fuggle and J.E. Inglesfield (Eds.), Unoccupied Electronic States, Springer, Berlin, 1992, p. 139.
[Wad86] W.G. Waddington, P. Rez, J.P. Grant and C.J. Humphreys, Phys. Rev. B, 34 (1986) 1467.
[Wan77] C.S. Wang and J. Callaway, Phys. Rev. B, 15 (1977) 298.
[Way83] G.A. Waychunas, M.J. Apted and G.E. Brown, Jr., Phys. Chem. Miner., 10 (1983) 1.
[Way87] G.A. Waychunas, Am. Mineral., 72 (1987) 89.
[Way90] G.A. Waychunas and G.E. Brown, Jr., Phys. Chem. Miner., 17 (1990) 420.
[Wei90] R. Weidemann, B. Burmester, H.E. Gumlich, C. Jung, T. Kleemann, T. Kreitler, A. Krost, H.U. Middlemann, U. Becker, M. Kupsch and S. Bernstorff, J. Cryst. Growth, 101 (1990) 916.
[Wey91] P.J.W. Weijs, M.T. Czyżyk, J.F. van Acker, W. Speier, J.B. Goedkoop, H. van Leuken, H.J.M. Hendrix, R.A. de Groot, G. van der Laan, K.H.J. Buschow, G. Wiech and J.C. Fuggle, Phys. Rev. B, 41 (1990) 11899.
[Wie91] R. Wienke, G. Schütz and H. Ebert, J. Appl. Phys., 69 (1991) 6147.
[Wil79] A.R. Williams, J. Kübler and C.D. Gelatt, Jr., Phys. Rev. B, 19 (1979) 6094.
[Wim92] M. Willmann, H. Petersen, F. Schäfers, M. Mast, B.R. Müller and W. Gudat, BESSY Jahresbericht, 1991.
[Wis72] J.A. Wilson, Adv. Phys., 19 (1972) 1.
[Wis88] J.A. Wilson, in J.C. Fuggle, G.A. Sawatzky and J.W. Allen (Eds.), Narrow Band Phenomena, Plenum Press, New York, 1988, p. 209.
[Won84] J. Wong, F.W. Lytle, R.P. Messmer and D.H. Maylotte, Phys. Rev. B, 30 (1984) 5596.

[Won89] J. Wong and G.A. Slack, Physica B, 158 (1989) 627.
[Won90] J. Wong, G. Shimkaveg, W. Goldstein, M. Eckart, T. Tanaka, Z. Rek and H. Tompkins, Nucl. Instrum. Methods A, 291 (1990) 243.
[Woo87] R.G. Woolley, Int. Rev. Phys. Chem., 6 (1987) 93.
[Wuy92] Y. Wu, J. Stöhr, B.D. Hermsmeier, M.G. Samant and D. Weller, Phys. Rev. Lett., 69 (1992) 2307.
[Wyb65] B.G. Wybourne, Phys. Rev., 137 (1965) 364; Spectroscopic Properties of Rare Earths, Interscience, New York, 1965, Chapt. 2, 17.
[XAS91] S.S. Hasnain (Ed.), X-ray Absorption Fine Structure, Vol. VI, Ellis Horwood, Chichester, 1991, Chapt. IV, pp. 191–282 and references cited therein.
[Yam77] T. Yamaguchi and S. Sugano, J. Phys. Soc. Jpn., 42 (1977) 1949.
[Yam82a] T. Yamaguchi, S. Shibuya and S. Sugano, J. Phys. C, 15 (1982) 2625.
[Yam82b] T. Yamaguchi, S. Shibuya, S. Suga and S. Shin, J. Phys. C, 15 (1982) 2641.
[Yas83] J. Yamashita and S. Asano, J. Phys. Soc. Jpn., 52 (1983) 3506.
[Yaz93] H. Yamazaki, H. Miroshi, K. Kobayashi and K. Shimomi, Jpn. J. Appl. Phys., 32 (1993) 317.
[Zaa85a] J. Zaanen, G.A. Sawatzky and J.W. Allen, Phys. Rev. Lett., 55 (1985) 418.
[Zaa85b] J. Zaanen, G.A. Sawatzky, J. Fink, W. Speier and J.C. Fuggle, Phys. Rev. B, 32 (1985) 4905.
[Zaa86a] J. Zaanen, C. Westra and G.A. Sawatzky, Phys. Rev. B, 33 (1986) 8060.
[Zaa86t] J. Zaanen, The Electronic Structure of Transition Metal Compounds in the Impurity Model, Ph.D. Thesis, University of Groningen, 1986.
[Zaa88] J. Zaanen, O. Jepsen, O. Gunnarsson, A.T. Paxton, O.K. Andersen and A. Svane, Physica C, 153–155 (1988) 1636.
[Zaa90] J. Zaanen and G.A. Sawatzky, J. Solid State Chem., 88 (1990) 8.
[Zel92] R. Zeller, in J.C. Fuggle and J.E. Inglesfield (Eds.), Unoccupied Electronic States, Springer-Verlag, Berlin, 1992, p. 25.

Appendix A: Final state effects on Hubbard model parameters

An important question for the description of core level spectroscopies using short range model Hamiltonians is possible final state effects on the model parameters used. In many papers this question is not touched upon and it is tacitly assumed that one can use identical parameters in the final state as used in the initial state. The final state is described by adding the effect on the core hole potential (U_{cd}) acting on the localized states. It is however not obvious that the Coulomb repulsion U_{dd}, the (symmetry dependent) hopping terms t_{pd} and the cubic crystal field splitting (10Dq) are equal in the final state.

In most papers using the Anderson impurity model, or related short range models, it is assumed that the hopping should increase in the final state of 2p XPS due to the presence of the core hole, which gives an extra term in the matrix element [Zaa86t, Zaa90]. Gunnarsson et al. [Gun88a, Gun89a] analysed the final state hopping in detail. They pointed out two counteracting effects: (1) the extra term in the matrix element, and (2) the fact that the localized wavefunctions (ϕ_d) tend to localize further because of the core hole. For the case of Mn of CdTe the finding is that if a core hole is included, the hopping is reduced by about 20%. In other words the localization effect is found to be more important than the extra hopping term.

Apart from differences between initial state and final state there can also be differences between different experiments, such as 2p XPS, 2p XAS and 1s XAS, particularly because the screening processes will be different. For example in [Laa92a] U_{cd} is chosen to be different in 2p XPS and 2p XAS. Moreover if the hopping in the final state is different from the ground state this will affect the spectral shape. Another consequence is that if a (single) value for the hopping is determined empirically from core level spectroscopy, this value will correspond to the final state value (or to some kind of effective mean value of ground state and final state).

Also the Coulomb repulsion U_{dd} is not necessarily identical in the final state. In atomic multiplet calculations the two electron integrals $\langle 3d, 3d|1/r|3d, 3d\rangle$ are calculated ab initio. It turns out in the final state of 2p XAS that these integrals are increased by about 5 to 10% (see for example the table for the Slater integrals in Ref. [Deg90a]), hence the atomic (unscreened) value of U_{dd} will also be 5 to 10% larger. For this reason also the final state value of U_{dd} can be

expected to be slightly larger than the value in the ground state.

A detailed study has been performed for the creation of an oxygen 1s core hole in the copper oxides [Hyb92]. Apart from the large effect of the core hole potential on the oxygen 2p states (U_{cp}), also the effect on the neighbouring 3d states (U^{κ}_{cd}) was considered. (κ denotes inter-electronic Coulomb repulsions.) It was shown that there is an effect on the Coulomb repulsion of the neighbouring sites. U_{dd} decreases from 4.1 to 3.7 eV. This finding can be generalized to the following statement:

A core hole created on site increases U_{dd}, but created at a neighbouring site it decreases U_{dd}.

Another finding of this study is that the hopping t_{pd} is significantly decreased from 0.43 eV to 0.20 eV, which is (qualitatively) a similar result to the Mn in CdTe system discussed above.

Another problem is that for the simulation of metal 1s X-ray absorption the parameters which give the best description of the spectral shape are modified in the final state, which is motivated from the final state effects of the excited electron in an np state. Within the model description with only metal 3d and ligand 2p the effective parameters in the final state are likely to be re-adjusted [Tol92].

Thus it can be concluded that the model parameters in the final states of different experiments are in general only roughly known and systematic final state effects, apart from the inclusion of U_{cd}, are in general not used. In my opinion this is an important problem because the eventual final state effects on model parameters are important for the accurate determination of the ground state values, that is for our understanding of the ground state electronic structure. In other words

> An accurate description of the ground state is only possible with correct inclusion of final state effects.

Appendix B: Abbreviations, etc.

The often used abbreviations and symbols are given. In many sections symbols are used (and defined) within the context given. They are not repeated here.

Group theory symmetry notations (A_1, E, etc.) can be found in [Sug70]. Some alternative notations are in use (0, 1, etc.) or (Γ_1, etc.); see Butler [But81] for details.

Angular momentum notations (L, S, J, M_J, ...) and term symbols ($^4T_1$) can be found in, for example, [Sug70, Grf64].

Electronic structure models

ASW	Augmented spherical wave method
CEPA	Coupled electron pair approximation
CT-M	Charge transfer-multiplet model
DOS	Density of states
DFT	Density functional theory
FOCI	First order configuration-interaction
GGA	Generalized gradient approximation
GW	*G* (Green function) *W* (screened Coulomb interaction) method
HF	Hartree–Fock approximation
KKR	Koster Koringa Rostoker
LAPW	Linearized augmented plane wave
LFM	Ligand field multiplet
LMTO	Linearized muffin-tin orbital
LSD	Local spin density approximation
MC	Multi-configurational
MS	Multiple scattering
OP	Orbital polarization
SCF	Self-consistent field
SIC	Self-interaction correction

Experimental techniques

BIS	Bremsstrahlung Isochromat Spectroscopie = (inverse (X-ray) photoemission)
EELS	Electron energy loss spectroscopy
EPR	Electron paramagnetic resonance
EXAFS	Extended X-ray absorption fine structure
IPS	Inverse photoemission spectroscopy
K edge	X-ray excitation of 1s state
L_1 edge	X-ray excitation of 2s state

$L_{2,3}$ edge	X-ray excitation of 2p state (split by core state spin–orbit coupling)
TEY	Total electron yield
XANES	X-ray absorption near edge structure
XAS	X-ray absorption spectroscopy
XPS	X-ray photoelectron spectroscopy

Symbols

B	Racah parameter ("orbit") (see Table 2)
C	Racah parameter ("spin") (see Table 2)
C	Kanamori parameter ("orbit") (see Table 2)
10Dq*	Cubic ligand field splitting (the asterisk denotes an average value)
$(\mathscr{D})$	Cubic ligand field splitting
F^2	Slater integral
G^1	Slater (exchange) integral
I_s^*	(mean) Stoner exchange coupling
J	Exchange splitting (see Table 2) (Kanamori parameter ("spin"))
$\langle L_z \rangle$	Orbital moment
n	Density of states
n^+	...spin-up
n^-	...spin-down
P_e	Fano constant
Φ and ϕ	Wavefunction (subscript denotes orbital quantum number, superscript denotes core (c) or valence (v))
q	polarization of the X-ray (−1, 0, +1)
σ	X-ray absorption cross section
σ^+	...right circularly polarized
σ^-	...left circularly polarized
σ^0	...z polarized
$\langle S_z \rangle$	Spin moment
ζ	Spin–orbit coupling

Anderson impurity model

$a^\dagger$	Creation operator (second quantization)
Δ	Charge transfer energy ($\varepsilon_d - \varepsilon_{pk}$)
ε_d	Energy position of d state
ε_{pk}	Energy position of p band
n	Occupation number ($a^\dagger a$)
t_{pd}	Hopping terms
U	Coulomb interaction energy
V_{eff}	Effective interaction strength